2023

Aptamer-based sequence verification platform for rapid multiplexed detection of viral RNA targets

BOSTON UNIVERSITY

COLLEGE OF ENGINEERING

Thesis

APTAMER-BASED SEQUENCE VERIFICATION PLATFORM FOR RAPID MULTIPLEXED DETECTION OF VIRAL RNA TARGETS

by

AMIT ESHED

B.S.E., University of Connecticut, 2021

Submitted in partial fulfillment of the

requirements for the degree of

Master of Science

2023

Approved by

First Reader

Alexander A. Green, Ph.D.
Assistant Professor of Biomedical Engineering

Second Reader

Ahmad S. Khalil, Ph.D.
Professor of Biomedical Engineering

Third Reader

John T. Ngo, Ph.D.
Assistant Professor of Biomedical Engineering

DEDICATION

To my family, my very first teachers who continue to inspire and motivate me, who engage my curiosity about all the wonders on the earth and taught me my very first lesson: *learning how to learn*.

ACKNOWLEDGEMENTS

I would like to thank Dr. Alexander Green and Dr. Zhaoqing Yan for your mentorship, training, and support, I have learned so much in such a short period of time. I would also like to thank all of the members of the Green lab, for welcoming me in, talking through and fleshing out all of the ideas and experiments that I had, and for answering all of my questions. Additionally, for the preparation of this manuscript I want to thank everyone who was able to review it and provide excellent feedback. Thank you all.

APTAMER-BASED SEQUENCE VERIFICATION PLATFORM FOR RAPID MULTIPLEXED DETECTION OF VIRAL RNA TARGETS

AMIT ESHED

ABSTRACT

Diagnostic detection of viruses is a cornerstone method for the management of emerging epidemics and pandemics. However, current limitations in commercially available and gold standard diagnostic detection platforms like cost, time to signal readout, and sensitivity, expose gaps in viral surveillance. To address these limitations, we have developed a novel Point-of-Care aligned method for the rapid isothermal amplification of viral RNA targets using RT-LAMP, and amplicon sequence verification using an aptamer-based colorimetric signal readout. With this method established, we then developed multiplexing detection platforms that target globally impactful mosquito-borne viral diseases and pathogens, including Dengue virus and Malaria, as well as the viruses that they are often misdiagnosed with, like Zika and Chikungunya viruses. With these platforms, we demonstrate both a quantitative and qualitative distinguishment of up to four mosquito borne pathogenic RNA targets at once in a single multiplexed detection platform.

TABLE OF CONTENTS

LIST OF TABLES

LIST OF FIGURES

LIST OF ABBREVIATIONS

Broc	Broccoli
CHIKV	Chikungunya Virus
DENV	Dengue Virus
DFHBI-1T	(Z)-4-(3,5-difluoro-4-hydroxybenzylidene)-2-methyl-1-(2,2,2-trifluoroethyl)-1H-imidazol-5(4 H)-one
DFHO	4-(3,5-difluoro-4-hydroxybenzylidene)-1-methyl-5-oxo-4,5-dihydro-1*H*-imidazole-2-carbaldehyde oxime
DNA	Deoxyribonucleic Acid
dsDNA	Double-stranded Deoxyribonucleic Acid
FQ	Fluorophore Quencher
LAMP	Loop-Mediated Isothermal Amplification
LFA	Lateral Flow Assay
LoD	Limit of Detection
MFE	Minimum Free Energy
NASBA	Nucleic Acid Sequence Based Amplification
NTC	No-Target Control
NUPACK	Nucleic Acid Package
OBI	3,5-difluoro-4-hydroxybenzylidene-imidazolinone-2-oxime-1-benzoimidazole
OBroc	Orange Broccoli
PCR	Polymerase Chain Reaction
PlsF	*Plasmodium falciparum*
POC	Point-of-Care
RBroc	Red Broccoli
RDT	Rapid Diagnostic Test
RFU	Relative Fluorescent Units
RNA	Ribonucleic Acid
RPA	Recombinase Polymerase Amplification
rRNA	Ribosomal Ribonucleic Acid
RT	Reverse Transcription
RT-LAMP	Reverse Transcription Loop-Mediated Isothermal Amplification
RT-PCR	Reverse Transcription Polymerase Chain Reaction
RT-RPA	Reverse Transcription Recombinase Polymerase Amplification

SARS-CoV-2	Severe Acute Respiratory Syndrome Coronavirus 2
SELEX	Systematic Evolution of Ligands by Exponential Enrichment
ssDNA	Single-stranded Deoxyribonucleic Acid
TMSD	Toehold-Mediated Strand Displacement
TO	Thiazole Orange
TO1	Thiazole Orange 1
TO3	Thiazole Orange 3
WNV	West Nile Virus
YFV	Yellow Fever Virus
YO3	Oxazole Yellow 3
ZIKV	Zika Virus

Chapter 1

INTRODUCTION TO VIRAL DETECTION AND APTAMER-BASED DIAGNOSTICS

In this chapter, we will introduce the impact and current state of diagnostic testing for disease management (Section 1.1). Taking lessons learned from current and past pandemics and epidemics will help outline the guiding principles for the design of our proposed viral diagnostic detection platforms (Section 1.2). For each step and process in designing our platforms, we identify the available options and considered what materials (Section 1.3) and methods (Sections 1.4-1.6) used will best align our platforms for Point-of-Care (POC) needs.

For this research, we will develop nucleic acid-based POC-aligned diagnostics for the detection of high impact viral RNAs and pathogens. We will demonstrate platforms for the detection of: Severe Acute Respiratory Syndrome Coronavirus 2 (SARS-CoV-2), Chikungunya virus (CHIKV), Dengue virus (DENV), West Nile virus (WNV), Yellow Fever virus (YFV), Zika virus (ZIKV), and *Plasmodium falciparum* (PlsF) the parasite that causes Malaria.

1.1 The Impact of Diagnostic Detection Tests

The SARS-CoV-2 pandemic and other recent epidemics have highlighted the magnitude and the variety of roles diagnostic testing serves for the management, tracking, and identification of diseases. As of March 21st, 2023, there have been over 761 million reported cases and 6.8 million deaths from SARS-CoV-2[1]. Since SARS-CoV-2 is highly

transmissible and can present as asymptomatic, diagnostic population screenings have been used to monitor and control viral transmission on a large scale, while also identifying patients who would otherwise be unaware of carrying the virus[2],[3].

The rapidity of time-to-signal readout of diagnostic tests is particularly important for viral management as seen by the 2005-6 CHIKV outbreaks across the Indian Ocean[4],[5]. In 2005, CHIKV hopped from the Comoros Islands to Mayotte, Mauritius, Madagascar, the Seychelles, and Réunion Islands. While the remoteness of a viral outbreak on an island would typically help with containment, the insufficient testing allowed the spread of CHIKV to outpace detection and quarantine, culminating in the 2006 Réunion Island epidemic during which at least 30% of the population (244,000 of 770,000 people) was infected[4],[5]. Genotyping the samples collected from the island outbreaks and mapping the microevolution patterns allowed for the tracking of CHIKV to an original strain in East Africa, despite the fact there were no reports of CHIKV there[4].

While the speed of signal readout for diagnostic tests can be vital for disease management, the specificity (ability to correctly test negative cases) of diagnostic tests is crucial in the identification of viral outbreaks. In 2007, physicians from Yap of the Federated States of Micronesia declared a local Dengue epidemic when rapid assay laboratory testing diagnosed patient samples with DENV. Two months later when the samples were sent to the Centers for Disease Control diagnostic laboratory, it was discovered that the rapid tests misdiagnosed DENV, and in fact Yap had a ZIKV outbreak[6]. The implications of misdiagnosing an epidemic can be critical, impacting the methods and resources health

services have for managing and treating diseases, as well as the speed and control they have to react.

Identification of an outbreak can be made additionally difficult due to the co-circulation or unaware silent circulation of viruses[7]. As of 2021, DENV is endemic in 128 countries with an estimated 400 million annual infections[8-13]. This wide-spread presence puts incredible demand for diagnostic testing by national surveillance programs, which can have unintended consequences. In 2013, a Dengue outbreak was declared in India, and while certain regions of India are DENV endemic, a study from Saswat et al., observed that of patients suspected of having DENV, 32.43% actually had CHIKV, and 44.8% were co-infected with both viruses[14]. The lack of initial reporting of a CHIKV outbreak may have had several different causes. For one, India being declared Dengue endemic may have caused a reporting bias for DENV and unintentional misdiagnosing due to CHIKV presenting similar symptoms to DENV while being less pervasive[14],[15]. Other challenges included a lack of a dedicated CHIKV surveillance program, and unreported patients who were symptomatic but did not go to clinics or hospitals to seek treatment[15]. From 2015 to 2017, Brazil experienced a triple circulation of CHIKV, DENV, and ZIKV viruses[7],[16],[17]. Diagnosing patients was made difficult due to an overburdened system and antibody tests' insufficient sensitivity (ability to correctly test positive cases)[7],[18],[19]. The cross-reactivity of the patient antibodies in serological assays resulted in false-positive tests and misdiagnosed patients[16].

Centralized laboratories can be put under significant pressure with the onset of a new disease and the co-circulation of viruses. From 2000 to 2019, global Malaria cases had

been steadily decreasing, however when the onset of the SARS-CoV-2 pandemic caused a redirection of resources away from Malaria testing, the number of Malaria cases increased in 2020 and deaths from Malaria increased globally for the first time in 20 years[20]. In considering the design and development of the next generation of diagnostic tests it is critical that such tests operate rapidly, are highly specific, and can offer multiplexed detection without increasing the workload of centralized laboratories.

1.2 Point-of-Care Tests

In this section, we will discuss the gap between current diagnostic tests and POC tests.

1.2.1 What are Point-of-Care tests?

POC tests are diagnostic tests that are designed to be inexpensive, fast, and accessible to non-technical users[21]. This is of crucial importance during disease outbreaks because detection and mitigation efforts must be scaled up rapidly, with minimal training or reliance on a limited number of specialists. There are several factors in the operation of diagnostics that influence whether a test is POC aligned. Material resources, like the use of sensitive reagents, complex equipment, and laboratory space, greatly impact the end cost, speed, and accessibility. Complex tests require the employment of skilled operators and advanced equipment to conduct high-throughput batch testing, which makes such operations less POC aligned.

One of the most successful examples of POC diagnostics are at-home pregnancy tests[22]. Such tests make use of lateral flow assay (LFA) technology. They are low cost, quick and convenient to test at home, and easy for users to interpret with a simple colorimetric or

digital readout[21],[22].

1.2.2 Why should diagnostic tests be Point-of-Care?

POC tests offer the convenience of location. Consider, for example, the transmission of DENV, which is typically concentrated in urban areas[10],[17]. The expansion of the habitable zones for its mosquito vectors into more rural and low-resource environments due to climate changes exposes gaps in viral surveillance that are out of range of central laboratories for timely sample processing[7],[23]. POC tests do not require samples to travel to laboratories, cutting down on processing time and costs by avoiding transportation, processing, and distributing test results, all of which increase the likelihood of operational errors like mislabeling, samples expiring, or cross-patient contamination[22]. Rapid POC tests, which deliver results directly to the user, are useful as early warning surveillance[19]. They can also be critical for early diagnosis, which may greatly impact survival outcomes for patients[8],[10],[17],[20]. Diseases like DENV and Malaria are known for sudden escalations from mild to severe symptoms with fatal outcomes if not treated in a timely manner[10],[20].

Inexpensive POC diagnostics can serve as a key tool for disease management, benefiting both individual patients and national health surveillance programs[10]. By improving testing accessibility and reducing the personal burden caused by traveling to distant health facilities, POC tests can offer significant benefits and reach a greater number of individuals[22]. In cases where communities are amid a surging epidemic or pandemic, national laboratories can quickly become overburdened[13]. POC testing relieves the bottleneck of diagnostic testing from laboratories. One such example is the 2015-16 ZIKV epidemic that occurred in Brazil. Brazil's five national diagnostic laboratories experienced

a significant backlog of tests such that high-priority patients had up to a 3-week turnaround time on their test results[18],[19]. During this crisis, which included the circulation of CHIKV and DENV, many patients could not be diagnosed based on tests but rather symptomatic manifestations[7]. A study by Silva et al. found that of patients who had DENV only 9.4% were correctly diagnosed, while 18.7% were initially diagnosed with ZIKV. For patients who had CHIKV, only 10.7% were correctly diagnosed, with 30.8% diagnosed with DENV and 6.9% with ZIKV. This was directly attributed to the overburdened laboratories and use of symptom-based diagnoses. In cases where patients were co-infected with CHIKV and DENV, 23.1% were initially diagnosed with DENV only and none were identified with CHIKV[7].

1.2.3 Why do we need to advance Point-of-Care tests?

The current gold standard for diagnostic tests is reverse transcription polymerase chain reaction (RT-PCR), on account of its excellent test specificity and sensitivity[2],[3][24-26]. However, RT-PCR is unaligned to POC needs because it requires the use of complex equipment, conducted by skilled operators over several hours, making such tests expensive, slow, and inaccessible to many communities[2],[3],[24],[25],[27]. POC assays that rely on antibody detection like LFAs or rapid diagnostic tests (RDTs), while fast and relatively inexpensive, are limited by poor sensitivity as cross-reactive antibodies result in high false-positive rates[2],[8],[12],[16],[21],[26]. Such errors enable the misdiagnoses of viruses in co-circulating environments. The accurate POC reporting of viruses still remains a central challenge in disease management, which is linked to what materials are being detected in diagnostic tests[10].

1.3 Viral RNA as a Genomic Biomarker for Characterizing Pathogens

In the area of molecular diagnostics there are three types of detectable materials to consider: small-molecules[28-31], proteins[6],[7],[9],[10],[16],[20-22],[31-33], and nucleic acids[8],[10],[24],[27],[32-37] for which there are numerous diagnostic platforms already developed. In the context of creating platforms for the detection of viruses, small molecules, or metabolites, are not particularly relevant because viruses rely entirely on host mechanisms, and therefore do not have a signature metabolic process. The detection of host-response proteins like antibodies has been utilized before in POC tests but suffers from poor sensitivity and issues with cross-reactivity as mentioned in the previous sections. Viral antigens, like surface-presenting or non-structural proteins, can be used as a biomarker. However, to have a detectable quantity, the virus needs to be cultured in-lab from patient blood samples followed by a protein-purification[7],[8],[16].

Diagnostic antigen-based tests are not POC aligned since viral culturing and protein isolation is a complex procedure that can take on the order of days to weeks to process, which adds a significant cost and turnaround time in the face of rapidly evolving disease outbreaks[16]. Therefore, protein-based molecular diagnostics for viral detection may not be appropriate for POC platforms. Lastly, we can consider the detection of nucleic acid sequences from the viral genome.

Nucleic acid sequences as a detectable viral genomic material are well suited for POC diagnostics. Compared to antibody-based diagnostics, nucleic acids can be detected and have a peak concentration much earlier in the pathogenesis than antibodies, making them

more sensitive for earlier diagnoses[16]. Nucleic acids can be easily extracted from patient saliva samples with a short boiling step[19],[27]. Unlike serum or blood samples, commonly used for protein-based diagnostics, patient saliva is POC-aligned since it can be readily provided by a patient without physical or technical difficulties and discomforts[7],[10],[16]. Deoxyribonucleic acids (DNAs) and ribonucleic acids (RNAs) also follow a predictable thermodynamic behavior with well-known Watson-Crick base-pair binding interactions, meaning that a detection system based on these binding rules can follow a generalizable design[34],[35],[37],[38]. Additionally, transcription and reverse-transcription (RT) methods enable the conversion of target sequences between DNA and RNA which can be useful for creating a generalized system for detecting any virus or pathogen regardless of what form its genome is in.

For our platforms, we aim to develop nucleic acid-based diagnostic assays targeting the following: CHIKV[4], DENV[10],[16],[39], SARS-CoV-2[3], WNV[9], YFV[9], and ZIKV[39] all of which are RNA viruses, as well as the RNA of recombinant Pfs25 protein from PlsF. All viral RNA targets can benefit from cell-free nucleic acid amplification techniques. The ability to amplify target sequences in a cell-free method like PCR or RT-PCR means that detecting viral RNA from patient samples is not entirely dependent on the volume of sample collected. Sample volumes can be minimized on to the order of microliters provided that the sample meets a target concentration at or above the limit of detection (LoD) for the amplification method[2]. While PCR-based amplification is not POC aligned due to the sensitive reagents, complex equipment, and trained personnel required, there are a variety of isothermal amplification methods that can be utilized in a POC platform that allow for

rapid and single temperature amplification of DNA and RNA sequences.

1.4 Isothermal Amplification Methods

In this section we will explore isothermal amplification techniques to enable POC detection.

1.4.1 Motivation for Isothermal Amplification

The concentration of viral RNA varies during the pathogenesis. Viruses typically start with an accelerated incubation phase, causing a respective increase in viral RNA that peaks in concentration within days of exposure. Viral RNA then has a steady decline in concentration over the next several days to weeks[3]. Depending on the time-point a patient gets tested for viral RNA, the amount of RNA that can be detected is variable, which causes variations in the output signal strength. It is therefore necessary to amplify viral RNA targets not only to improve detection, but to reduce time-dependent variability in our POC platforms. Provided that the initial concentration of viral RNA meets the LoD of the amplification method, any patient sample regardless of the sampling timepoint will ideally produce an output signal of near-equal strength as illustrated in **Figure 1.1-A**. A viral concentration that is below the amplification LoD will not be amplified and can be construed as a false-negative result[2]. LoD sensitivity is therefore extremely important to amplify the largest dynamic range of RNA concentrations and provide detection as early as possible in the pathogenesis.

For laboratory and clinical-based tests, determining the concentration of viral RNA may be important. However, for POC user accessibility, it is not particularly helpful to quantify

the extent someone has a viral infection. At-home users simply want to know whether they are sick. In our POC platforms, an ideal signal output would produce an unambiguous signal of either positive or negative for viral RNA.

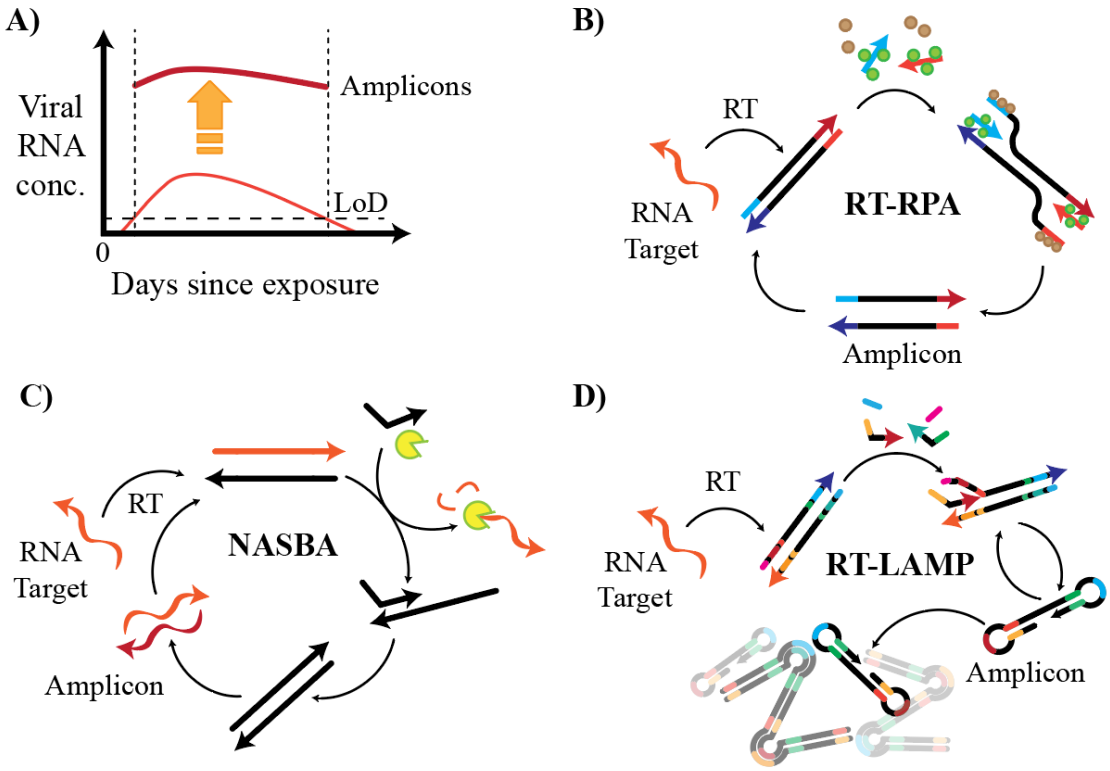

Figure 1.1 | Motivation and methodology of isothermal amplification methods. A) Amplification of viral targets at or above the method's LoD target concentration reduces time-dependent variability in amplicon concentration. **B)** Simplified representation of RT-RPA methodology. **C)** Simplified representation of NASBA methodology. **D)** Simplified representation of RT-LAMP methodology.

1.4.2 Recombinase Polymerase Amplification

In the Recombinase Polymerase Amplification (RPA) method, two oligonucleotide primers invade a homologous region of a double stranded DNA (dsDNA), stabilized by recombinase proteins. When the two strands of DNA separate, the single-stranded DNAs (ssDNA) stabilized by single strand binding proteins, are used as templates to synthesize

the target region producing an amplicon. For the purposes of amplifying an RNA target, a reverse transcriptase step can be incorporated to create a one-pot reverse transcription RPA (RT-RPA) method (**Fig 1.1-B**)[40].

RT-RPA can be performed between 37-42 ºC in a 20 minute or less amplification[40]. Additionally, platforms have been developed to amplify RNA targets at very low concentrations. For example, Lin et al., developed an RPA coupled with CRISPR detection system, achieving LoD 0.4 copies/µL of SARS-CoV-2 RNA targets[24]. While the RT-RPA method is very fast and has a simple one-step method, in our experimental investigation it has low specificity with a lot of non-target byproducts produced by recombinase-initiated non-specific binding and amplification.

1.4.3 Nucleic Acid Sequence Based Amplification

The Nucleic Acid Sequence Based Amplification (NASBA) method targets RNA (**Fig 1.1-C**). In cycles of reverse transcription and transcription, the NASBA method produces complementary DNA intermediates which serve as templates for RNA amplicons, after which the RNA gets degraded by RNaseH enzymes[10],[25],[41]. NASBA has been used for viral RNA amplification of CHIKV[18], DENV[10], ZIKV[27], and SARS-CoV-2[25] with exceptional sensitivity demonstrated. The optimal NASBA method is not technically isothermal because of an initial 65 ºC RNA primer binding step. After initial primer binding, NASBA produces amplicons at 41 ºC, with additional steps changing the operating temperature to activate and heat inactivate enzymes[27],[41]. This process can be simplified into a more POC-aligned one-step, one-temperature (41 ºC) protocol.

Despite a simplified protocol there are drawbacks to NASBA that may limit its efficacy as an amplification method for POC testing. NASBA is relatively slow, with a one-to-two-hour amplification period, and its reagents are relatively expensive compared to other methods[19],[27]. Additionally, NASBA is prone to cross-contamination, amplifying undesired targets and producing false positives and noisy signals resulting in a poor specificity[27].

1.4.4 Loop-Mediated Isothermal Amplification

The Loop-Mediated Isothermal Amplification (LAMP) method is based on a series of primers that continuously strand displace dsDNA products. The bound primers, which have complementary overhangs to other parts of the target region, are used to initiate the synthesis of the amplicons which self-bind to form a characteristic dumbbell-like structure[2]. Unlike RPA or NASBA, LAMP amplicons can form concatemers, meaning that there is not one single amplicon size produced. Like RT-RPA, a reverse transcriptase step can be incorporated into the LAMP method, enabling the amplification of RNA targets in reverse transcription LAMP (RT-LAMP) (**Fig 1.1-D**). RT-LAMP is fast, with a 30-minute incubation at a temperature range from 61~72 ºC[2]. From our experimentation, we have found 67 ºC to be an optimal temperature for amplicon production with the greatest amplicon yield. RT-LAMP is a relatively simple one-step method that is environmentally insensitive, capable of operating at a wider range of temperatures and pHs than RT-RPA or NASBA while still maintaining a high target sensitivity. Like NASBA however, RT-LAMP is prone to carryover contamination with false positive amplifications which can result in low specificity[2].

Low specificity is a drawback for all isothermal amplification methods mentioned. However, in diagnostics a high sensitivity is much more important and should be prioritized for the amplification method over high specificity. Poor specificity in amplification can be resolved when coupled with a highly specific post-amplification detection method, effectively filtering out noisy signals. All methods have their benefits and drawbacks in terms of POC alignment (see **Table 1** for summary).

Table 1 | Comparison of Isothermal Amplification Methods

Methods	Temperature	Time	POC		Ref.
			Benefits	Drawbacks	
RT-RPA	37-42°C	<20 min.	-Fast	-Poor specificity -Low yield	[24],[40]
NASBA	65°C, 41°C	1-2 hours	-Excellent sensitivity	-Slow -Expensive reagents -Poor specificity	[10],[18], [19],[25], [27],[41]
RT-LAMP	61-72°C	<30 min.	-Fast -Wide operational ranges (temp./pH)	-Poor specificity	[2]

For our platforms, we will use RT-LAMP as an isothermal amplification method for viral RNA targets. RT-LAMP is preferable over RT-RPA, based on our experience with RT-RPA showing limited amplicon yield, which is a significant issue with diagnostics. The amplification method of our targets must have high sensitivity and produce a significant yield of amplicons, because if we cannot amplify the targets sufficiently, then we cannot

detect them in post-amplification. RT-LAMP is also more POC aligned than NASBA due to RT-LAMP being a significantly faster and simpler method. RT-RPA and NASBA operate at lower temperatures than RT-LAMP which means that RT-LAMP requires a greater energy source for a POC test. However, the elevated temperature required by RT-LAMP can be used to our advantage for POC platforms. Because we wish to base our platforms on saliva samples, the viral RNA extraction step can be rolled into the amplification method. Boiling saliva at RT-LAMP operation temperatures means that unlike RT-RPA or NASBA, the entire process from extracting patient sample viral RNA to producing amplicons can be isothermal.

1.5 RNA Aptamers

Amplification of a target is not our final output detection method, but rather the means to produce enough target to use a POC-aligned visual indicator. RNA aptamers paired with fluorescent ligands will be used as a post-amplification detection system to produce a colorimetric signal akin to pregnancy tests.

RNA aptamers are short RNA sequences, typically between 25-90 nucleotides long, that bind with high affinity to a specific ligand[42]. Of them, fluorescent light-up aptamers are RNA sequences that can bind nontoxic, cell-permeable ligand fluorophores and activate their fluorescence over many orders of magnitude upon binding. Typically, they have two distinct regions, a stabilizing stem and a ligand interacting domain[30] as shown in **Figure 1.2-A**. The stabilizing stem is a sequence-independent region that, when bound in a hairpin motif via Watson-Crick base-pair interactions, enables the formation of a complex

secondary and tertiary-level structure in the ligand interacting domain[30],[42]. The successful binding of the stabilizing stem is necessary for prolonged stability of the ligand domain[43],[44].

The sequence-dependent ligand interacting domain makes use of Watson-Crick, Hoogsteen, and other non-canonical nucleic base interactions[45-49]. The purpose of these complex interactions is to establish a specific electrostatic environment that will enable the binding of a ligand to the nucleic acid sequence[35]. The stability of the ligand interacting domain is also aided by ions like K^+ and Mg^{2+} to resolve the innate electrostatic repulsions between nucleic acids[45-47],[50]. The binding of the ligand has been found to be mutually stabilizing for both the ligand and the aptamer[47],[50],[51]. Despite the fact that aptamers have extensive non-canonical nucleic acid interactions, they are very stable when activated with a low K_D, making them a viable alternative to antibodies in terms of binding affinity[22],[28],[34],[35]. Aptamers have been demonstrated to have a high binding affinity and specificity to a variety of targets including caffeine[52], cocaine[28], small ions like zinc[42], and large glycoproteins[42]. Aptamers also have a history of being used as fluorescent probes for *in vivo* imaging of RNA and target proteins, and have been found to be comparable to fluorescent proteins for intracellular labeling[48],[49],[53].

Aptamer structures are naturally occurring in the genome of prokaryotes and eukaryotes as riboswitches[46]. Riboswitches serve as natural intracellular sensors that mediate genetic circuit pathways by controlling transcription and translation processes[43],[46],[50]. The aptamers that we will use have been synthetically engineered to have high affinity to specific ligands. Synthetic aptamers have been developed and validated by a variety of

research groups using systematic evolution of ligands by exponential enrichment (SELEX) methods[31],[42],[47],[52-55]. The existing library of aptamers is extensive, with the ability to bind to a diverse range of targets[31],[44]. To create fluorescent probes, a set of aptamers will be used that bind to small-molecule ligands called fluorophores.

1.6 Aptamer-Fluorophore Interactions

For molecular imaging, there are a variety of popular fluorescent tools available, such as fluorescent proteins and fluorophore-quencher (FQ) probes. Fluorescent proteins are a common molecular biology biomarker used for *in vivo* imaging and for the development of synthetic genetic circuits[36],[37],[56]. In diagnostics, fluorescent proteins can be controlled by regulating the transcription and translation of the protein's gene[37],[57]. Fluorescent proteins have a long half-life. In the scenario that the system that regulates the production of proteins does not have excellent specificity, the platform will inevitably have a noisy background due to the accumulation of false positive signal from the fluorescent proteins[53],[57]. FQs triggered by a non-reversible cleavage causing the separation of the fluorophore probe from the quencher can also cause a poor signal-to-noise ratio for the same reasons[30],[35],[57],[58]. Unlike fluorescent proteins or FQs, aptamer-fluorophore interactions are reversible and therefore the noise can be near a low background level. Without false positive signals accumulating, noise generation in this system is a time-independent process. The generation of noise is an important factor to consider for POC diagnostics. Depending on the time the user checks their results, they may see a clear indicator in 30 minutes or an ambiguous signal after an hour.

Fluorophores exhibit fluorescence when excited by a specific excitation wavelength. The excitation raises the fluorophore's energy state and when the molecule drops back to ground level, it emits a lower energy signal. Fluorophores that are unbound can produce a signal but with a very weak intensity[59]. When a fluorophore is interacting with an aptamer, the electrostatic interactions cause a stabilization of the fluorophore molecule preventing dissipation of the small-molecule's energy from non-radiation processes like heat and molecular vibrations[56],[57]. When the stabilized fluorophore is energetically excited, it produces a higher intensity redshifted emission compared to its unbound state emission[59] (**Fig 1.2-B**).

Mango family aptamers are used extensively in this research. Mango aptamers are best characterized by their unique stacked G-quadraplex domains which forms guanine-boxes[45],[47],[57],[60]. A G-quadraplex is a non-canonical structural motif of four guanines interacting together via Hoogsteen binding to form a planar surface, with each guanine occupying a corner[45],[47],[57],[59],[60]. This surface produces a local negative charge within the aptamer[60]. The structure is stabilized typically with a monovalent cation like K^+ occupying the center of the guanine box[47],[57],[59],[60] (**Fig 1.2-C**).

The thiazole orange 1 (TO1) fluorophore specifically binds to a Mango-III aptamer with high affinity by intercalating between the surface of the upper G-quadraplex (red surface in Figure 1.2-C) and an A-U base pair[47],[59]. TO1 and TO1 derivatives that bind specifically to Mango aptamers, are stabilized by electrostatic interactions that sequester a hydrocarbon chain that links two ring groups of the fluorophore[42],[47],[56],[59],[60]. Both the fluorophore and the G-quadraplex are mutually stabilized when they interface[45],[60].

The main difference between the various Mango aptamers are the nucleotide sequences that link the set of guanines together[59]. Because Mango aptamers are structurally similar, they are capable of binding to each other's primary fluorophore, albeit with a lesser affinity and with different emission peaks. Mango-I and Mango-II aptamers have both been shown to bind to TO1 and thiazole orange 3 (TO3) fluorophores, each with different affinity and different fluorophore orientations on the aptamer[47]. For POC aligned tests we will want to demonstrate an ability to multiplex. Using Mango aptamers alone will not be suitable for multiplexing tests due to potentially poor orthogonality from aptamer-fluorophore cross reactivity. In addition to using Mango aptamers, we will also develop platform detection systems with Broccoli family aptamers. The differences in Broccoli and Mango aptamer structure and fluorophore binding mechanisms will allow for improved orthogonality in multiplexed platforms. Using different classes of aptamers will also increase the library of aptamers to work with and broaden the spectral range of signal outputs. **Figure 1.2-D** shows the peak bound state excitation and emission spectra for all the aptamer-fluorophore pairs we intend to use.

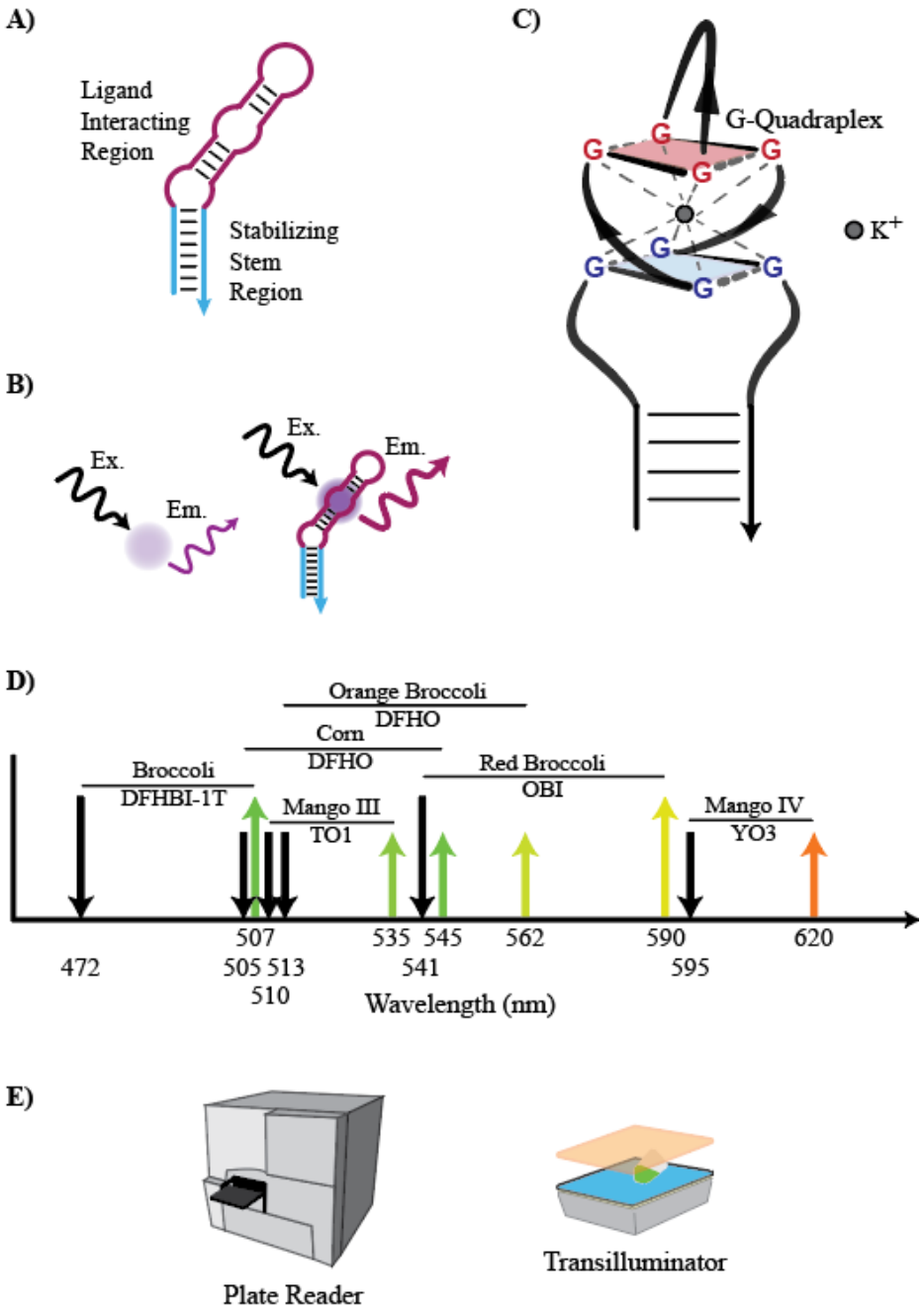

Figure 1.2 | Aptamer-fluorophore interactions. A) Aptamers are characterized by a sequence-independent stabilizing stem region and a sequence-dependent ligand interacting region. **B)** Fluorophores have higher intensity redshifted emission when interacting with an aptamer compared to unbound state. **C)** Characteristic double-layer G-quadraplex motif in Mango family aptamers stabilized by an internal K^+. **D)** Peak bound-state excitation (black arrows) and emission (colored arrows) spectra of aptamer-fluorophore pairs. **E)** Synergy Neo2 Multimode Microplate Reader is used for quantitative fluorescent measurements. A transilluminator is used for qualitative fluorescent measurements.

To observe fluorescence generated by aptamer-fluorophore binding, we will use a Synergy Neo2 Multimode Microplate Reader from BioTek. We will measure relative fluorescent units (RFU) in time-course curves for experiments that have one or two fluorescent channels, and single-point measurements for experiments with three or more channels. To qualitatively observe fluorescence, we will use a transilluminator with a blue source and an orange color filter (**Fig 1.2-E**). While each aptamer-fluorophore pair can be visually optimized under different source and filter wavelengths, all images will be taken under the same conditions for consistency.

Chapter 2

DEVELOPMENT OF AN APTAMER-BASED SEQUENCE VERIFICATION METHOD COUPLING ISOTHERMAL AMPLIFICATION FOR HIGHLY SENSITIVE TESTS

In this chapter, we will cover how we will use aptamers to react with amplicons to produce an output signal (Section 2.1). We will discuss how to generate new designs, model aptaswitches, and target binding *in-silico* (Section 2.2). Then, we will demonstrate the process of aptaswitch performance optimization experimentally (Section 2.3), and the development of a SARS-CoV-2 and a human positive control RNA detection platform coupled with RT-LAMP (Sections 2.4-2.6).

2.1 Aptamers to Aptamer-based Biological Switches (Aptaswitches)

To couple the sequence verification of the amplicons with sequence-specific fluorescence activation from the fluorophores, we will need to modify the aptamer structure. To achieve this coupling, we must make the correct folding of the aptamer contingent on its ability to recognize the sequence from the amplicon product[34],[35],[61]. To activate the aptamer in the presence of a trans-acting target, we will use a 5' toehold-mediated strand displacement (TMSD) mechanism[36],[58],[61],[62],[37]. Other activation methods such as loop-initiated[25] and kissing loop[34],[44] structures have been demonstrated to activate aptaswitches, however they are not as kinetically fast as TMSD activation[25],[38].

The design of our aptaswitch (**Fig 2.1-A**), starts by recognizing that the sequence-independent stabilizing stem region of the aptamer is necessary for the ligand-binding

domain to form[48]. By occluding one strand of the stabilizing stem in a hairpin structure we can effectively deactivate the aptamer by creating a thermodynamic barrier to aptamer folding. The addition of a 5' toehold domain to the occluding stem serves as the initial binding site for a target[62]. The target sequence, which is reverse complementary to the toehold domain and the adjacent half of the occluding stem, binds to the toehold region by Watson-Crick base pairing and then strand displaces the distal half of the stem[37],[38],[58],[61],[62]. With the prerequisite stabilizing stem domain now liberated from the occluding hairpin and in turn binding to the downstream 3' stabilizing stem, the functional aptamer structure is restored and can immediately interact with its fluorophore[48].

The core principle of the aptaswitch is the thermodynamic favorability of different states. The OFF state is more thermodynamically favorable than an untriggered-ON state, due to the stronger binding energy of the occluding hairpin, then an exposed single-stranded hairpin and a fully formed aptamer. Meanwhile, the OFF state is less thermodynamically favorable than the triggered-ON state where the aptaswitch complexes with a target, allowing for the base pairing of both the toehold and proximal half of the occluding stem as well as the formation of the aptamer. Such a thermodynamic background means that the aptaswitch device favors a tightly bound OFF state when there is no target present, thereby minimizing untriggered false-positive noise, but when a target is present the structure will rapidly change states and stably form an ON configuration[38] (**Fig 2.1-B**).

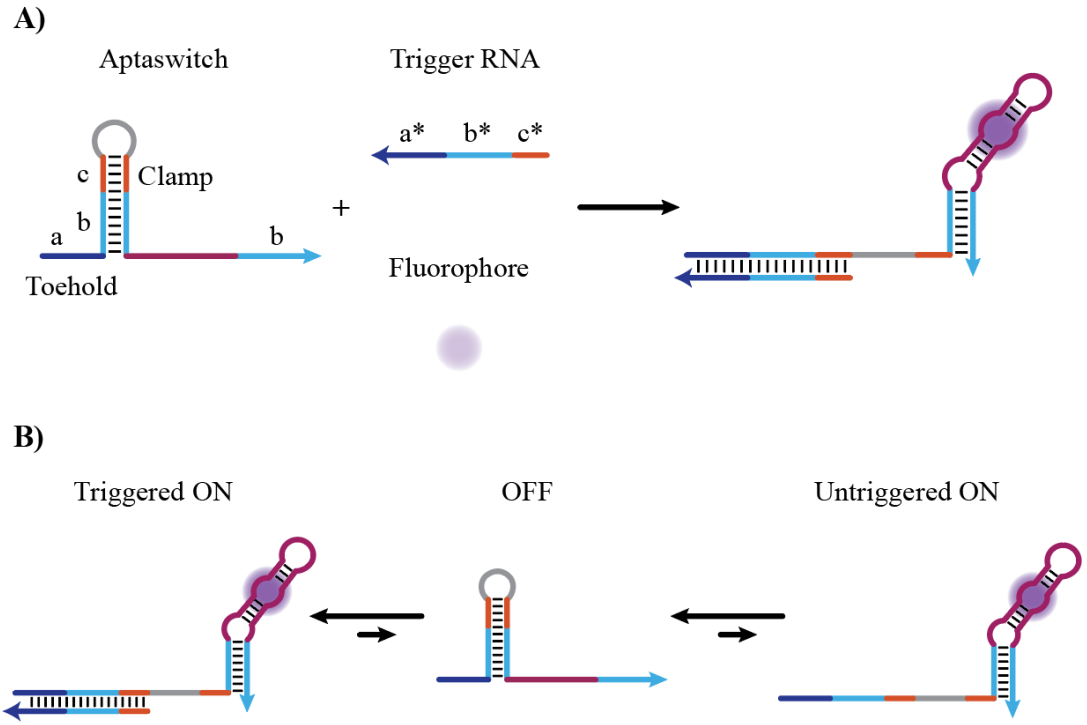

Figure 2.1 | Toehold-mediated strand displacement activation for aptaswitches. A) Mechanism of toehold-mediated strand displacement activating an aptamer in an aptaswitch structure. **B)** Thermodynamic preference of a triggered aptaswitch ON state over an OFF and untriggered ON state.

There are several design principles and structural motifs that allow us to design an aptaswitch with these thermodynamic preferences[63]. The presence of a clamp domain in the occluding stem between the captured stabilizing stem domain and the loop structure is necessary to make the occluding stem a stable interaction. The added nucleotides from the clamp create a longer occluding stem, which increases the energetic barrier[51],[63]. Having a clamp domain helps the aptaswitch favor an OFF state over an untriggered ON state[25],[64].

The toehold domain, if it is of sufficient length, is necessary to initially capture the target and hold it long enough while the rest of the target strand displaces the occluding stem.

Adding length to the toehold, up to a certain point, helps the aptaswitch with strand displacement. Additionally, the added base-paired nucleotides of the target binding with the toehold, the complementary stabilizing stem, and the clamp domains help with the thermodynamic favorability of a triggered-ON state over an OFF state.

Because the stabilizing stem is largely sequence-independent, the entire activation of an aptaswitch does not have any sequence limitations or requirements. This means that the aptaswitch has a generalizable design, allowing us to use virtually any nucleic acid target sequence to induce aptamer formation[37],[62].

2.2 In-Silico Design and Analysis of Aptaswitches

For the *in-silico* design and generation of our aptaswitches, the toehold, reverse complementary stabilizing stem from the aptamer, and clamp domains are all base-paired to the viral RNA target and therefore dependent on the target sequence. The ligand interacting domain of the aptamer is sequence-dependent and therefore constant in all aptaswitches that use the same aptamer base. To determine the unspecified sequences, like the loop domain, of the aptaswitch and evaluate the whole device and target binding *in-silico* we use Nucleic Acid Package (NUPACK) design and analysis software 4.0[65].

NUPACK design software generates sequence designs that best fit our coded secondary structure and prescribed design requirements. The software runs sequence permutations of unspecified domains to solve an optimization function for the minimum free energy (MFE) of the described structures. The structure energetics are calculated based on Watson-Crick base pairing and base stacking energies. A normalized ensemble defect is also calculated

to describe the fraction of nucleotides in the structure that are base-paired when they were not designed to be. A low normalized ensemble defect is an indicator that the NUPACK-generated sequence follows the secondary structure that we intended to design[65]. A low MFE, low normalized ensemble defect, and high base-pair binding probabilities as matched by our initial design are all indicators of a successfully designed aptaswitch sequence. See **Appendix A** for example NUPACK 4.0 aptaswitch design code and corresponding NUPACK MFE base-pairing probability diagrams of an aptaswitch, target, and aptaswitch-target complex (**Fig A.1**).

The choice of the target RNA from the viral genome, which determines most of the aptaswitch sequence, is narrowed down by certain requirements. For the monitoring of a specific virus or a variant, the target region must be genetically conserved[8]. If a diagnostic test is based on a region of the genome that constantly mutates, then the sensitivity and long-term utility of that test will be poor. Additionally, the target sequence should be in single-stranded form for compatibility with TMSD activation of the aptaswitch. A compatible target therefore should have little to no secondary structure[27],[36]. If the target region is part of a naturally occurring complex secondary and tertiary structure of the viral genome, then it may be inaccessible for RT-LAMP primers to bind and produce amplicons. If the target region is self-binding, then it may not hybridize to the toehold region of the aptaswitch, making TMSD activation ineffective[27]. Lastly, in the context of POC diagnostics, the desired target region should have little to no homology with any sequence in the human genome or the genome of other viruses of interest[27]. The no homology requirement is necessary to avoid false-positive and ambiguous signals. Viral genome

sequences, as well as the discovery of new mutations and variants are published by research groups and maintained in databases such as BLAST, GISAID, and GenBank.

Once a desirable aptaswitch has been generated by NUPACK, the aptaswitch and target sequences are ordered as DNA ultramers and oligos from Integrated DNA Technologies. For devices longer than 200 nucleotides, we order forward and reverse strand ultramers and forward and reverse primers and conduct a one-cycle PCR assembly. When the assembly of the aptaswitch is confirmed by gel electrophoresis, then all the target oligos and the assembled DNA aptaswitch templates undergo a 2.5-hour transcription. After transcription, the RNA products are column purified using the Monarch® Cleanup Kit by New England BioLabs. By calculating the extinction coefficient for the products and collecting the optical density A260 value from NanoDrop Microvolume Spectrophotometer by ThermoFisher Scientific, we then calculate the purified RNA concentration of the products as follows in equation 1.

$$Conc.[\mu M] = \frac{OD\ A260 \times 10^6}{Ext.\ Coeff.} \quad \text{[Eq. 1]}$$

All RNA products are then diluted in ultrapure water to a stock concentration and stored in -80 ºC until use.

2.3 Aptaswitch Detection and Platform Optimization

To verify the optimal aptamer-fluorophore pairs for Mango-I, -II, -III, and -IV with a series of thiazole orange (TO) derivatives, including TO1-Biotin, TO3-Biotin, and YO3-Biotin, we screened a set of aptaswitches of each Mango type against each fluorophore. When the

best-performing combinations of aptaswitch-fluorophore were found based on fold change, potential optimization steps were explored. Fold change is calculated as the ratio between a reaction with an aptaswitch, its respective target, and fluorophore to a no-target control (NTC).

For each Mango type, 10 aptaswitches and their respective arbitrary targets were generated via NUPACK. In total 40 unique aptaswitches were screened. Reactions were mixed at room temperature in a 96-well plate and read in the Plate Reader at 37 ºC. The aptaswitch was held as the limiting reagent with excess target and fluorophore. Ultrapure water was used to supplement the volume of the reaction up to 35 µL. The screening of Mango-IV aptaswitches against TO3 fluorophore was not performed.

Figure 2.2 shows the time-course curves of the identified top-performing aptaswitches per aptamer base per fluorophore. The ON green curve corresponds to when the fluorophore, aptaswitch, and its respective target are all present in the reaction. The red OFF curve indicates that only the fluorophore and aptaswitch are present, acting as the NTC. Any signal generated by an OFF curve constitutes leakage, or untriggered ON signal, in the aptaswitch device which should be thermodynamically unfavorable. The background black curve shows when only the fluorophore is present. The background should always produce the lowest fluorescence signal, as there is no aptaswitch present for a fluorophore to be able to bind to and produce an enhanced bound-state emission. Additionally, the background channel also acts as a Plate Reader instrumental control. There should be no time-dependent variations in the background signal. If the background signal increases or

significantly changes over a prolonged period, then that would indicate that the Plate Reader measurements are drifting over time.

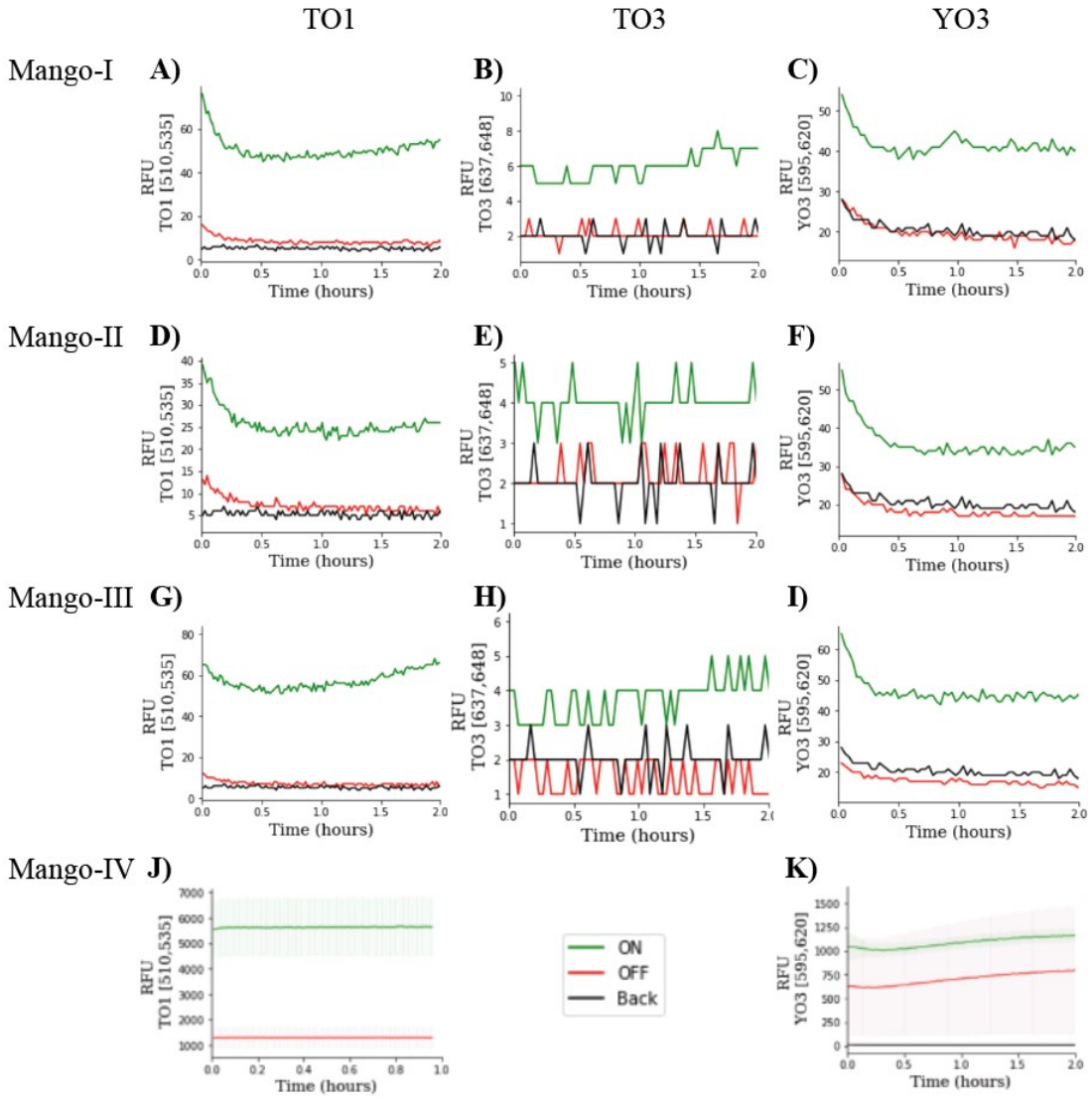

Figure 2.2 | Top performing Mango-I, -II, -III, and -IV aptaswitches against TO1, TO3, and YO3 fluorophores. A-C) Top performing Mango-I aptaswitches with TO1, TO3, and YO3. **D-F)** Top performing Mango-II aptaswitches with TO1, TO3, and YO3. **G-I)** Top performing Mango-III aptaswitches with TO1, TO3, and YO3. **J-K)** Top performing Mango-IV aptaswitches with TO1 and YO3.

From this screening, it is observed that there is no signal detection using TO3 with a Mango-I, -II, or -III based aptaswitch. However, for Mango-I, -II, -III, and -IV it appears

that of the best performing aptaswitches, the greatest fold change fluorescence all occurs with TO1. Additionally, the OFF signal is equal to the background fluorescence level, indicating no signal leakage. The best performing aptaswitches, in terms of fluorescent intensity, with Oxazole Yellow 3 (YO3), occurs with a Mango-IV base aptaswitch.

For the remainder of this research, we used Mango-III(A10U) aptaswitches paired with TO1 and Mango-IV aptaswitches paired with YO3. We did not continue to use Mango-I or -II based aptaswitches, because neither were able to interact with TO3, performed better than Mango-III(A10U) with TO1, or achieved the same fluorescent intensity with Mango-IV and YO3.

While there is a measurable difference between the ON and OFF channels for aptaswitch fluorophore pairs, apart from TO3 interactions, the fold change ratio for these platforms can be improved. To optimize performance of the aptaswitch in the reaction, we would like to determine if changing the concentration of the aptaswitch will improve fold change. In this set of experiments the aptaswitch concentration varies, while the target concentration is set to 1 μM and fluorophore to 2.5 μM. **Figure 2.3-A** shows the time course curve for a Mango-III aptaswitch with TO1. The Mango-III aptaswitch was transcribed for 1.5 hours and then mixed as the limiting reagent with excess fluorophore and target. While the aptaswitch does generate a high fluorescent ON signal, there is considerable leakage.

To observe whether the concentration of the aptaswitch without RNA purifying has any effect on output signals, we varied the transcription time of the Mango-III aptaswitch and added DNase enzyme to the transcription (**Fig 2.3-B**). We assumed that the longer we

transcribe the aptaswitch, the greater its concentration will be up until all the transcription reagents have been consumed. The DNase enzyme was added to remove the aptaswitch DNA template, which we hypothesized was causing signal leakage as a contaminant. We observe that a 15-minute transcription (**Fig 2.3-C**) of the aptaswitch performs better by reducing leakage than a longer 2-hour transcription which has a relatively higher ON and OFF fluorescence (**Fig 2.3-D**). While having fewer aptaswitches may seem counter-intuitive to a greater fold change, this does follow other observed behaviors that RNA at high concentrations forms duplexes[64]. What this means is that a high concentration of aptaswitches can produce a strong ON signal with a target, but when there is no target present, aptaswitches may bind to each other, causing high leakage and therefore a low fold change.

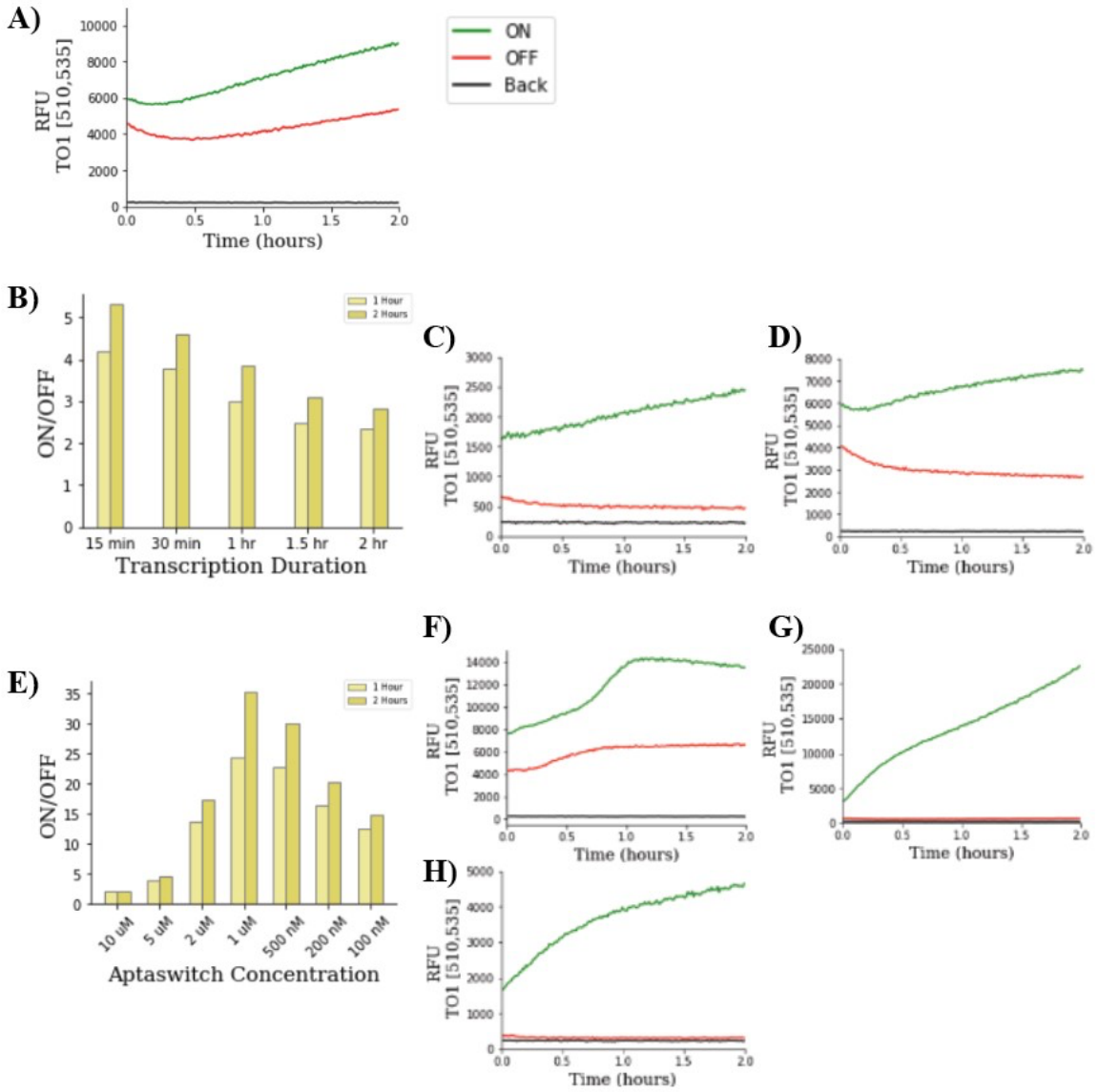

Figure 2.3 | Mango-III aptaswitch optimization through purification methods. A) Unpurified Mango-III aptaswitch, transcribed for 2.5-hours paired with TO1. **B)** Fold change of Mango-III aptaswitch at different unpurified concentrations by varying aptaswitch transcription times with added DNase. **C)** Time course curve for Mango-III aptaswitch with a 15-minute transcription. **D)** Time course curve for Mango-III aptaswitch with a 2-hour transcription. **E)** Fold change of Mango-III aptaswitch at different RNA purified concentrations. **F)** Time course curve for Mango III aptaswitch set at 10 μM. **G)** Time course curve for Mango-III aptaswitch set at 1 μM. **H)** Time course curve for Mango-III aptaswitch set at 100 nM.

Next, we checked whether RNA column purification impacts aptaswitch performance (**Fig 2.3-E**). The aptaswitch underwent overnight transcription and was purified and diluted to

stock concentrations. Because we purified the aptaswitch before the reaction, we were able to measure and set the concentration of the devices. Interestingly, unlike our observation with unpurified concentration variation, where low concentrations perform better, with purified aptaswitch there is a maximization of aptaswitch performance at 1 μM (**Fig 2.3-G**). In this case, we observe that when the aptaswitch is set very high at 10 μM (**Fig 2.3-F**), there is a very strong ON signal generated, but there is also considerable signal leakage which reduces performance, like the high concentration unpurified aptaswitch. When the concentration is very low at 100 nM (**Fig 2.3-H**), there is essentially no leakage, but by virtue of having less aptaswitch the relative fluorescence and fold change is lower, like the low concentration unpurified aptaswitch. We find that when the aptaswitch and target are equimolar, both set at 1 μM with an excess fluorophore, we achieve fold change maximization balancing low leakage with a high ON signal.

There is an agreement between purified and unpurified signal generation and leakage at high and low aptaswitch concentrations. However, RNA purification seems to provide more than just controlling aptaswitch concentrations, it also improves the platform performance. When comparing the fold change between unpurified and purified aptaswitches, the purified aptaswitches have a three to ten times improvement in the ON-OFF ratio, except for the high concentration purified aptaswitches set to 10 and 5 μM. We hypothesize that the transcription enzymes and buffers impact the aptaswitch by interfering with target binding and TMSD activation. By removing the proteins and buffer via RNA column purification, the aptaswitch performance improves.

2.4 Isothermal Amplification of Viral Targets

We investigated the use of RT-LAMP as an isothermal amplification method for viral RNA. In past troubleshooting of the RT-LAMP method, we identified 67 ºC as the optimal temperature for maximum amplicon production. Because RT-LAMP produces concatemer amplicons, final amplicon concentrations cannot be directly measured with NanoDrop. To observe the successful amplification of a viral target from RT-LAMP, we run an agarose gel electrophoresis. The characteristic laddered bands observed in the gel serve as an indicator for the presence of the RT-LAMP concatemer amplicons. When comparing the production of amplicons, the darker bands in the gel indicate a higher concentration of product.

To identify the best-performing RT-LAMP primer mixes, we screened for the LoD of Beta (Control 16) and Omicron (Control 48) variants from Twist Bioscience SARS-CoV-2 RNA Controls for different primer mixes. The best LoD for screened primers of SARS-CoV-2 Beta (**Fig 2.4-A**) and Omicron (**Fig 2.4-B**) variant targets are 5 copies per reaction and 20 copies per reaction or 0.25 copies/µL and 1 copy/µL respectively. Other reported RT-LAMP-based detection methods for SARS-CoV-2 RNA amplification reported a LoD ranging from 0.08 to 100 copies/µL[2].

In addition to testing RT-LAMP amplification of viral targets, we also tested the amplification of 18s ribosomal RNA (rRNA) as a human positive control biomarker. In a 10-fold dilution series, 18s rRNA saliva sample amplification was achieved down to 10^4 dilution and a synthetic 18s rRNA target in the femtomolar range (**Fig 2.4-C**).

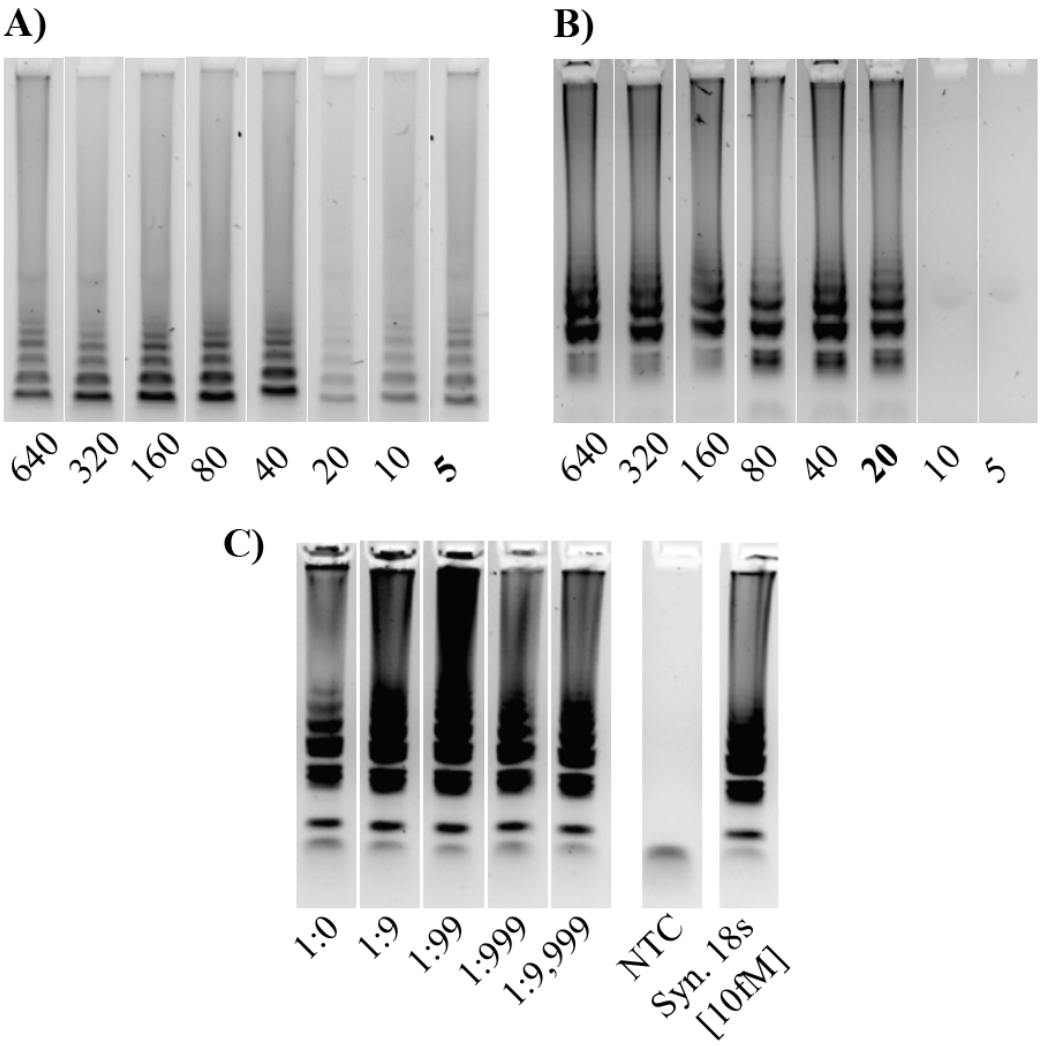

Figure 2.4 | Limit of Detection for SARS-CoV-2 variants. A) Agarose gel electrophoresis of Beta variant RT-LAMP amplicons. **B)** Agarose gel electrophoresis of Omicron variant RT-LAMP amplicons. Values are in viral RNA copies per reaction, bolded values indicate the LoD. **C)** Agarose gel electrophoresis of saliva sample 18s rRNA dilution series.

See **Appendix B** for LoD gels for Beta (**Fig B.1**) and Omicron (**Fig B.2**) variants screened, and RT-LAMP protocol (**Table B.1**).

2.5 Two-Pot Reaction Platform

With an amplification method verified (Section 2.4) and a fluorescence readout method designed and optimized (Section 2.3), we now coupled the amplification of target RNA

with the fluorescence detection of the amplicon. **Figure 2.5-A** outlines the two-pot platform method where the amplification and detection reactions occur in separate tubes. In the first tube, RNA targets undergo RT-LAMP amplification at 67 ºC for 30 minutes. The amplicon product is then transferred to the detection tube, mixed with aptaswitch and fluorophore, during which detection of the amplicon is observed. Detection of Omicron amplicon (**Fig 2.5-B**) with Red Broccoli-OBI and 18s rRNA amplicon (**Fig 2.5-C**) with Broccoli-DFHBI-1T readout were demonstrated with this two-pot method.

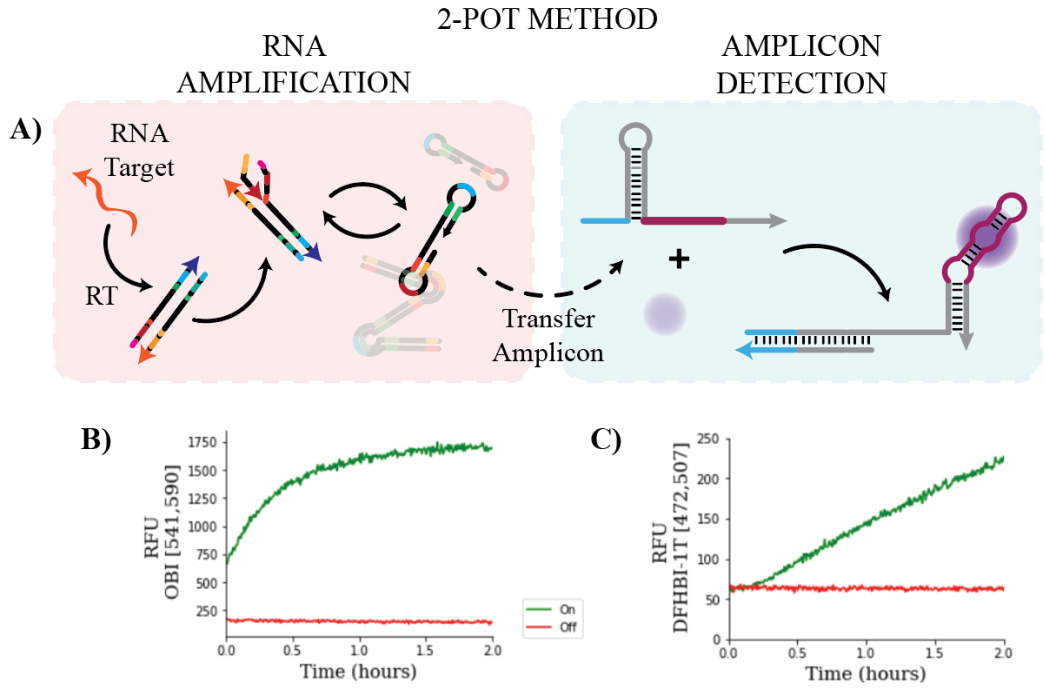

Figure 2.5 | Two-Pot method coupling RT-LAMP with aptaswitch detection. A) Two-Pot method, 1st pot RT-LAMP amplification method to output amplicons. 2nd pot transfer amplicon to aptaswitch detection method to output fluorescence. **B)** Omicron target with Red Broccoli-OBI fluorescence output from two-pot method. **C)** Saliva sample 18s rRNA target with Broccoli-DFHBI-1T fluorescence output from two-pot method.

For 18s rRNA two-pot detection, the rate of fluorescence activation is relatively slow compared to Omicron achieving almost five-fold change after two hours of signal measurement. At time zero, the ON and OFF signal start at the same fluorescence intensity

because the readout measurements occur just after the amplicon is mixed with the aptaswitch and fluorophore.

2.6 One-Pot Reaction Platform

The two-pot method is streamlined to be operationally simpler with a rapid signal readout in a one-pot method. The one-pot method incorporates the aptaswitch and fluorophore in the RT-LAMP mix and incubates all materials at 67 ºC for 30 minutes and then transfers this one-pot into the plate reader for immediate signal readout (**Fig 2.6-A**). At the 67 ºC incubation, the aptaswitches cannot detect the amplicons that are being produced, since the thermal energy at this temperature causes all aptaswitches to form a linear state. After the amplification step, the reaction is cooled down and read at 37 ºC, the temperature at which the aptaswitches adopt their secondary structure confirmation and can immediately bind to the amplicon. Detection of Omicron amplicon (**Fig 2.6-B**) with Red Broccoli-OBI and 18s rRNA amplicon (**Fig 2.6-C**) with Broccoli-DFHBI-1T readout were demonstrated with this one-pot method.

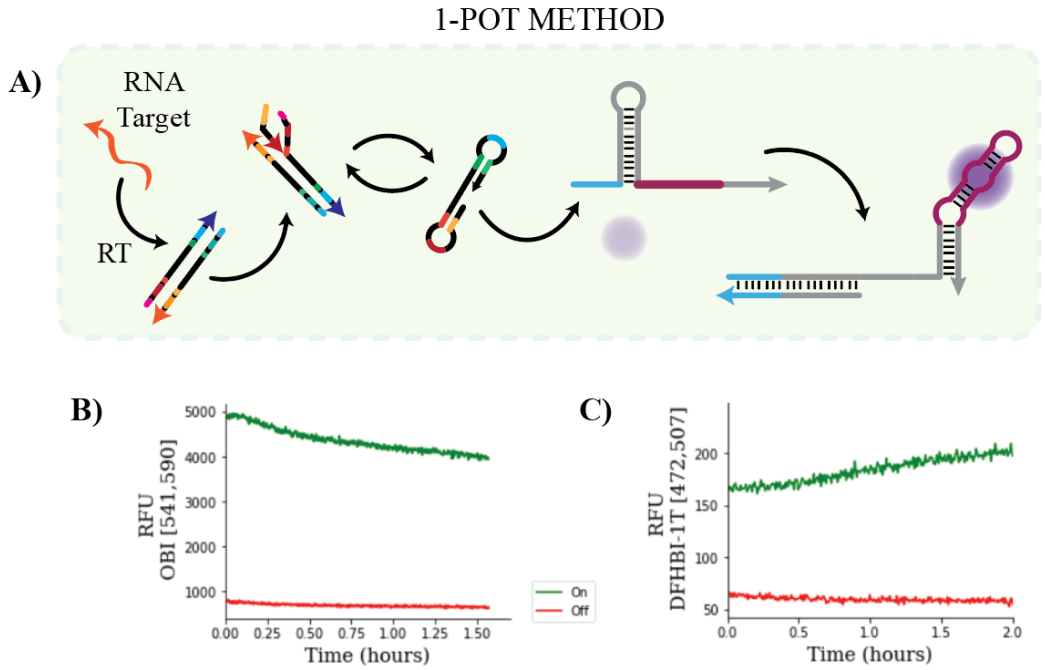

Figure 2.6 | One-Pot method coupling RT-LAMP with aptaswitch detection. A) One-Pot method, RT-LAMP amplification occurring simultaneously with aptaswitch detection. **B)** Omicron target with Red Broccoli-OBI fluorescence output from one-pot method. **C)** Saliva sample 18s rRNA target with Broccoli-DFHBI-1T fluorescence output from one-pot method.

For the detection of the 18s rRNA in **Figure 2.6-C**, we demonstrated not only the detection of 18s rRNA, but the complete pipeline of detecting RNA from unpurified and untreated saliva sample. During this single 30-minute incubation period, the RNA in the saliva sample is heat extracted and amplified all at RT-LAMP temperature and is immediately detectable when cooled down. Unlike the two-pot method, in the one-pot method a measurable difference in fluorescence level is observed at time zero because the aptaswitch and fluorophore have been thoroughly mixed in the high thermal kinetic energy amplification step prior to reading.

Chapter 3

ASSEMBLY OF MULTIPLEXED PLATFORMS FOR DETECTION AND DISTINGUISHMENT OF VIRUSES OF INTEREST

In this chapter, we will review the challenges and the significant motivations for multiplexed diagnostics to target mosquito-borne viruses (Section 3.1). To create multiplexed platforms, we start by screening a large library of aptaswitches against six viral targets (Section 3.2). Once the top-performing aptaswitches have been identified, we then assemble and optimize them into highly orthogonal multiplexed platforms (Section 3.3). **Figure 3.1** maps the multiplexing platform assembly workflow from aptaswitch screening (**Fig 3.1-A**) to triplicate verification (**Fig 3.1-B**) and finally platform assembly (**Fig 3.1-C**).

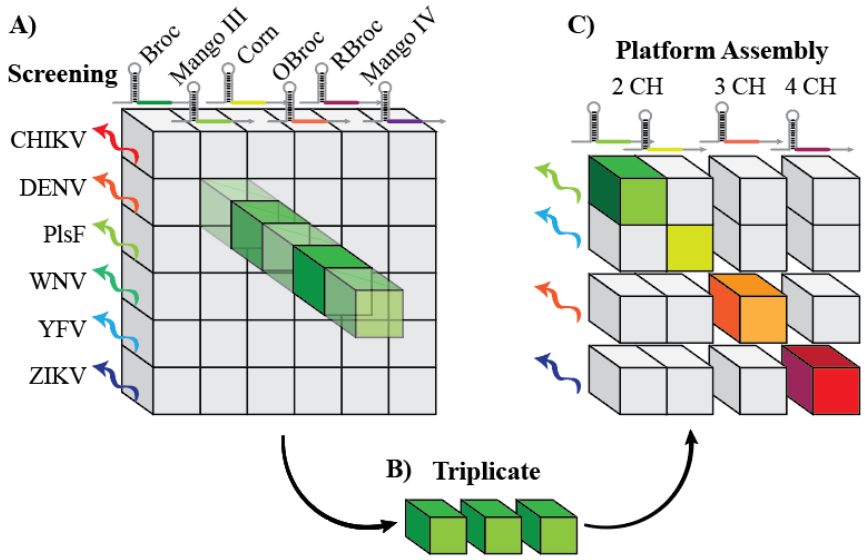

Figure 3.1 | Multiplex platform assembly workflow. A) Variety of aptaswitch designs screening per aptaswitch type per viral target: Broccoli (Broc), Mango-III, Corn, Orange Broccoli (OBroc), Red Broccoli (RBroc), and Mango-IV against CHIKV, DENV, PlsF, WNV, YFV, and ZIKV. **B)** Best performing aptaswitches verified in triplicates. **C)** Multiplexing platform assembly to maximize cross-channel orthogonality.

3.1 Motivation for Multiplexed Detection of Mosquito-borne Viruses

As explored in case studies described in Chapter 1, the accurate diagnosis of several mosquito-borne viruses presents many challenges due to symptomatic and geographic overlap. With viruses like CHIKV, DENV, and ZIKV which have similar acute symptoms, patients can be easily misdiagnosed, and viruses can circulate silently behind the outbreak of another[7],[16],[39],[66]. A consequence of misdiagnosing mosquito-borne viruses is not only the treatments may be ineffective, but the time to react to symptomatic escalations is limited[16]. During the acute phase, non-specific symptoms that are common to several viruses, from anorexia to vomiting, are present[5-7],[9-11],[14],[16],[17],[39],[66-69]. For severe or critical cases, viruses can be identified by symptomatically unique presentations, but by that point it may be too late to diagnose a patient. If the disease advances suddenly from its acute to severe form without being correctly identified beforehand, the failure to quickly react to the onset of virus-specific symptoms, like dengue shock syndrome or cerebral malaria, can be fatal[8],[10],[16],[20].

The global impact these viruses have also makes diagnoses difficult. From case studies of DENV outbreaks in India, the massive near-global presence that DENV has demonstrated to overshadow the management and resources for less pervasive viruses like CHIKV that are often misdiagnosed as DENV[5],[10],[14],[15]. High-impact pathogens like DENV[8],[10],[13],[23] and Malaria[20] that have millions of reported cases a year may inadvertently mask the true extent of other viruses like CHIKV, WNV, YFV, and ZIKV[7],[14],[15],[39].

For mosquito-borne viruses and pathogens, the difficulty in detection is not only that these diseases have similar clinical presentations, but they also have overlapping geography[7],[16]. The significance of geographic overlap for diagnoses is that there is a reasonable expectation that a patient with an ambiguous set of symptoms could realistically be infected with any one (or multiple) of several viruses[8]. In contrast to a patient who has several possible diagnoses, but only has a common geography with one virus, all the other possible diagnoses could be ruled out in favor of the more likely local transmission.

A root cause of why mosquito viruses have geographic overlap is that many are carried by the same mosquito vector, which itself is capable of being co-infected, enabling the co-circulation and infection of several viruses at once[4],[6],[7],[11],[13],[14],[16],[17],[23],[39],[66],[67]. The effects of climate change are predicted to increase not only the latitude of habitable zones, but also the altitude, exposing these mosquitoes to new environments[10],[16],[23]. The presence of virally infected mosquitos in communities that have been previously isolated and without acquired functional immunity can have significant consequences. If the spread of a novel virus is masked under traditionally local viruses and infections, the new virus may go unreported and early steps to prevent a new virus from going endemic may be missed. Multiplexed diagnostics is not only important for the six mosquito-borne pathogens we are studying, but in the future may be important in concerted detection of previously unassociated viruses.

Table 2 summarizes the need for multiplexed detection of mosquito-borne viruses and pathogens due to common mosquito vectors, geographic presence, and shared acute phase symptoms.

Table 2 | Mosquito-Borne Viruses and Pathogens Summary

Disease	Mosquito Vectors	Number of Countries Present	Estimated Cases (year)	Symptoms shared by 2 or more diseases	Ref.
CHIKV	*Ae.egypti* *Ae.albopictus*	60+	1.4-6.5 million (2005)	Anorexia Arthralgia Arthritis Encephalitis Fever Gulliane Barre Syndrome Headache Hemorrhage Muscle pain Myalgia Nausea Rash Retro-orbital pain Swollen joints Vomiting	[4],[5],[7], [11],[14],[17], [66],[67]
DENV	*Ae.egypti* *Ae.albopictus* *Ae.polynesiensis*	128	100 million (2020)		[7-17],[23], [39],[66]
Malaria	*An.stephensi*	85	241 million (2020)		[20],[69]
WNV	*Cx.pipiens*	Nearly global	N/A		[11],[68],[70]
YFV	*Ae.egypti*	47	200 thousand (2012)		[11],[68],[71]
ZIKV	*Ae.egypti* *Ae.africanus* *Ae.albopictus*	89	7 thousand (2015)		[6],[7],[17], [39],[68],[72]

3.2 Screening Aptaswitches for Viral Detection

The first step towards creating a multiplexing platform, is screening a large library of aptaswitches. For each of the 36 combinations of aptaswitch type (6 aptaswitches) and virus (6 targets), we generated 6-12 unique designs and screened over 200 aptaswitches in high throughput. **Figure 3.2** shows the results of all the Broccoli aptaswitch designs screened against each of the six viral targets (**Fig 3.2-A,C,E,G,I,K**), as well as each respective viral target's best performing aptaswitch time course curve (**Fig 3.2-B,D,F,H,J,L**). The screening data is measured at the one-hour time-point since the reaction was mixed.

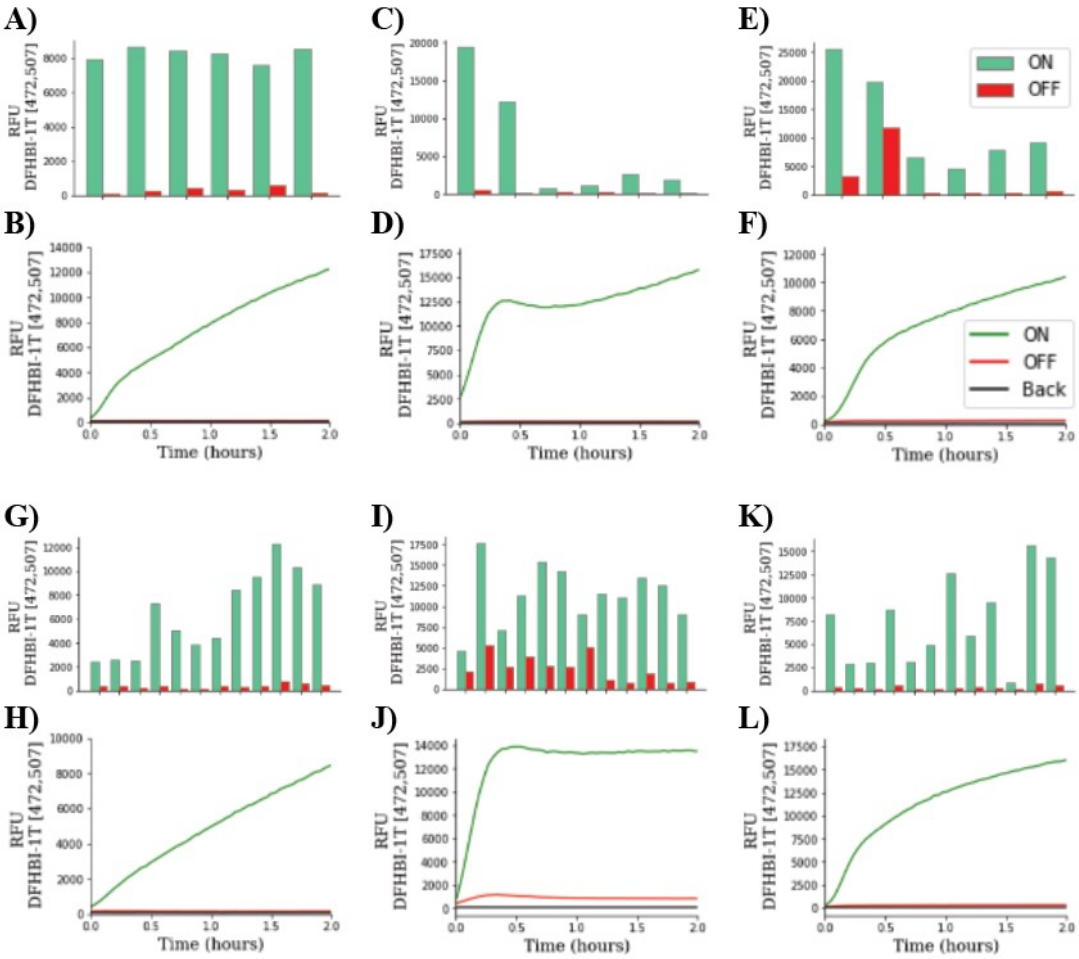

Figure 3.2 | Viral screening against Broccoli aptaswitch library. A) Broccoli aptaswitches screened against CHIKV target. **B)** Time course curve of best performing Broccoli aptaswitch against CHIKV. **C)** Broccoli aptaswitches screened against DENV target. **D)** Time course curve of best performing Broccoli aptaswitch against DENV. **E)** Broccoli aptaswitches screened against PlsF target. **F)** Time course curve of best performing Broccoli aptaswitch against PlsF. **G)** Broccoli aptaswitches screened against WNV target. **H)** Time course curve of best performing Broccoli aptaswitch against WNV. **I)** Broccoli aptaswitches screened against YFV target. **J)** Time course curve of best performing Broccoli aptaswitch against YFV. **K)** Broccoli aptaswitches screened against ZIKV target. **L)** Time course curve of best performing Broccoli aptaswitch against ZIKV.

As we can see from the screening data, not all designs perform the same, and the activation speed, signal leakage, and fluorescent intensity vary. From this screening, and the remaining five aptaswitch screenings, (see **Appendix C**, **Figures C.1-5**) the top 36 aptaswitch-target pairings have been identified. Next, we re-ran the top performing

reactions in triplicate to establish a sense of consistency for each reaction, get a fuller picture of each reaction's kinetics and leakiness, and directly compare aptaswitches against each other. **Figure 3.3** shows the triplicate verification of the previously identified top performing Broccoli aptaswitches for the six targets.

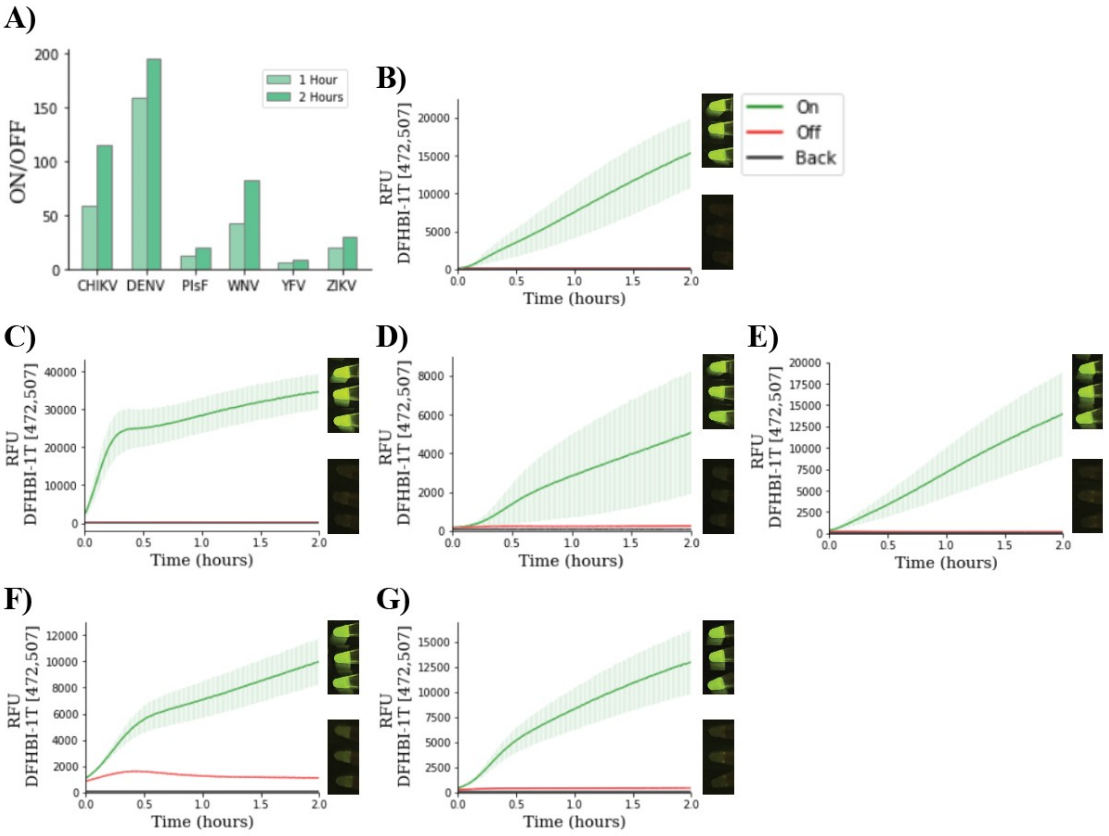

Figure 3.3 | Top performing viral targeting Broccoli aptaswitches in triplicate. A) Mean fold change of top performing viral targeting Broccoli aptaswitches. **B)** Time course curve of top Broccoli aptaswitch against CHIKV. **C)** Time course curve of top Broccoli aptaswitch against DENV. **D)** Time course curve of top Broccoli aptaswitch against PlsF. **E)** Time course curve of top Broccoli aptaswitch against WNV. **F)** Time course curve of top Broccoli aptaswitch against YFV. **G)** Time course curve of top Broccoli aptaswitch against ZIKV. The shaded region in the time-course curve is the standard deviation around the mean signal for that channel. Top fluorescent image for each group is ON triplicate, bottom image is OFF triplicate.

From **Figure 3.3-A**, we get a sense that for the Broccoli aptaswitches, the best platforms are with the CHIKV (**Fig 3.3-B**), DENV (**Fig 3.3-C**), and WNV (**Fig 3.3-E**) targets. These

targets achieve a fold change signal above 50 after one hour. After all the reactions reached an equilibrium state, where fold change was maximized, they were transferred from the 96 well plates to PCR tubes and photos observing their fluorescence was taken on the transilluminator. For each reaction shown in **Figure 3.3**, the top three tubes with green fluorescence are the ON state in triplicate and the bottom three tubes are the OFF, or NTC, in triplicate. While the PlsF (**Fig 3.3-D**), YFV (**Fig 3.3-F**), and ZIKV (**Fig 3.3-G**) reactions do not have as high of a fold change signal as the other three platforms, we can still see a qualitative difference in target detection based on the transilluminator images.

From this triplicate verification, and the other five aptaswitches' triplicate verifications (**Figures C.6-10**) we can get a sense of which aptaswitches should be used per target and begin organizing multi-channel platforms.

3.3 Multiplexed Platform Assembly

There are several considerations based on aptamer-fluorophore interactions that guide how we choose which top performing aptaswitches to combine to create a highly orthogonal multiplexing platform. We consider a highly orthogonal platform to be one where the fluorescence in a channel produced by the presence of a non-cognate target (a target that is not supposed to trigger that channel's aptaswitch) to be near equal to that channel's no target control. Because both Corn and Orange Broccoli aptamers use DFHO, albeit with different spectral properties, they should not be combined into the same platform due to cross-channel noise. Aptamers that have similar fluorophore binding mechanisms like the Mango family aptamers Mango-III and Mango-IV should not be mixed[59]. As

demonstrated back in **Figure 2.2**, both Mango-III and Mango-IV are capable of binding to TO1 and YO3 and therefore activation of one aptaswitch could produce fluorescence signal in the other channel. For aptamers like Mango-III and Orange Broccoli, there is concern about spectral overlap, their excitation wavelength is only 3 nm apart from each other[34]. In the plate reader machine, a laser scans the well plates with the reactions centered at the excitation wavelength with some level of variance. In a platform that contains both Mango-III and Orange Broccoli aptaswitches, the fluorophores from both reactions could be excited at the same time and increase background noise when reading the emission measurements for each channel.

With the following considerations in mind, we first created a two-channel platform, using the Broccoli targeting DENV aptaswitch and the Corn targeting ZIKV aptaswitch (**Fig 3.4-A**). While Broccoli aptamers can bind to DFHO, they have a very poor binding affinity, and the combination of a Broccoli-Corn platform should be orthogonal[73]. For each channel, we measure a signal increase when the aptaswitch's respective targets are present. In this two-channel platform, orthogonality is also demonstrated to be very good, with non-cognate target fluorescence being nearly the same as the NTC for both channels. When all reactions reach equilibrium state, and a target is present we also observe fluorescence on the transilluminator (**Fig 3.4-D**). When only the DENV target is present, we can see a green fluorescence indicating Broccoli aptaswitch binding, and when only ZIKV target is present, we can see a yellow fluorescence corresponding to the Corn aptaswitch binding. When both targets are present however, the platform shows a yellow fluorescence nearly the same as when only ZIKV is present. This is because the relative fluorescent intensity of the Corn-

DFHO channel is much stronger than the Broccoli-DFHBI-1T channel despite both channels having the same reaction concentrations. By altering the aptaswitch and fluorophore concentrations, we can modulate each channel to achieve near equal fluorescent intensities and would expect to observe a lime green color when both targets are present.

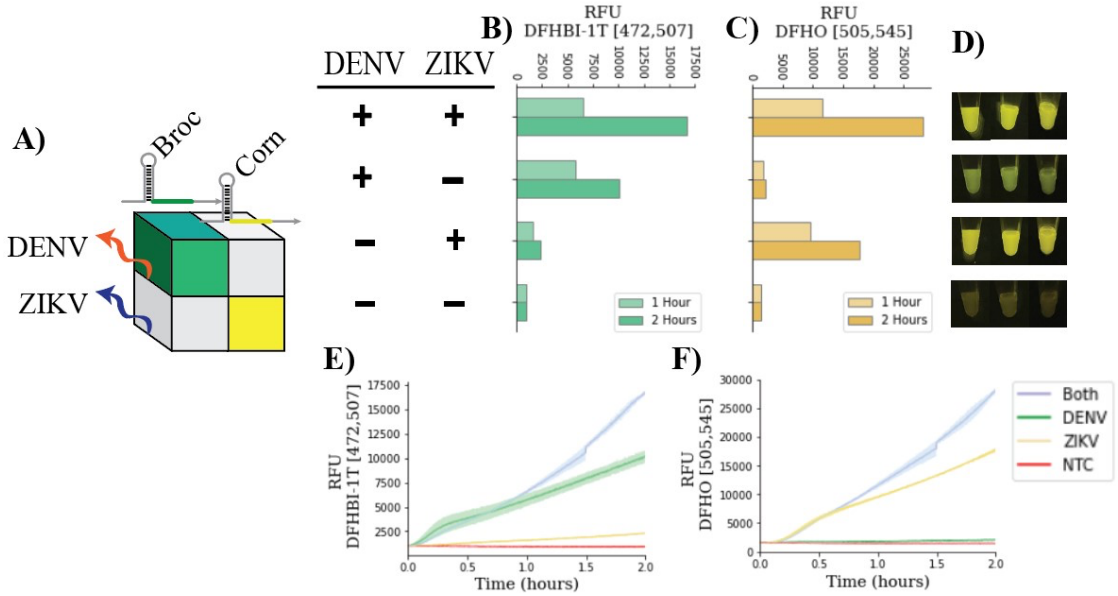

Figure 3.4 | Two channel DENV-ZIKV platform. A) Platform organization, Broccoli aptaswitch targeting DENV and Corn aptaswitch targeting ZIKV. **B)** Broccoli–DFHBI-1T channel one- and two-hour mean fluorescence. **C)** Corn–DFHO channel one- and two-hour mean fluorescence. **D)** Transilluminator images of platform performed in triplicate once all reactions reach equilibrium state. **E)** Time course curve of platform in triplicate on DFHBI-1T fluorescence channel. **F)** Time course curve of platform in triplicate on DFHO fluorescence channel.

Another two-channel platform we explored was a DENV and PlsF targeted by a Broccoli and Mango-III aptaswitches respectively (**Fig 3.5-A**). Like the DENV and ZIKV platform developed, there is an observable fluorescence upon aptaswitch activation (**Fig 3.5-D**), however the Broccoli channel does have signal leakage when mixed with the non-cognate PlsF target (**Fig 3.5-B**). Because the TO1 fluorescent activation by Mango-III is much

stronger than the DFHBI-1T activation by Broccoli, it is difficult to observe any green fluorescence from the leaky signal for the PlsF target only case. By testing out pairings of different aptaswitch-fluorophore mixes in two-channel platforms, we determined which aptaswitch-fluorophore channels are orthogonal and can be combined in higher-order platforms.

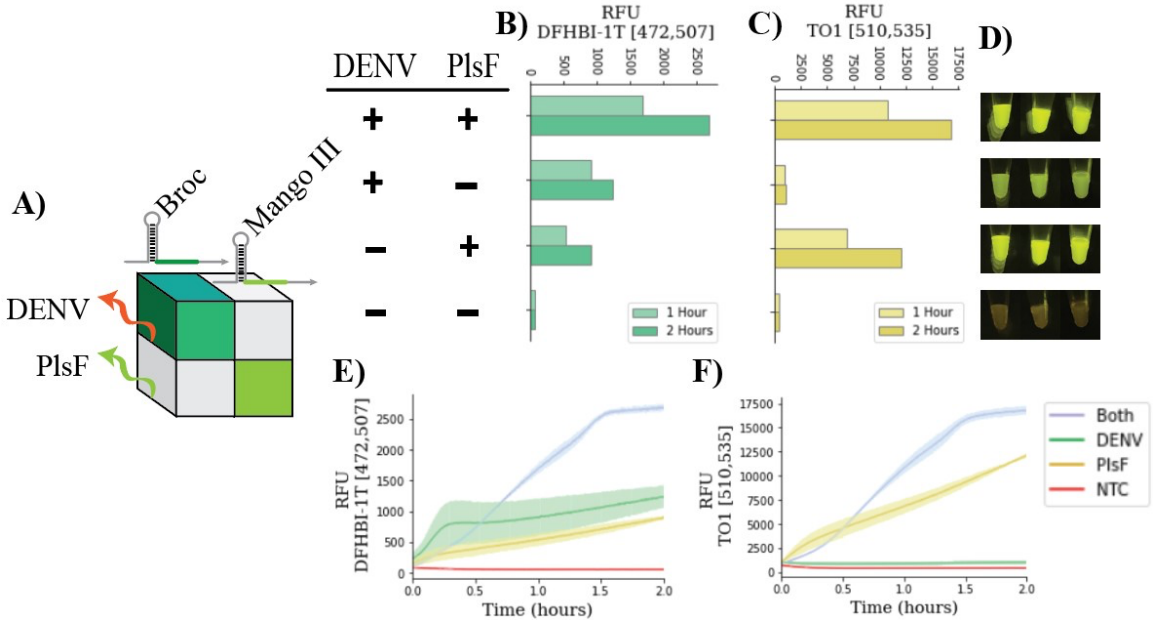

Figure 3.5 | Two channel DENV-PlsF platform. A) Platform organization, Broccoli aptaswitch targeting DENV and Mango-III aptaswitch targeting PlsF. **B)** Broccoli–DFHBI-1T channel one- and two-hour mean fluorescence. **C)** Mango-III–TO1 channel one- and two-hour mean fluorescence. **D)** Transilluminator images of platform performed in triplicate once all reactions reach equilibrium state. **E)** Time course curve of platform in triplicate on DFHBI-1T fluorescence channel. **F)** Time course curve of platform in triplicate on TO1 fluorescence channel.

With the success of the Broccoli and Corn, DENV and ZIKV platform, another channel detecting PlsF with Mango-IV aptaswitch was added to create a three-channel platform (**Fig 3.6-A**). The combination of DFHBI-1T, DFHO, and YO3 fluorophores appear to allow for a highly orthogonal platform, as there is little crosstalk, and any fluorescence that is produced in non-cognate target reactions is near the same as the NTC for that channel

(**Fig. 3.6-B-D**). In the cases where there is only one target present, we can also observe the three primary colors of this platform with each fluorophore being solely expressed (**Fig 3.6-E**). When there are two or more targets present, we can observe the mixing of different colors and shades, due to the relative fluorescent intensities across each channel being more on-par with each other compared to the previous two-channel platforms.

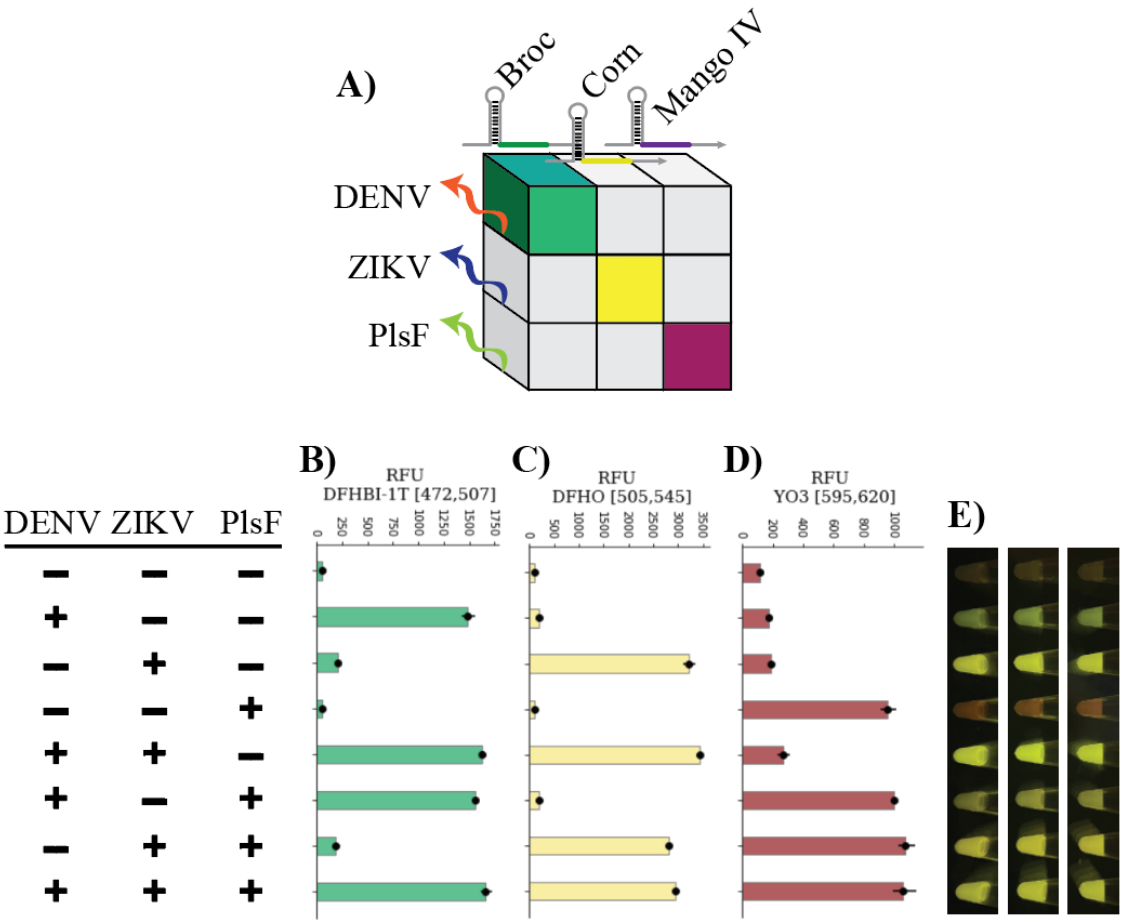

Figure 3.6 | Three channel DENV-ZIKV-PlsF platform. A) Platform organization, Broccoli aptaswitch targeting DENV, Corn aptaswitch targeting ZIKV, and Mango-IV aptaswitch targeting PlsF. **B)** Broccoli–DFHBI-1T channel mean fluorescence. **C)** Corn–DFHO channel mean fluorescence. **D)** Mango-IV–YO3 channel mean fluorescence. **E)** Transilluminator images of platform performed in triplicate once all reactions reach equilibrium state.

After the success from the three-channel platform, another channel with Red Broccoli aptaswitch targeting CHIKV was added to create a four-channel platform (**Fig 3.7-A**). Here

we also achieve distinguishable fluorescent activation, however for Broccoli and Red Broccoli aptaswitches crosstalk leakage becomes an increasing issue. Because Red Broccoli is capable of binding to DFHBI-1T we observe noise in the DFHBI-1T channel for non-cognate target reactions where at least one of the targets is CHIKV, which unlocks Red Broccoli. This noise works both ways when DENV unlocks Broccoli, which incorrectly binds to OBI.

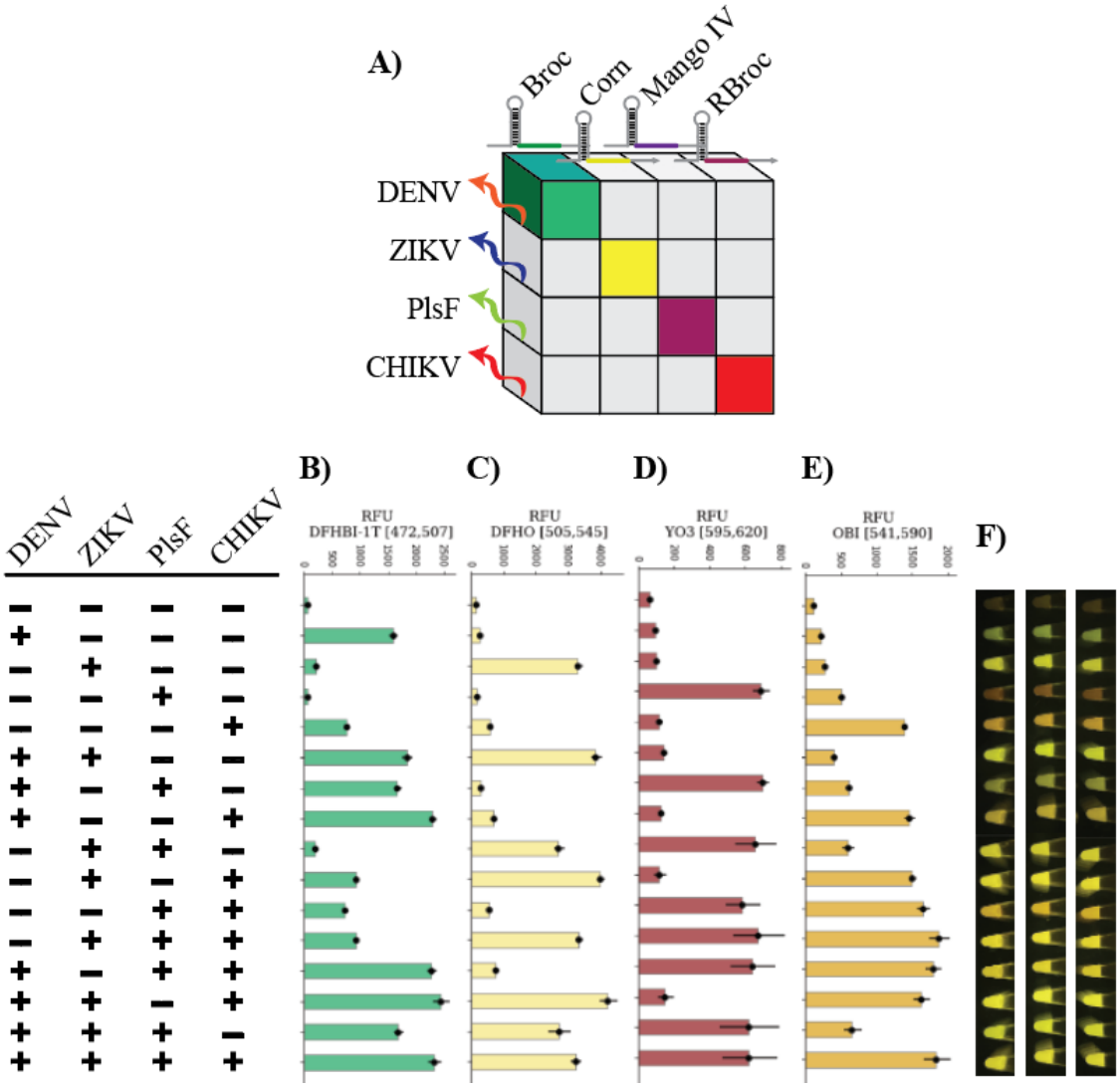

Figure 3.7 | Four channel DENV-ZIKV-PlsF-CHIKV platform. A) Platform organization, Broccoli aptaswitch targeting DENV, Corn aptaswitch targeting ZIKV, Mango-IV aptaswitch

targeting PlsF, and Red Broccoli aptaswitch targeting CHIKV. **B)** Broccoli–DFHBI-1T channel mean fluorescence. **C)** Corn–DFHO channel mean fluorescence. **D)** Mango-IV–YO3 channel mean fluorescence. **E)** Red Broccoli–OBI channel mean fluorescence. **F)** Transilluminator images of platform performed in triplicate once all reactions reach equilibrium state.

The increasing leakiness of the platforms with more channels brings up the question of how large of a platform can be assembled without compromising the fidelity of each channel. We see that even in the four-channel platform, with Broccoli, Corn, and Red Broccoli all capable of binding to each other's fluorophore, the Mango-IV crosstalk is minimal and not much greater than the fluorescence presented in the NTC on the YO3 emission channel (**Fig 3.7-D**). Despite the noise created by Broccoli, Corn, and Red Broccoli, all of which have similar binding mechanisms, Mango-IV performance does not worsen when we move from the three-channel to the four-channel platform. The key to achieving a platform that has more channels while minimizing crosstalk may be only to use aptaswitches from different aptamer families.

Chapter 4

PLATFORM OPTIMIZATION USING APTAMER-ARRAYS TO FURTHER ALIGN PLATFORMS TO POINT-OF-CARE NEEDS

In this chapter, we will consider how new aptamer-array devices can further align our platforms to POC needs (Section 4.1). We will design and test a set of multiplexing arrays and compare them to our platforms developed in chapter 3 (Section 4.2). Additionally, we will propose and consider the design and mechanism of a cascading array and how such devices may benefit diagnostic tests (Section 4.3).

4.1 Aptamer Arrays

The concept behind an aptamer array is to have multiple aptamers embedded in unimolecular structures that can provide enhanced performance or more complex functionality over individually performing aptaswitches. The goal of the aptamer arrays is to develop new aptamer-fluorophore-based detection devices that can improve on some of the limitations of the aptaswitch-based platforms by making such platforms more POC aligned.

For each channel we add to the aptaswitch platform the complexity of the system grows with more components, increased noise, slower activation speeds, and worsening orthogonality. Such aptamer array devices proposed and tested aim to reduce the number of material components in a platform, increase activation speed, and potentially reduce crosstalk noise.

4.2 Multiplexing Arrays

The idea behind the multiplexing array is to reduce the number of components in the detection platform by fusing from 5' to 3' ends of previously verified aptaswitches into a unimolecular structure (**Fig 4.1-A**). The advantage of the multiplexing array compared to an aptaswitch multiplexing platform, is that optimization of the platform becomes much simpler. For aptaswitch multiplexing, if we wanted to optimize the fluorescent intensity such that each channel produces the same signal strength when activated, we would have to adjust the concentrations of all the aptaswitches and fluorophores relative to each other. Because the aptamers in a multiplexing array have a fixed ratio that is innate to its structure, optimization of a multiplexing array platform only requires adjusting the fluorophore concentrations relative to the array. Additionally, errors like imperfect dilutions, different volumes pipetted, or varying aptaswitch degradation rates are all normalized due to the structure of the multiplexing array.

The multiplexing arrays use TMSD like the aptaswitch activation method. Theoretically, the activation of each aptaswitch embedded in the multiplexing array should be independent of the other aptaswitches in the structure. One difference in the activation mechanism of the array is that only the 5' aptaswitch in the array has a 5' toehold, while all the other fused aptaswitches have an internal toehold, which is found experimentally to not be as efficient for TMSD activation (**Fig 4.1-B**).

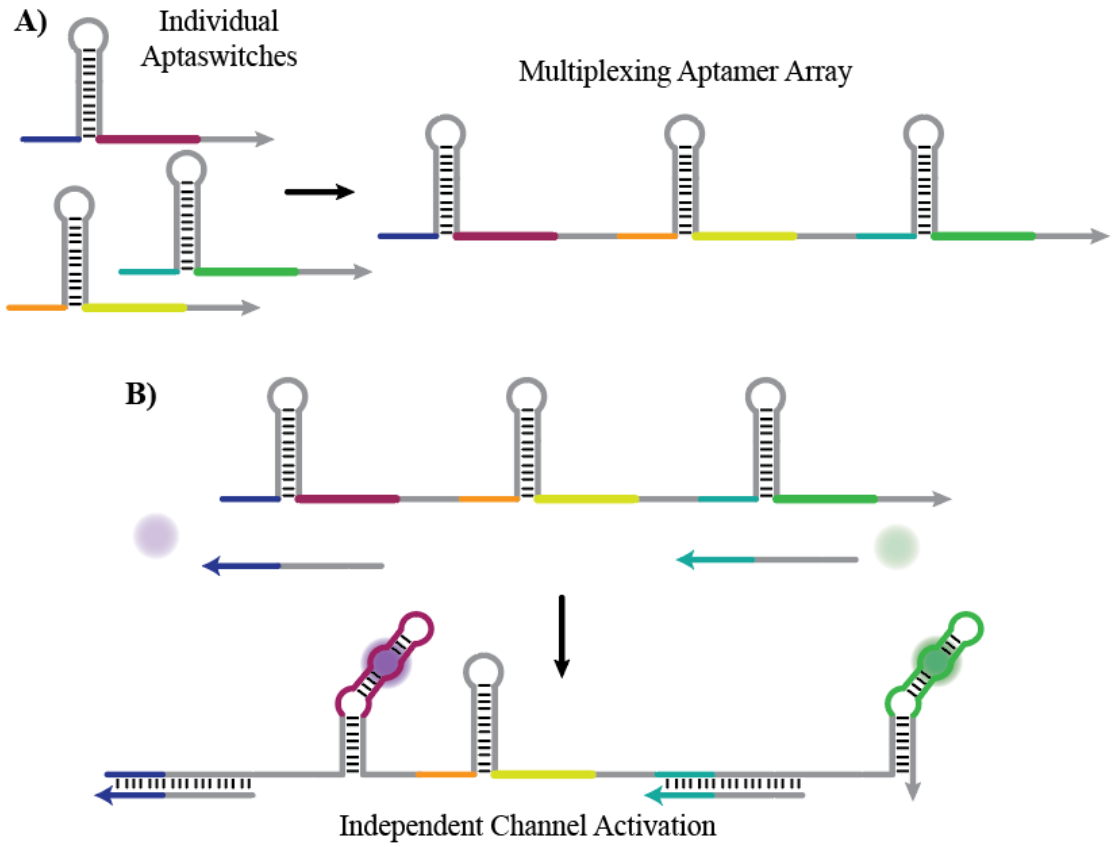

Figure 4.1 | Design and mechanism of multiplexing arrays. A) Individual aptaswitches are fused end-to-end to create a unimolecular multiplexing aptamer array. **B)** Activation of independent channels using TMSD on the multiplexing.

Figures 4.2 and **4.3**, compares the performance of the aptaswitch two-channel Broccoli Corn platform previously developed with four Broccoli-Corn multiplexing array designs. The individual multiplexing aptaswitch platform (**Fig 4.2-A-F**) performs as expected compared to previous characterization (**Figure 3.2**). The Broccoli-Corn array v.1 (BCv1) (**Fig 4.2-G-L**), where the Broccoli aptaswitch is on the 5' end, has essentially no leakage on the DFHBI-1T channel, with both the NTC and the non-cognate target reactions producing fluorescence near background levels. The same minimal signal leakage is found in the DFHBI-1T channel for the Broccoli-Corn array v.2 (BCv2) (**Fig 4.2-M-R**), however for both arrays, there is considerable signal leakage in the non-cognate target reaction in

the DFHO channel.

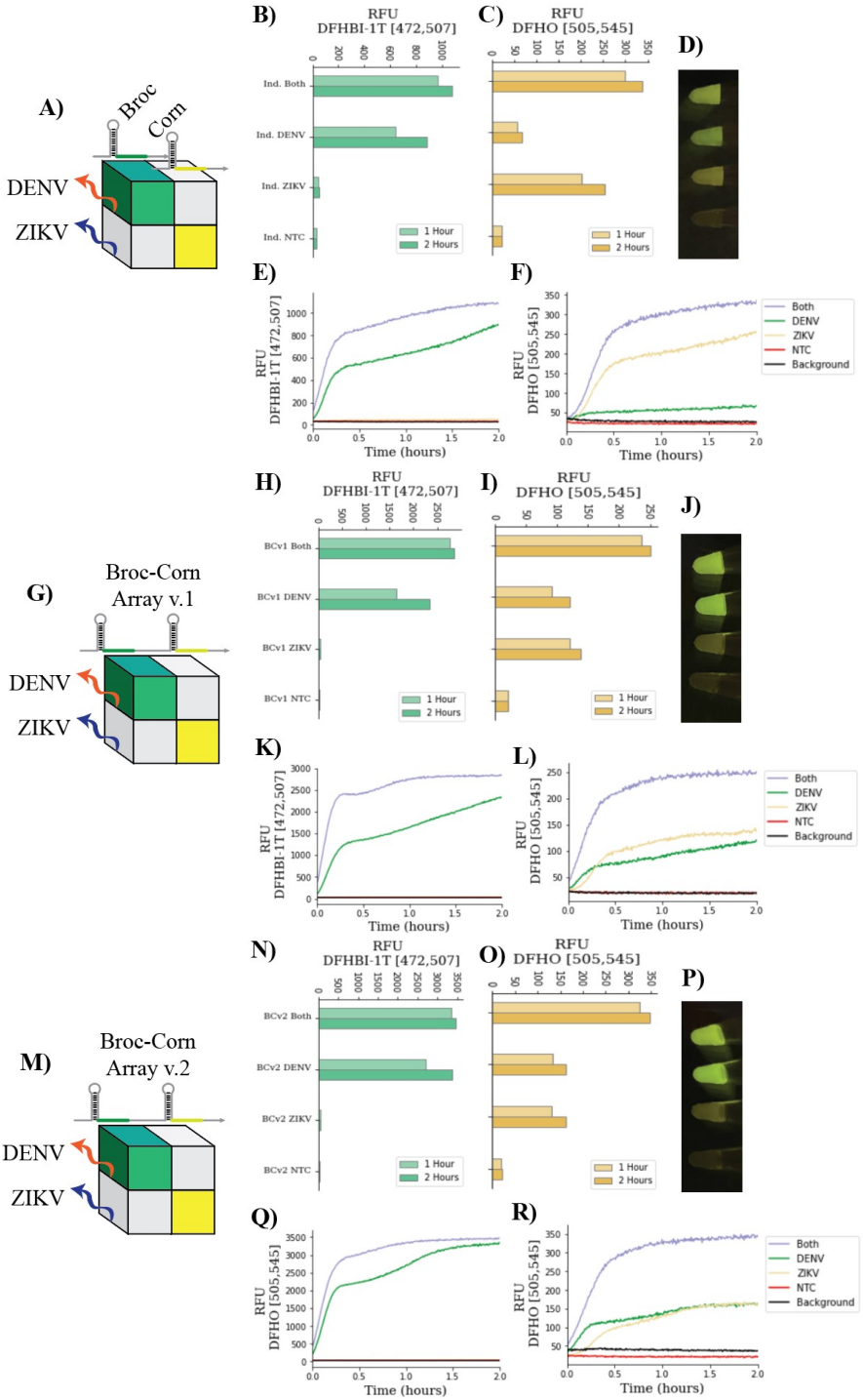

Figure 4.2 | Broccoli–Corn multiplexing arrays. A-F) Broccoli–Corn individual aptaswitch control. **G-L)** Broccoli–Corn multiplexing array design one. **M-R)** Broccoli–Corn multiplexing array design two.

When we move the Corn aptaswitch to the 5’ end of the array, in Corn-Broccoli array v.1 (CBv1) (**Fig 4.3-A-F**) and Corn-Broccoli array v.2 (CBv2) (**Fig 4.3-G-L**), there is essentially no leakage in the DFHO channel, with some leakage in the DFHBI-1T emissions. By comparing the performance of the aptaswitch platform with the four arrays when only the DENV target is present (**Fig 4.3-M**), we see that the arrays with a Broccoli aptaswitch on the 5’ end perform better than the aptaswitch control and the arrays where Broccoli has an internal toehold. The same holds true when only ZIKV target is present (**Fig 4.3-N**), with the Corn aptaswitches on the 5’ end of the array having the fastest activation, followed by the individual aptaswitches and the arrays where Corn has an internal toehold.

We can conclude from the faster activation speeds shown in **Figures 4.3-M** and **N** that a 5’ toehold does indeed have a faster TMSD activation than an internal toehold. The reason why the 5’ aptaswitches in the multiplexing arrays have a higher signal than the individual aptaswitches may be due in part to the difficulty of synthesizing larger devices, with a transcription method favoring the synthesis of the sense template over antisense. Nevertheless, what we have learned from the arrays that have been correctly synthesized does indicate a promising start towards the development more complex unimolecular devices with other functionalities.

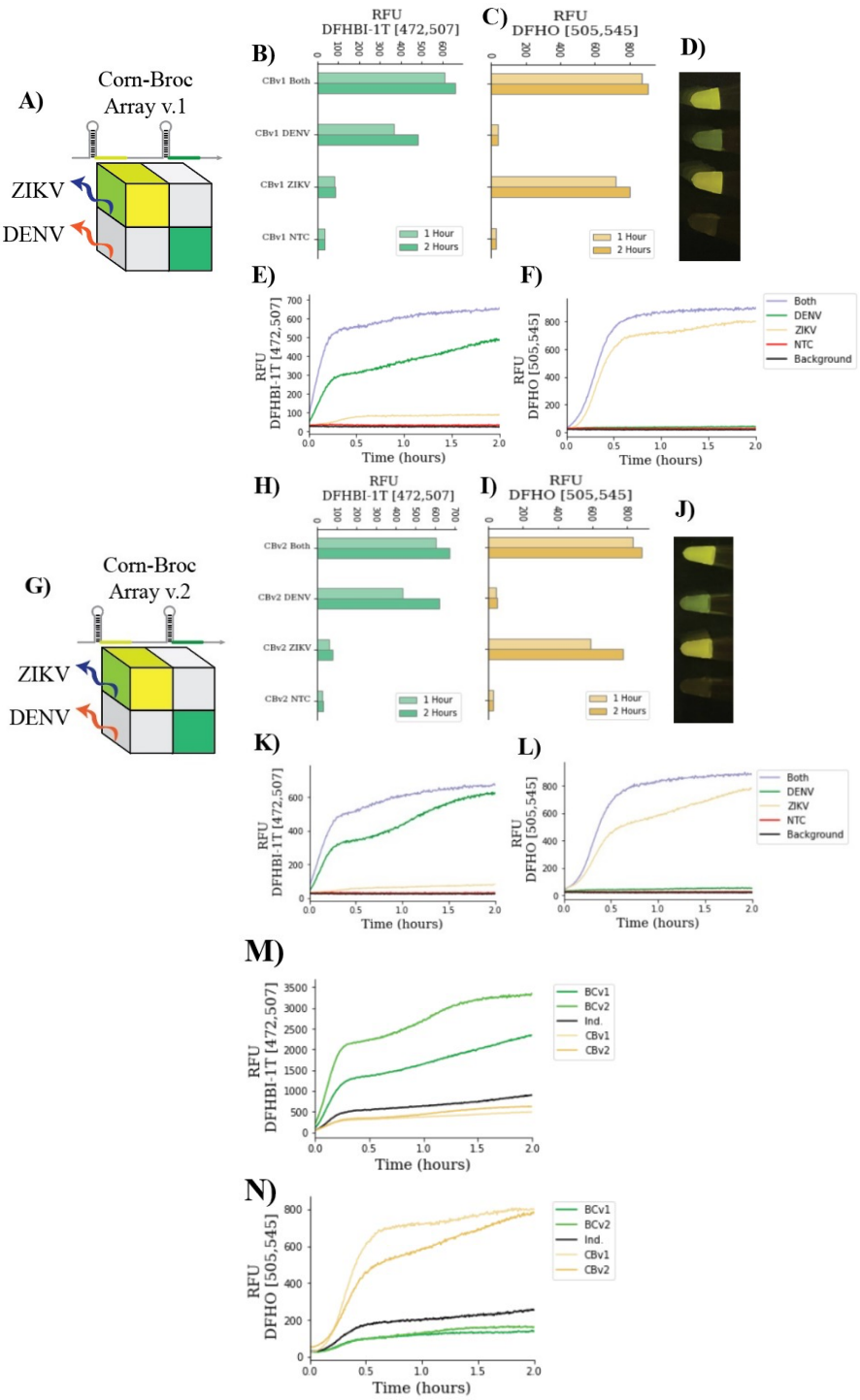

Figure 4.3 | Broccoli–Corn multiplexing arrays continued. A-F) Corn–Broccoli multiplexing array design one. **G-L)** Corn–Broccoli multiplexing array design two. **M)** DFHBI-1T channel time course curve of all Broccoli–Corn arrays and individual aptaswitch platforms with DENV target only. **N)** DFHO channel time course curve of all Broccoli–Corn arrays and individual aptaswitch platforms with ZIKV target only.

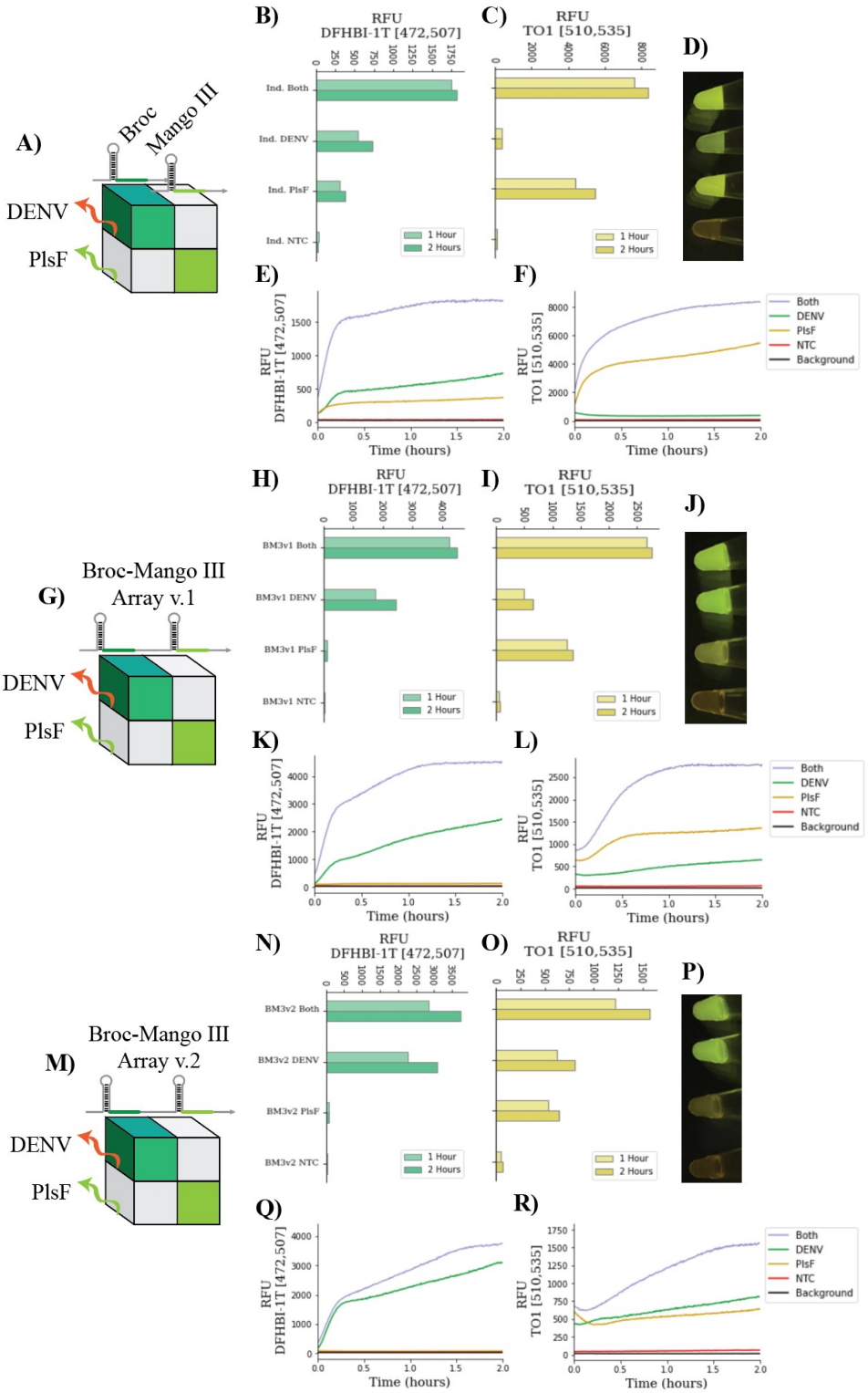

Figure 4.4 | Broccoli–Mango-III multiplexing arrays. A-F) Broccoli–Mango-III individual aptaswitch control. **G-L)** Broccoli–Mango-III multiplexing array design one. **M-R)** Broccoli–Mango-III multiplexing array design two.

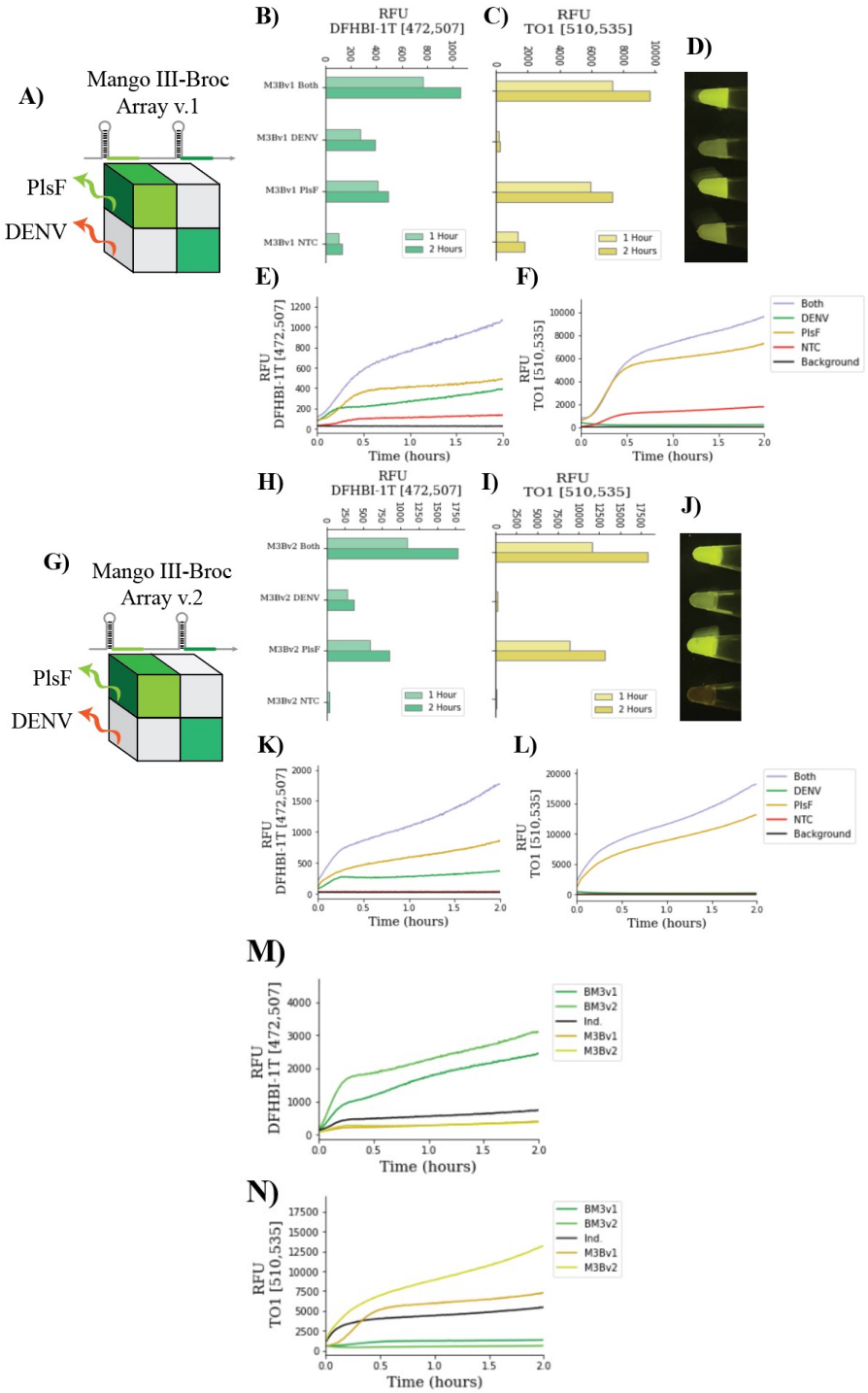

Figure 4.5 | Broccoli–Mango-III multiplexing arrays continued. A-F) Mango-III–Broccoli multiplexing array design one. **G-L)** Mango-III–Broccoli multiplexing array design two. **M)** DFHBI-1T channel time course curve of all Broccoli–Mango-III arrays and individual aptaswitch platforms with DENV target only. **N)** TO1 channel time course curve of all Broccoli–Mango-III arrays and individual aptaswitch platforms with PlsF target only.

Looking into the performance of the Broccoli-Mango-III arrays (**Figures 4.4,4.5**) we discover additional features about array mechanics that can inform future device designs.

For the Broccoli-Mango-III arrays, we see non-cognate target noise in channels where the non-cognate target is unlocking the 5' aptaswitch. What we take from this, is that when the 5' aptaswitch is being unlocked, the change in secondary structure of that aptaswitch is having downstream effects causing the aptaswitch behind it to be indirectly activated. Conversely, when the internal toehold in the array is being unlocked and that aptaswitch moves to an ON state, this change in secondary structure does not induce noise on the 5' aptaswitch as we see no or minimal non-cognate target signals in channels where the internal toehold is being unlocked. For future design considerations of the multiplexing arrays, being able to insulate noise created by 5' aptaswitches by either adding a sufficiently long spacer domain or a small sacrificial hairpin structure between each aptaswitch may help improve the platform's orthogonality.

In addition to the Broccoli-Corn and Broccoli-Mango-III arrays, we also tested Broccoli-Mango-IV (**Figures C.11**,**12**) and Mango-III-Red Broccoli (**Figure C.13**) two channel multiplexing arrays.

4.3 Cascading Arrays

The purpose of the cascading array is to increase the speed of signal readout by amplifying fluorescence when the array is activated. In all the previous platforms developed and discussed, one target unlocks one aptaswitch allowing the activation of one aptamer, the idea behind the cascading array is to improve this ratio. For the cascading array, when one

target unlocks the device, several aptamers can be turned on and the fluorescence signal induced per target is amplified (**Fig 4.6-A**).

The mechanism for the array operates first by a 5' TMSD activation unlocking a hairpin with a trans-acting target (**Fig 4.6-B**). When a target binds and strand displace the nearby hairpin structure a stabilizing stem is released however, unlike the aptaswitches, the complementary strand of that stabilizing stem is partially occluded in the next hairpin. For the stabilizing stem to hybridize, the released stem must behave as a cis-acting target unlocking the internal toehold created by the partially occluded complementary stem. The internal TMSD and hybridization of the stabilizing stem allows the first aptamer to form, and simultaneously releases the stabilizing stem for the second aptamer when the second hairpin is unlocked. The same pattern of cis-acting internal TMSD of stabilizing stems continues, cascading through the rest of the array, turning on an aptamer with each hairpin unlocked.

A key design principle for such an array to work, is that the binding energies of each consecutive hairpin (going from 5' to 3') must have a lower binding energy than the previous. If the amount of energy that is released by strand displacement of the first hairpin is less than the binding energy needed to displace the second, then the cascading effect would not move forward, thermodynamically speaking. The use of a clamp domain on the first hairpin, can help create a desired energetic landscape. The clamp domain, as previously discussed in **Section 2.1**, increases the stability and binding energy of the first hairpin. By tightly locking the stabilizing stem in the first hairpin, the clamp acts as vital domain to prevent the untriggered ON state fluorescence, whose reversable reaction back

to OFF would not be as favorable in a cascading array, causing false-positive signal accumulation.

Another design feature we can incorporate to allow an energy drop from one hairpin to the next, is by making each subsequent hairpin shorter. Because we wish to use TMSD activation, the stabilizing stem domains must be pushed down by several nucleotides for each hairpin to create an internal toehold for activation. With part of the stabilizing stem for the internal hairpins required as a toehold domain, the stems naturally get shorter and therefore have a decreasing binding energy.

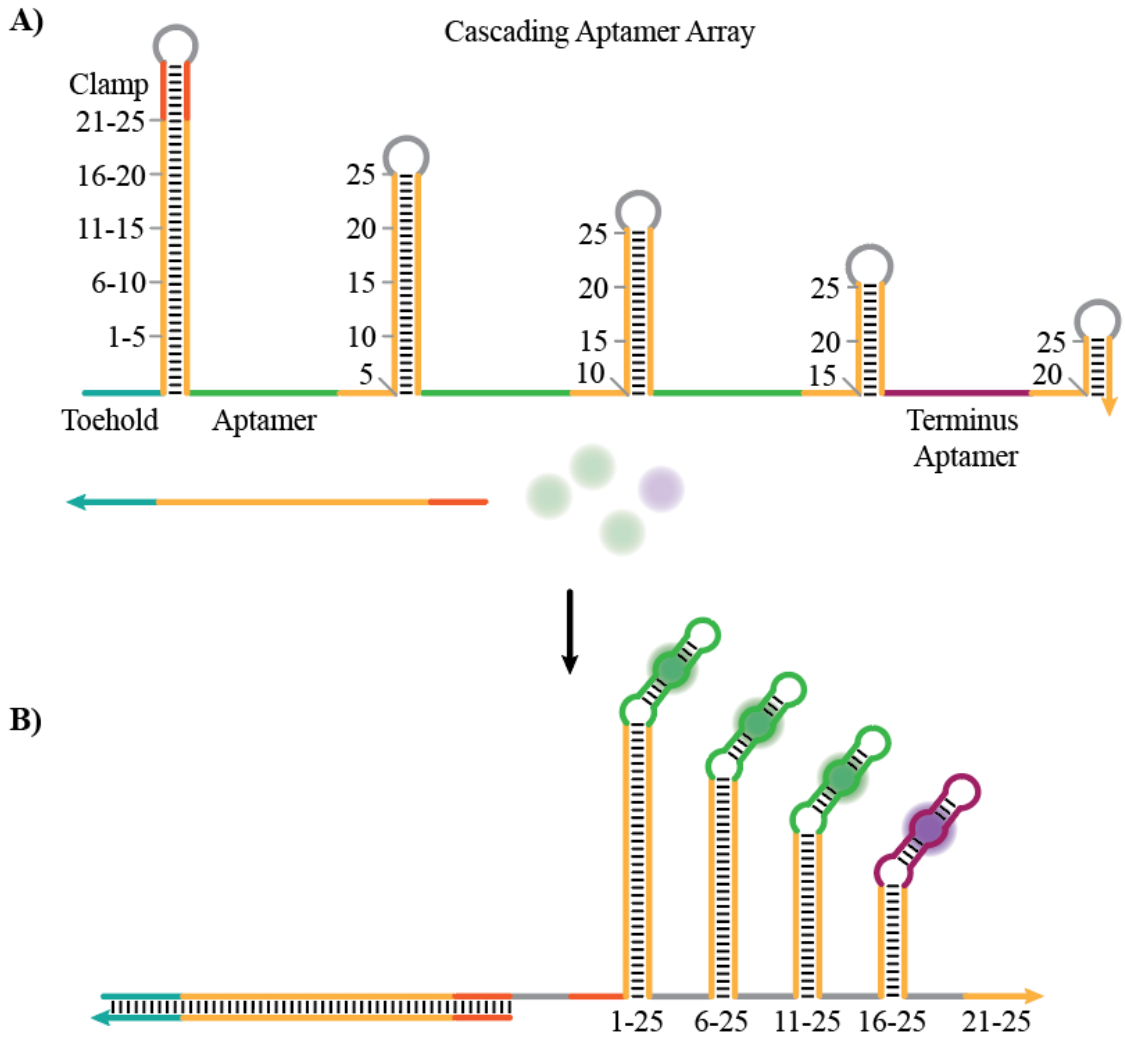

Figure 4.6 | Design and mechanism of cascading arrays. A) Design of a unimolecular cascading aptamer array. **B)** Activation of cascading array using TMSD activation of the 5' and internal toeholds.

For the development of the cascading array, we include a terminus aptamer that is different from all the other aptamers in the structure. The purpose of the terminus aptamer is to be an indicator that all previous aptamers have been successfully unlocked. The idea is that the two hairpins that are each occluding one half of the aptamer's stabilizing stem are strong enough that when there is no trans-acting target the aptamer will not form. Only

when a target is present, this final aptamer and all the aptamers upstream from it will turn on.

The cascading array if functions properly, could also increase the platform's LoD. If our platforms did not rely on a pre-amplification step, but instead interacted directly with a target then, for example, a cascading array that amplifies a signal four-fold compared to an aptaswitch should have a LoD that is four times lower.

The use of arrays increases the variety of devices possible for diagnostic detection. Using multiplexing or cascading arrays can improve a platform for POC use by potentially making an aptamer-based test cheaper, faster, and more sensitive. With arrays, the functionality of a device is not limited to only detecting a target, but with the multiple aptamers and various activation methods, such devices could perform increasingly advanced and complicated logic operations.

Chapter 5

CONCLUSION AND FUTURE DIRECTIONS

We identified in chapter one that while RT-PCR is the gold standard for diagnostics, it has significant limitations for POC testing. The consequences of lacking field-testing in low resource settings, and for overburdened laboratories during surging epidemics, have also been explored and have guided our motivations to develop a POC-aligned diagnostic detection method for viral RNAs.

In chapter two, we demonstrated a complete detection method, from RT-LAMP detection of low target concentrations of Omicron to an aptamer-based signal readout. Additionally, we demonstrated an ability to roll in the RNA extraction of human saliva 18s rRNA, into our detection method, all in a one-pot method.

Once we established our detection method, we developed multiplexing platforms of mosquito-borne viral targets in chapter three. We were able to assemble two-, three-, and four-channel multiplexing platforms, but found the fidelity of the channels and orthogonality of the platform worsened with the four-channel test.

Lastly, in chapter four, we looked to address some of the POC limitations we reached with the multiplexing aptaswitch platforms, by proposing and investigating aptamer-array devices. We tested several multiplexing array designs, which shows a promising start for diagnostic detection, if furthered refined. Additionally, we also proposed and examined the design and potential uses for a cascading aptamer array.

One next step to further this research includes investigating the use of other aptamers, like o-coral[74]. Creating new aptaswitches with novel aptamers could help improve the three- and four-channel multiplexing platforms and perhaps allow the platforms to grow to include even more channels. By incorporating different families of aptamers into a multiplexing test, the range of fluorescence output will increase. Increasing the colorimetric output will help with making a diagnosis based on visual indicators. Most of the fluorescent readouts that we have demonstrated on the transilluminator only produce various shades of green or yellow light when under the same source and filter wavelengths. The different binding mechanisms of new aptamers will also reduce the noise created during non-cognate target reactions.

With the development of a highly orthogonal multi-channel platform, the validation of the tests with patient samples will allow us to get a sense of the platform's true sensitivity and specificity and compare its utility to RT-PCR. Currently, it is difficult to comment on how this method compares to other diagnostic methods described in literature and commercially available products. In terms of speed, our one-pot method with RT-LAMP only requires a 30-minute incubation with an immediate signal readout, which is a faster process than RT-PCR. And in terms of LoD sensitivity, we have been able to demonstrate the amplification and detection of SARS-CoV-2 targets in the lower range of other published detection methods[2].

For the realization of such a method for POC applications, we would need to transfer this benchtop test into a portable system. There are several ways we could translate our method into a POC device, like making a paper-based freeze-dried reaction[18],[26],[36] or embedding

the reaction into a microfluidic chip that can be read or scanned by a phone or a digital device like a glucose monitor or pregnancy test[22].

The development of the multiplexing array, and investigation of the cascading array, may also prove to be useful devices for diagnostic testing, or at the very least teach us valuable lessons about RNA binding mechanics that can inform future aptamer-based detection devices. Other aptamer-based devices that could be developed include multiplexing detection at single-nucleotide polymorphisms or logic gates. If we modified the four-channel multiplexing test, such that we had four Broccoli aptaswitches, with each one targeting one of the four DENV serotypes, then we would effectively create an OR gate for DENV detection.

While the sensitive, rapid, and multiplexed detection method and platforms we have developed have demonstrated both quantitative and qualitative detection of viral RNAs, there are still opportunities for further optimization and refinement. The benefit of working with an aptamer-based detection system is that while there are established thermodynamic rules that guide the systems we work with, there is still a significant creative space to explore new nucleic-acid based designs and devices.

APPENDICES

APPENDIX A: NUPACK 4.0 Design and Analysis

NUPACK 4.0 example code of Broccoli aptamer based aptaswitch for the detection of a 27-nucleotide long DENV target sequence.

```
# Example NUPACK 4.0.0.0.28 Aptaswitch design to target DENV
from nupack import *

# Define physical model
    # Set design of an RNA sequence, simulated at 37 celsius
my_model = Model(material='rna', celsius=37)

# Define sequence domains of Aptaswitch
    # Ligand interacting domain for Broccoli aptamer, specified from literature
broccoli = Domain('GUCGAGUAGAGUGUGGCAAAGUUCGGAUGAACUUUGCGGUCGGGUCC', name='broccoli')

    # Toehold domain, specified based on target sequence
toehold = Domain('UGAGAAGCAUG', name='toehold')

    # Stabilizing stem domain, specified based on target sequence
stable_stem = Domain('GUCACGGAUC', name='stable_stem')

    # Clamp domain, specified based on target sequence
clamp = Domain('UUUUCC', name='clamp')

    # Loop domain, unspecified set to permutate through all nucleotide combinations
loop = Domain('N6', name='loop')


# Define strands containing domains from 5' to 3'
aptaswitch = TargetStrand([toehold, stable_stem, clamp, loop, ~clamp, ~stable_stem, broccoli, stable_stem], name='aptaswitch')
    # The toehold, stable_stem, and clamp domains have been defined based on the complementary sequence to the DENV target
```

```
39  DENV = TargetStrand([~clamp, ~stable_stem, ~toehold],
40        name='DENV')
41
42  # Define a target complex (DENV binds to aptaswitch)
43      # Define the secondary structure of the complex formed
44        by DENV activating the aptaswitch, using DU+ notation
45  aptaswitch_DENV = TargetComplex([aptaswitch, DENV], 'D27
46        (U6 U6 D10 (U47)+)', name='aptaswitch_DENV')
47
48  #Define a target test tube containing all off-target
49        complexes
50  t1 = TargetTube(on_targets={aptaswitch_DENV: 1e-06},
51        off_targets=SetSpec(max_size=2), name='t1')
52
53  # Set a stop condition of 1% and a seed for random number
54        generation to get a reproducible result for this demo
55  my_options = DesignOptions(f_stop=0.01, seed=93)
56
57  # Define and run the test tube design job
58  my_design = tube_design(tubes=[t1], model=my_model,
59        options=my_options)
60  my_results = my_design.run(trials=1)[0]
61
62  # Display the design results
63  my_results
```

Output:

Domain results:

Domain	Sequence
broccoli	GUCGAGUAGAGUGUGGCAAAGUUCGGAUGAACUUUGCGGUCGGGUCC
broccoli*	GGACCCGACCGCAAAGUUCAUCCGAACUUUGCCACACUCUACUCGAC
clamp	UUUUCC
clamp*	GGAAAA
loop	AGAAAA
loop*	UUUUCU
stable_stem	GUCACGGAUC
stable_stem*	GAUCCGUGAC
toehold	UGAGAAGCAUG
toehold*	CAUGCUUCUCA

Strand results:

Strand	Sequence
aptaswitch	UGAGAAGCAUGGUCACGGAUCUUUUCCAGAAAAGGAAAAGAUCCGUGACGUCGAGUAGAGUGUGGCAAAGUUCGGAUGAACUUUGCGGUCGGGUCCGUCACGGAUC
DENV	GGAAAAGAUCCGUGACCAUGCUUCUCA

Objective function:

Objective type	Value
Weighted ensemble defect	0.244

Ensemble defect: 0.244

On-target complex defects:

Complex	Complex defect (nt)	Normalized complex defect
aptaswitch_DENV	32.4	0.244

Tube defects:

Tube	Tube defect (M)	Normalized tube defect
t1	3.24e-05	0.244

Complex contributions to tube defects:

Tube	On-target complex	Structural defect (M)	Concentration defect (M)	Total defect (M)
t1	aptaswitch_DENV	3.24e-05	1.77e-13	3.24e-05

On-target complex concentrations:

Tube	Complex	Concentration (M)	Target concentration (M)
t1	aptaswitch_DENV	1.00e-06	1.00e-06

Significant off-target complex concentrations (≥ 1% max complex concentration in tube):

Tube	Complex	Concentration (M)
t1	—	

As produced in the output code, NUPACK designed the unspecified loop sequence of the aptaswitch to be AGAAAA and spliced all the domains together to generate the full aptaswitch and target sequences. This simulation produced a normalized complex defect of 0.244 in a range from [0,1]. While a lower normalized ensemble defect would be

preferable, we see in the NUPACK MFE base-pair probability diagrams (**Figure A.1**), that the source of the incorrect base pairs is that we did not properly portray the binding of the Broccoli aptamer essential sequence. For simplicity reasons on line 46 of the NUPACK code, to describe the secondary structure of the aptaswitch target complex in DU+ notation, we described the formation of the Broccoli aptamer "(U47)" as a 47 nucleotide signal stranded loop. However, the Broccoli domain sequence does have some degree of self-binding that was not specified in the code and therefore counted as an error in the ensemble defect. We should note when comparing **Figure A.1-C** with the secondary structure as designed in lines 45 and 46 in the code that, except for the Broccoli domain, there is perfect consensus.

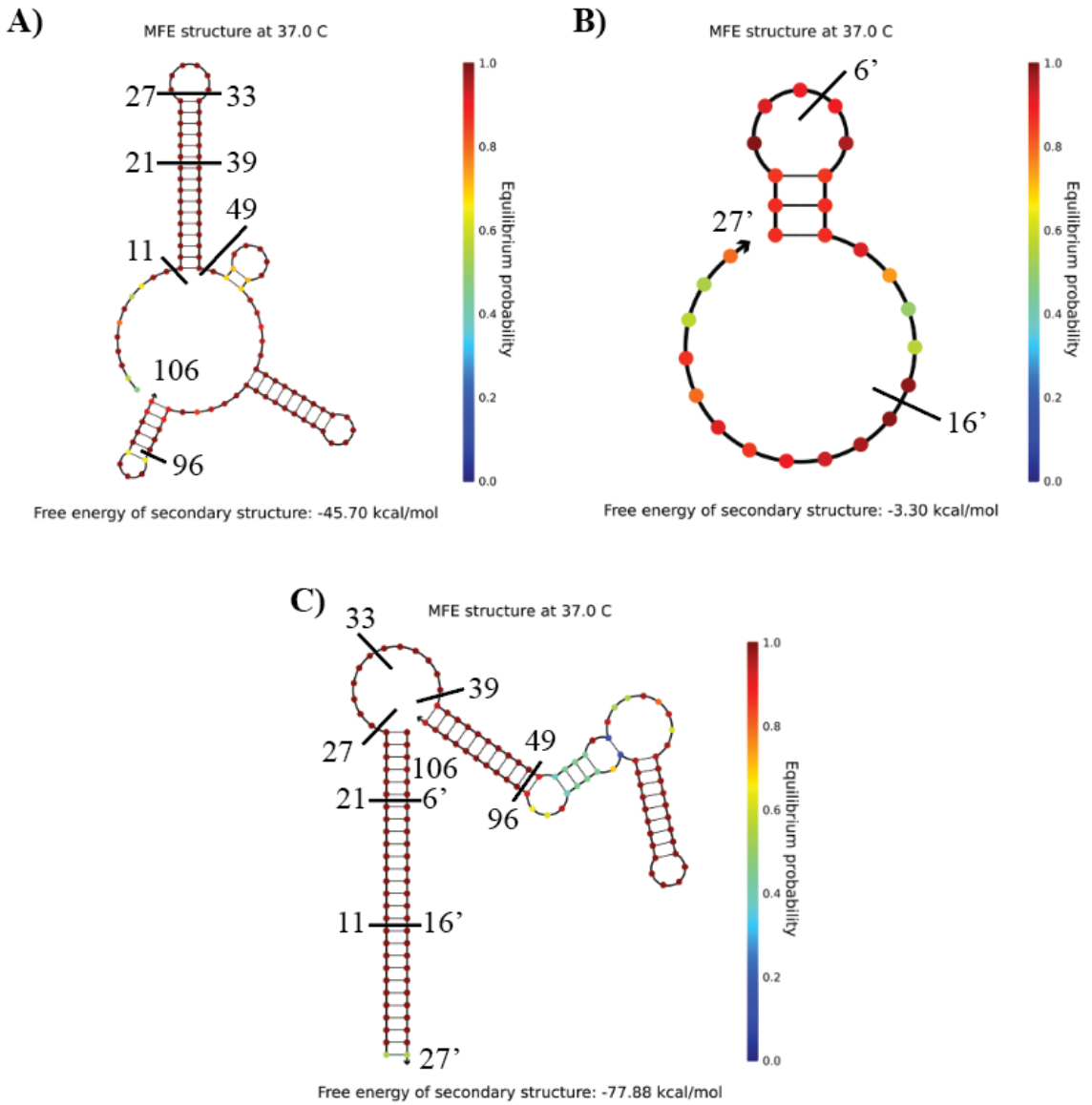

Figure A.1 | NUPACK 4.0 example minimum free energy and base-pair binding probability analysis A) NUPACK generated minimum free energy structure of aptaswitch at 37ºC. Nucleotides 0-11 correspond to the toehold, 12-21 stabilizing stem, 22-27 clamp, 28-33 loop, 34-39 clamp complement, 40-49 stabilizing stem complement, 50-96 Broccoli, and 97-106 stabilizing stem. **B)** NUPACK generated minimum free energy structure of DENV target at 37ºC. Nucleotides 0'-6' correspond to the clamp complement, 7'-16' stabilizing stem complement, and 17'-27' toehold complement. **C)** NUPACK generated minimum free energy structure of aptaswitch-DENV binding complex via toehold-mediated strand displacement at 37ºC.

The lower base pair binding probabilities seen in the Broccoli ligand interacting region in

Figure A.1-C are due in part to the fact that NUPACK simulations does not simulate all

the complex non-canonical interactions required by the aptamer to stably form, such as Hoogsteen pairing, internal ion stabilizations in G-quadraplexes or the stabilization that the ligand has on the aptamer. The MFE only shows a 2-dimensional secondary structure, while aptamers have a more complex 3-dimensional configuration. All being said, NUPACK simulations are simplified models of the experiments we perform, they are an excellent starting point, but in the end still require experimental validation.

APPENDIX B: Supplemental for Development of SARS-CoV-2 Platform

Table B.1 | RT-LAMP Protocol for Beta and Omicron Variants LOD

Materials	Concentration	Volume (uL)
WarmStart LAMP MM*	2x	10
RT-LAMP Primer Mix	10x	2
Target RNA	Copies/Rxn. [640,320, 160,80, 40,20, 10,5]	8

Run reaction at 67^{o}C for 30 minutes.
*WarmStart LAMP MM used from New England BioLabs WarmStart Multi-Purpose LAMP/RTLAMP 2x Master Mix

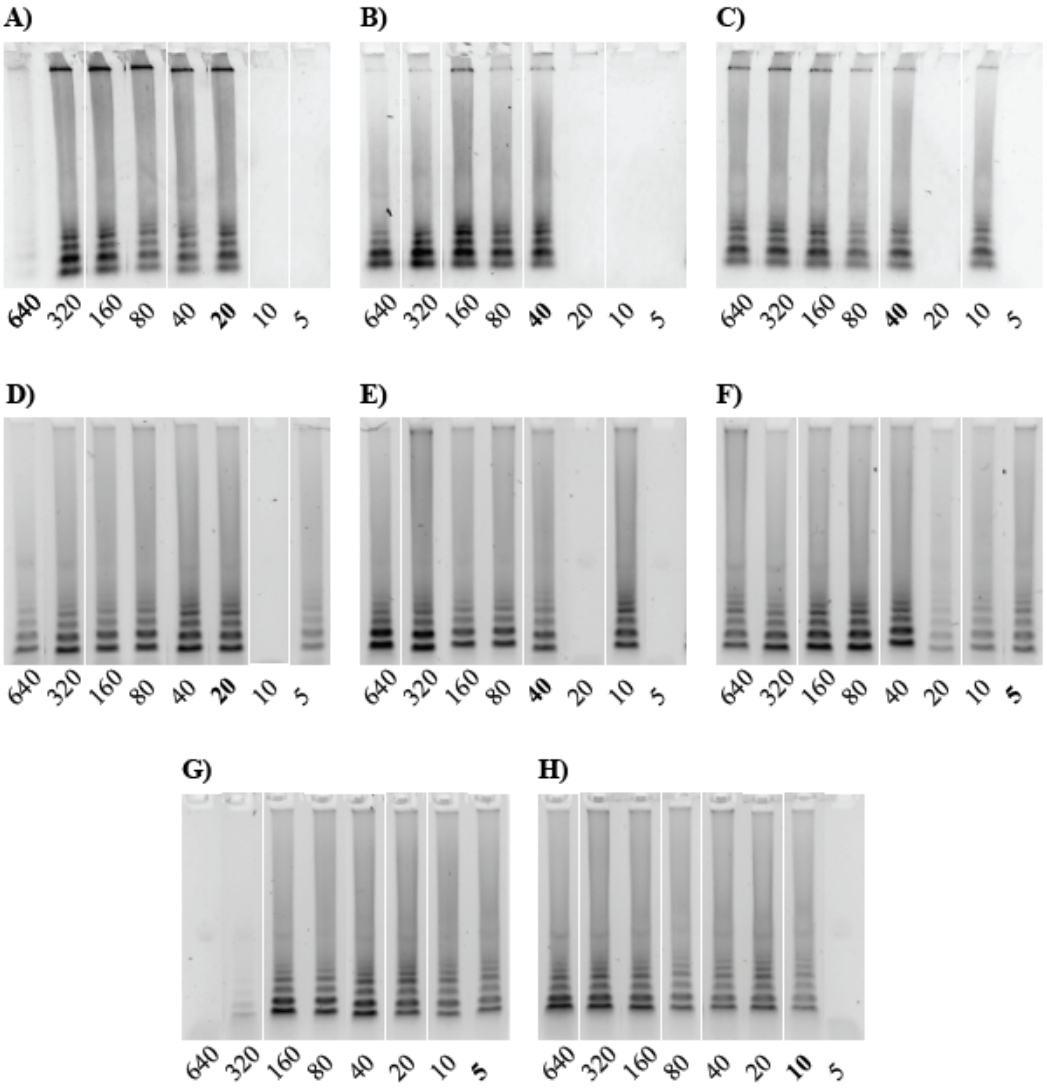

Figure B.1 | RT-LAMP LoD of SARS-CoV-2 Beta Variants. A-H) RT-LAMP primer mixes 1-8. **F)** Best performing RT-LAMP primer mix. Values are in viral RNA copies per reaction, bolded value indicates the LoD in a 20 µL reaction.

While **Fig B.1-F** and **Fig B.1-G**, have the same LoD, we identify **Fig B.1-F**, as the best performing, on account of **Fig B.1-G** does not amplify higher concentrations of viral RNA at 640 and minimally at 340 copies/reaction. Therefore, the dynamic range of amplification for **Fig B.1-F** primer mix is greater than **Fig B.1-G**.

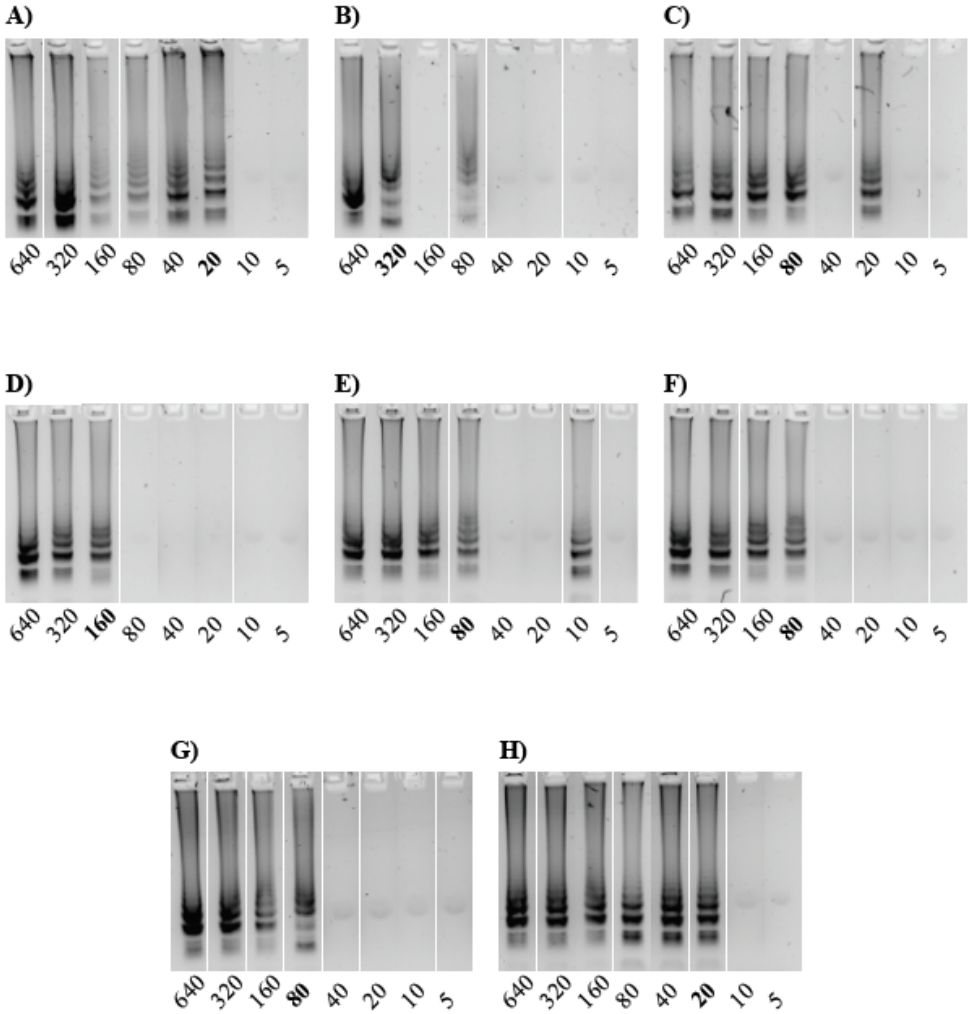

Figure B.2 | RT-LAMP LoD of SARS-CoV-2 Omicron Variants. A-H) RT-LAMP primer mixes 1-8. **H)** Best performing RT-LAMP primer mix. Values are in viral RNA copies per reaction, bolded value indicates the LOD in a 20 µL reaction.

While **Fig B.2-A** and **Fig B.2-H**, have the same LoD, we identify **Fig B.2-H**, as the best performing because greater amplicon synthesis, as indicated by the darker bands. As can be seen in both **Figure B.1** and **B.2**, there are some non-specific amplifications in cases where we see laddered RT-LAMP amplicon that is below the identified LoD. In **Figure B.2-E**, the amplicons at 10 copies/reaction are not likely to be Omicron since there is no amplicons produced at 40 and 20 copies/reaction.

APPENDIX C: Supplemental for Multiplexing Platform

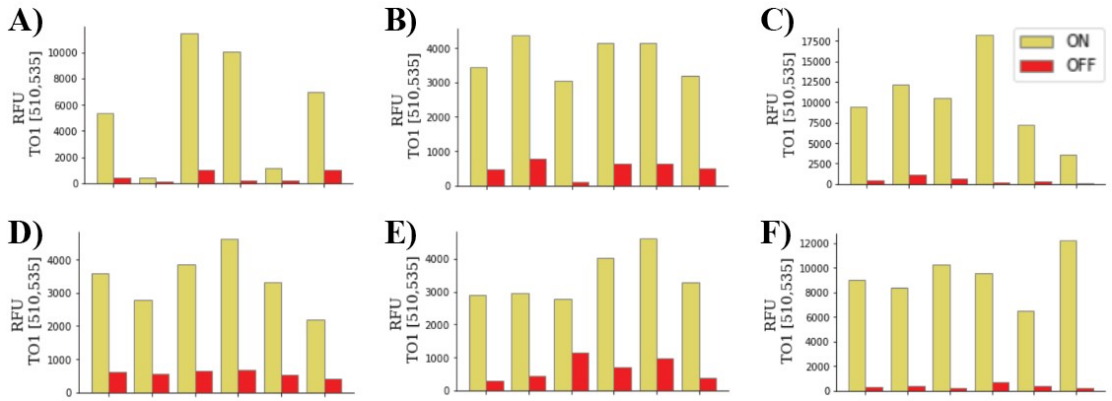

Figure C.1 | Viral screening against Mango-III aptaswitch library. A) Mango-III aptaswitches screened against CHIKV target. **B)** Mango-III aptaswitches screened against DENV target. **C)** Mango-III aptaswitches screened against PlsF target. **D)** Mango-III aptaswitches screened against WNV target. **E)** Mango-III aptaswitches screened against YFV target. **F)** Mango-III aptaswitches screened against ZIKV target.

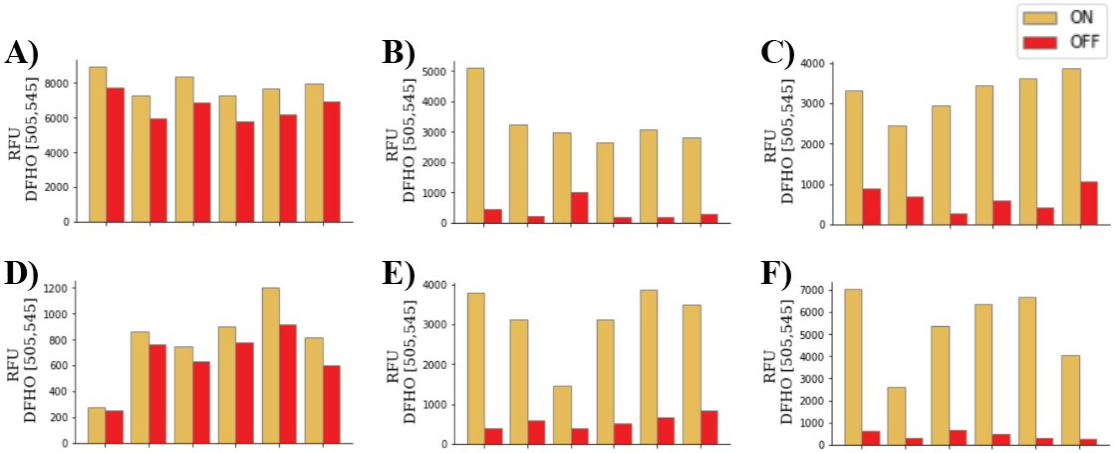

Figure C.2 | Viral screening against Corn aptaswitch library. A) Corn aptaswitches screened against CHIKV target. **B)** Corn aptaswitches screened against DENV target. **C)** Corn aptaswitches screened against PlsF target. **D)** Corn aptaswitches screened against WNV target. **E)** Corn aptaswitches screened against YFV target. **F)** Corn aptaswitches screened against ZIKV target.

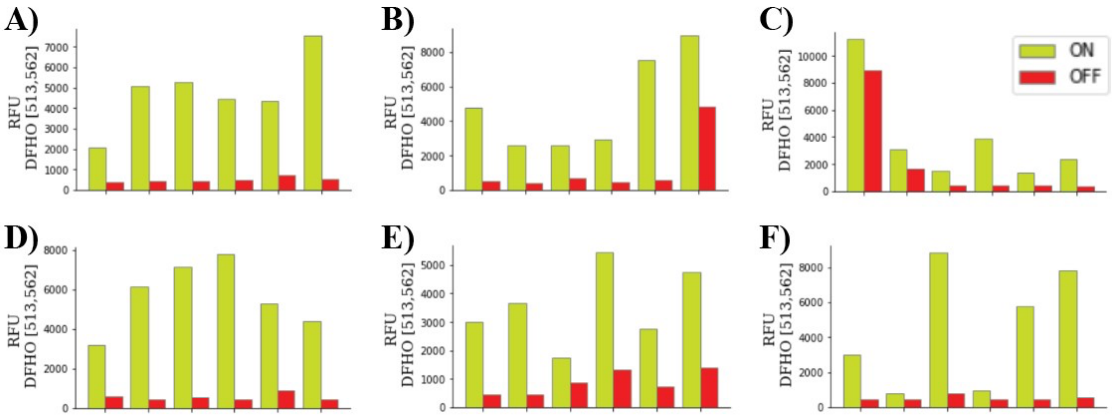

Figure C.3 | Viral screening against Orange Broccoli aptaswitch library. A) Orange Broccoli aptaswitches screened against CHIKV target. **B)** Orange Broccoli aptaswitches screened against DENV target. **C)** Orange Broccoli aptaswitches screened against PlsF target. **D)** Orange Broccoli aptaswitches screened against WNV target. **E)** Orange Broccoli aptaswitches screened against YFV target. **F)** Orange Broccoli aptaswitches screened against ZIKV target.

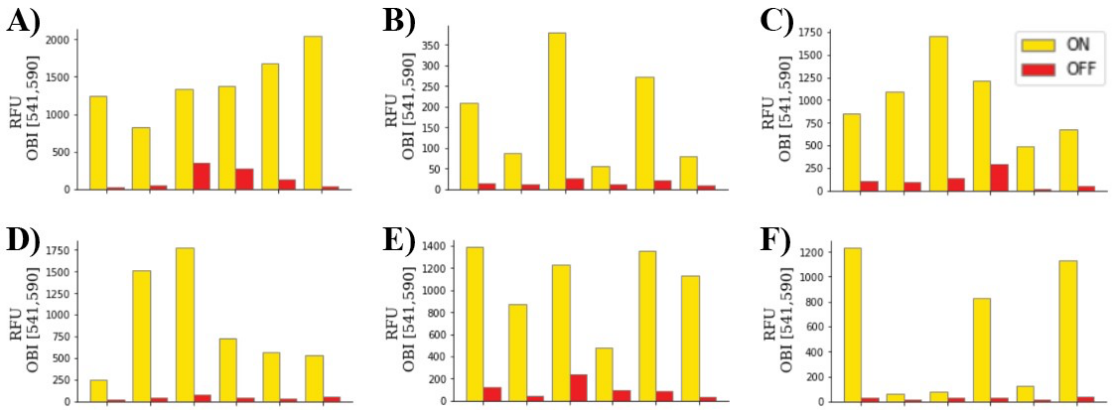

Figure C.4 | Viral screening against Red Broccoli aptaswitch library. A) Red Broccoli aptaswitches screened against CHIKV target. **B)** Red Broccoli aptaswitches screened against DENV target. **C)** Red Broccoli aptaswitches screened against PlsF target. **D)** Red Broccoli aptaswitches screened against WNV target. **E)** Red Broccoli aptaswitches screened against YFV target. **F)** Red Broccoli aptaswitches screened against ZIKV target.

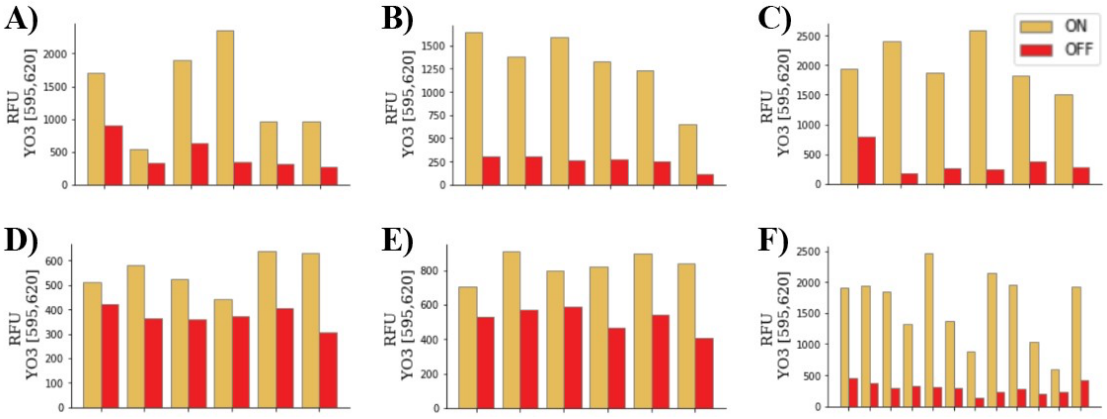

Figure C.5 | Viral screening against Mango-IV aptaswitch library. A) Mango-IV aptaswitches screened against CHIKV target. **B)** Mango-IV aptaswitches screened against DENV target. **C)** Mango-IV aptaswitches screened against PlsF target. **D)** Mango-IV aptaswitches screened against WNV target. **E)** Mango-IV aptaswitches screened against YFV target. **F)** Mango-IV aptaswitches screened against ZIKV target.

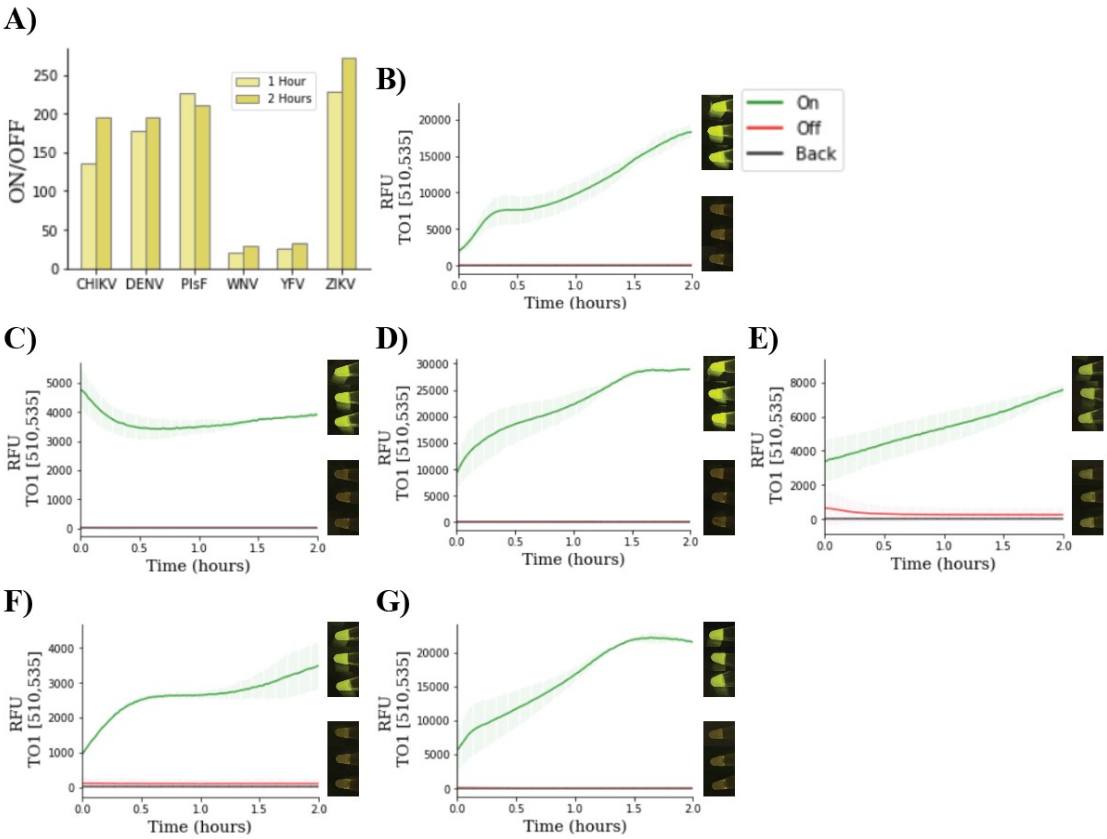

Figure C.6 | Top performing viral targeting Mango-III aptaswitches in triplicate. A) Mean fold change of top performing viral targeting Mango-III aptaswitches. **B)** Time course curve of top Mango-III aptaswitch against CHIKV. **C)** Time course curve of top Mango-III aptaswitch against DENV. **D)** Time course curve of top Mango-III aptaswitch against PlsF. **E)** Time course curve of top Mango-III aptaswitch against WNV. **F)** Time course curve of top Mango-III

aptaswitch against YFV. **G)** Time course curve of top Mango-III aptaswitch against ZIKV. Top fluorescent image for each group is ON triplicate, bottom image is OFF triplicate.

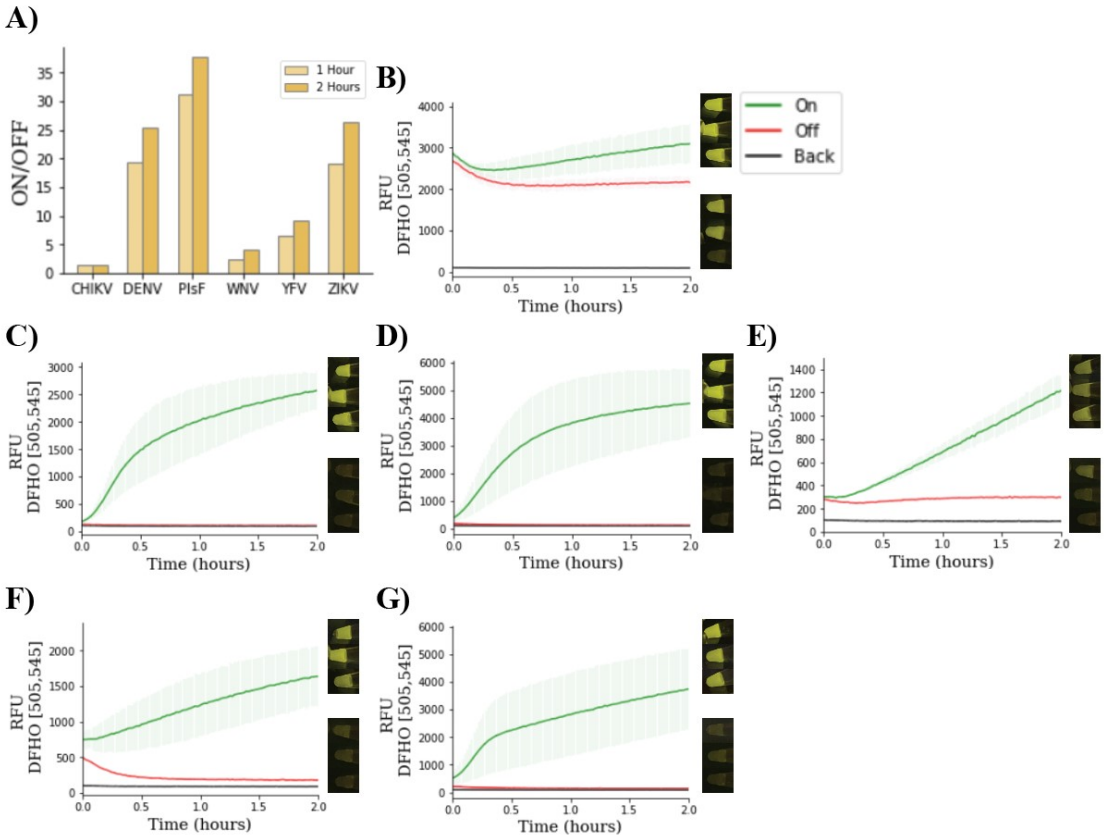

Figure C.7 | Top performing viral targeting Corn aptaswitches in triplicate. A) Mean fold change of top performing viral targeting Corn aptaswitches. **B)** Time course curve of top Corn aptaswitch against CHIKV. **C)** Time course curve of top Corn aptaswitch against DENV. **D)** Time course curve of top Corn aptaswitch against PlsF. **E)** Time course curve of top Corn aptaswitch against WNV. **F)** Time course curve of top Corn aptaswitch against YFV. **G)** Time course curve of top Corn aptaswitch against ZIKV. Top fluorescent image for each group is ON triplicate, bottom image is OFF triplicate.

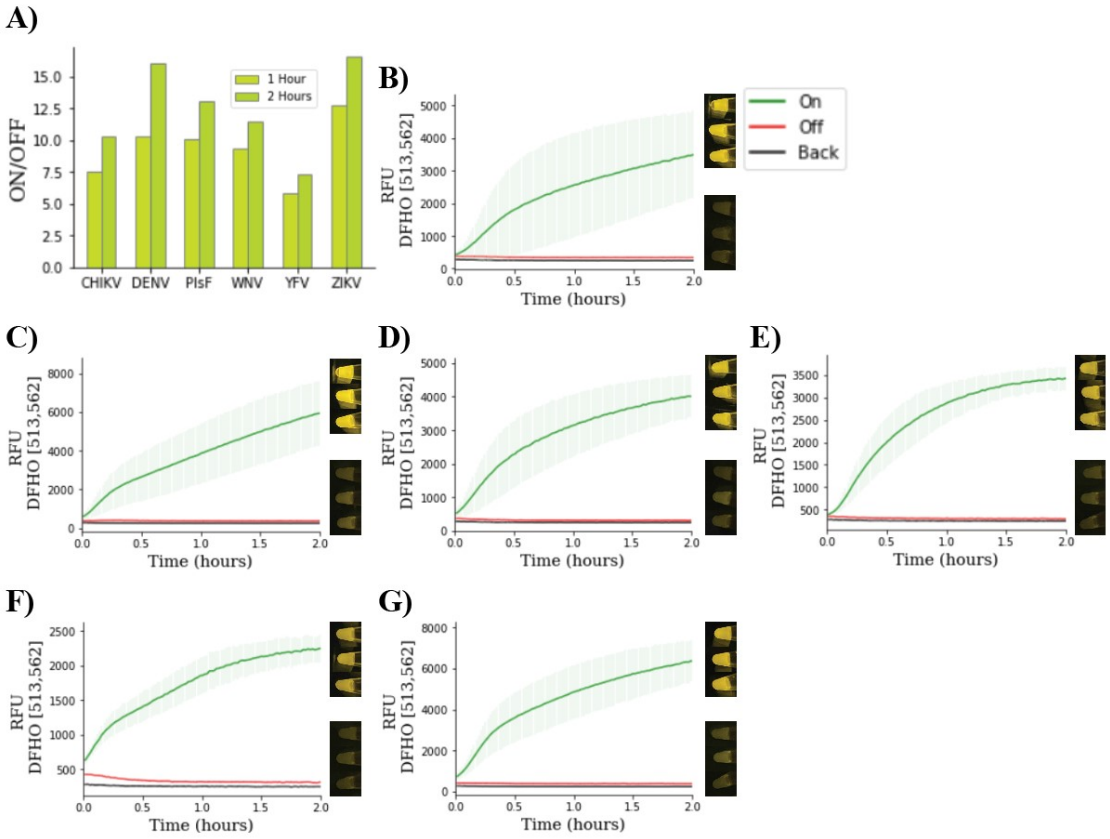

Figure C.8 | Top performing viral targeting Orange Broccoli aptaswitches in triplicate. A) Mean fold change of top performing viral targeting Orange Broccoli aptaswitches. **B)** Time course curve of top Orange Broccoli aptaswitch against CHIKV. **C)** Time course curve of top Orange Broccoli aptaswitch against DENV. **D)** Time course curve of top Orange Broccoli aptaswitch against PlsF. **E)** Time course curve of top Orange Broccoli aptaswitch against WNV. **F)** Time course curve of top Orange Broccoli aptaswitch against YFV. **G)** Time course curve of top Orange Broccoli aptaswitch against ZIKV. Top fluorescent image for each group is ON triplicate, bottom image is OFF triplicate.

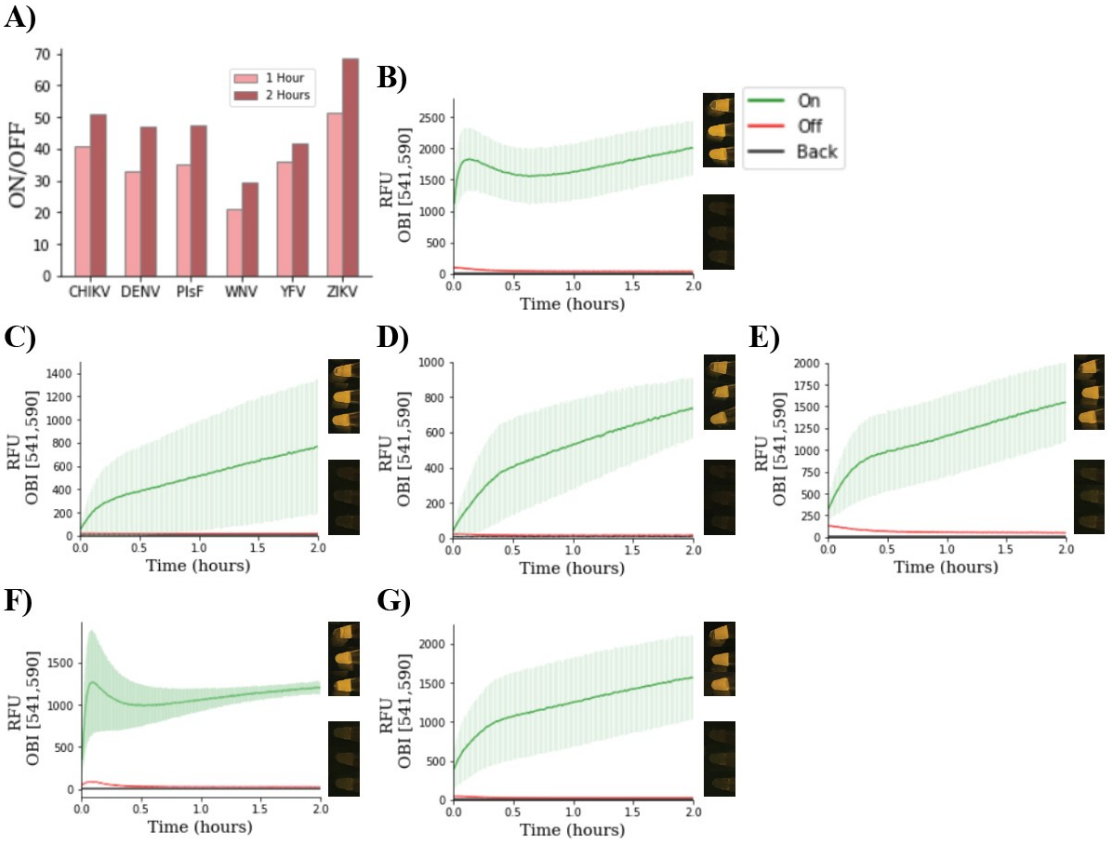

Figure C.9 | Top performing viral targeting Red Broccoli aptaswitches in triplicate. A) Mean fold change of top performing viral targeting Red Broccoli aptaswitches. **B)** Time course curve of top Red Broccoli aptaswitch against CHIKV. **C)** Time course curve of top Red Broccoli aptaswitch against DENV. **D)** Time course curve of top Red Broccoli aptaswitch against PlsF. **E)** Time course curve of top Red Broccoli aptaswitch against WNV. **F)** Time course curve of top Red Broccoli aptaswitch against YFV. **G)** Time course curve of top Red Broccoli aptaswitch against ZIKV. Top fluorescent image for each group is ON triplicate, bottom image is OFF triplicate.

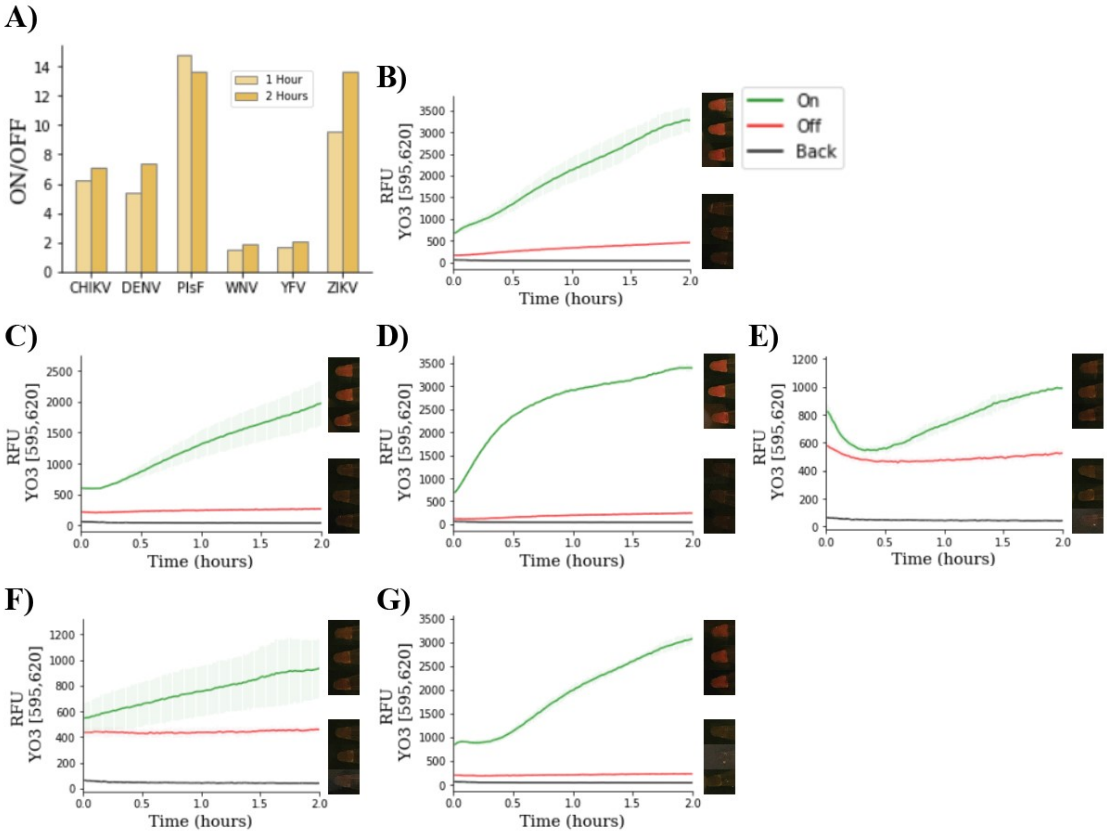

Figure C.10 | Top performing viral targeting Mango-IV aptaswitches in triplicate. A) Mean fold change of top performing viral targeting Mango-IV aptaswitches. **B)** Time course curve of top Mango-IV aptaswitch against CHIKV. **C)** Time course curve of top Mango-IV aptaswitch against DENV. **D)** Time course curve of top Mango-IV aptaswitch against PlsF. **E)** Time course curve of top Mango-IV aptaswitch against WNV. **F)** Time course curve of top Mango-IV aptaswitch against YFV. **G)** Time course curve of top Mango-IV aptaswitch against ZIKV. Top fluorescent image for each group is ON triplicate, bottom image is OFF triplicate.

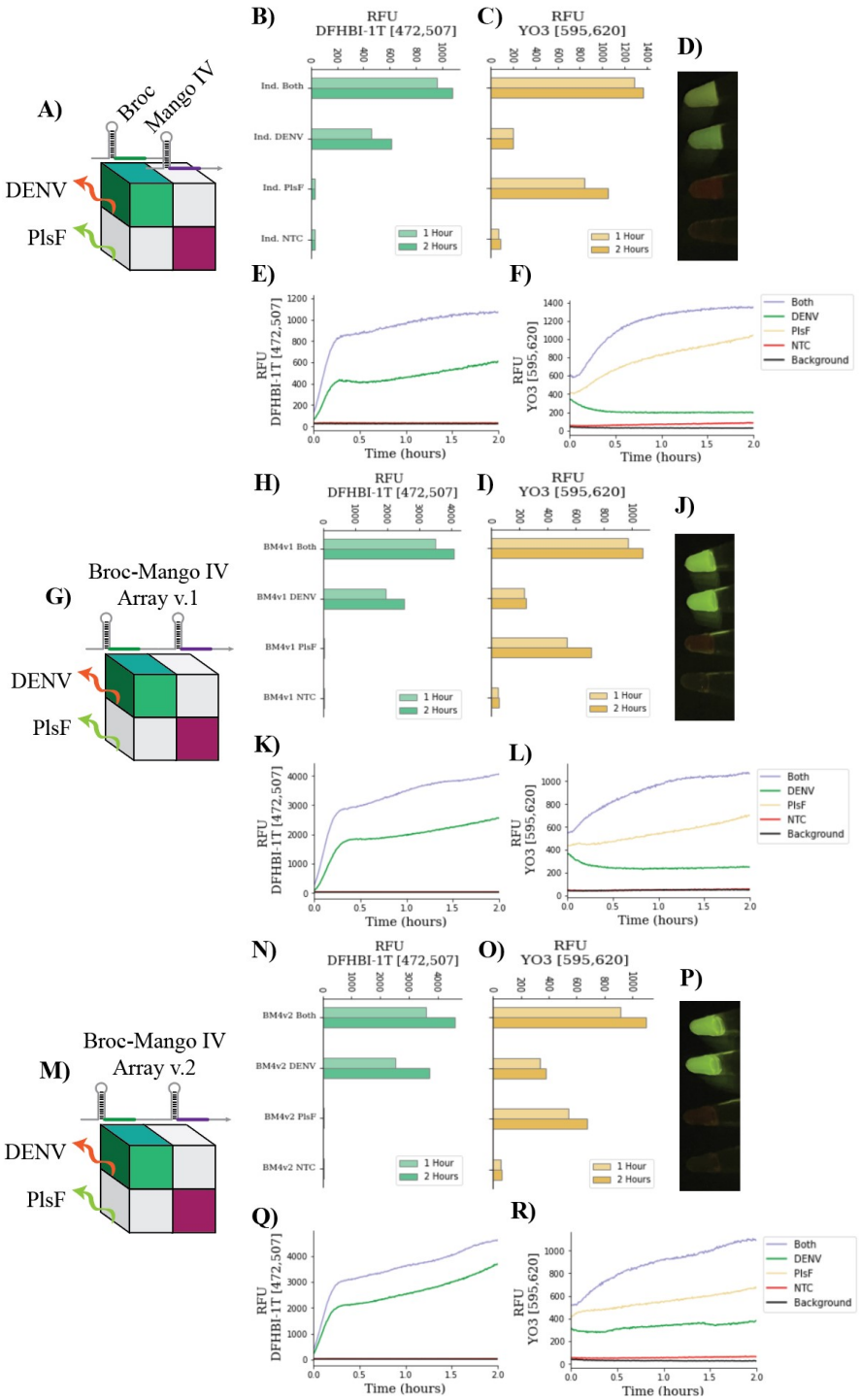

Figure C.11 | Broccoli–Mango-IV multiplexing arrays. A-F) Broccoli–Mango-IV individual aptaswitch control. **G-L)** Broccoli–Mango-IV multiplexing array design one. **M-R)** Broccoli–Mango-IV multiplexing array design two.

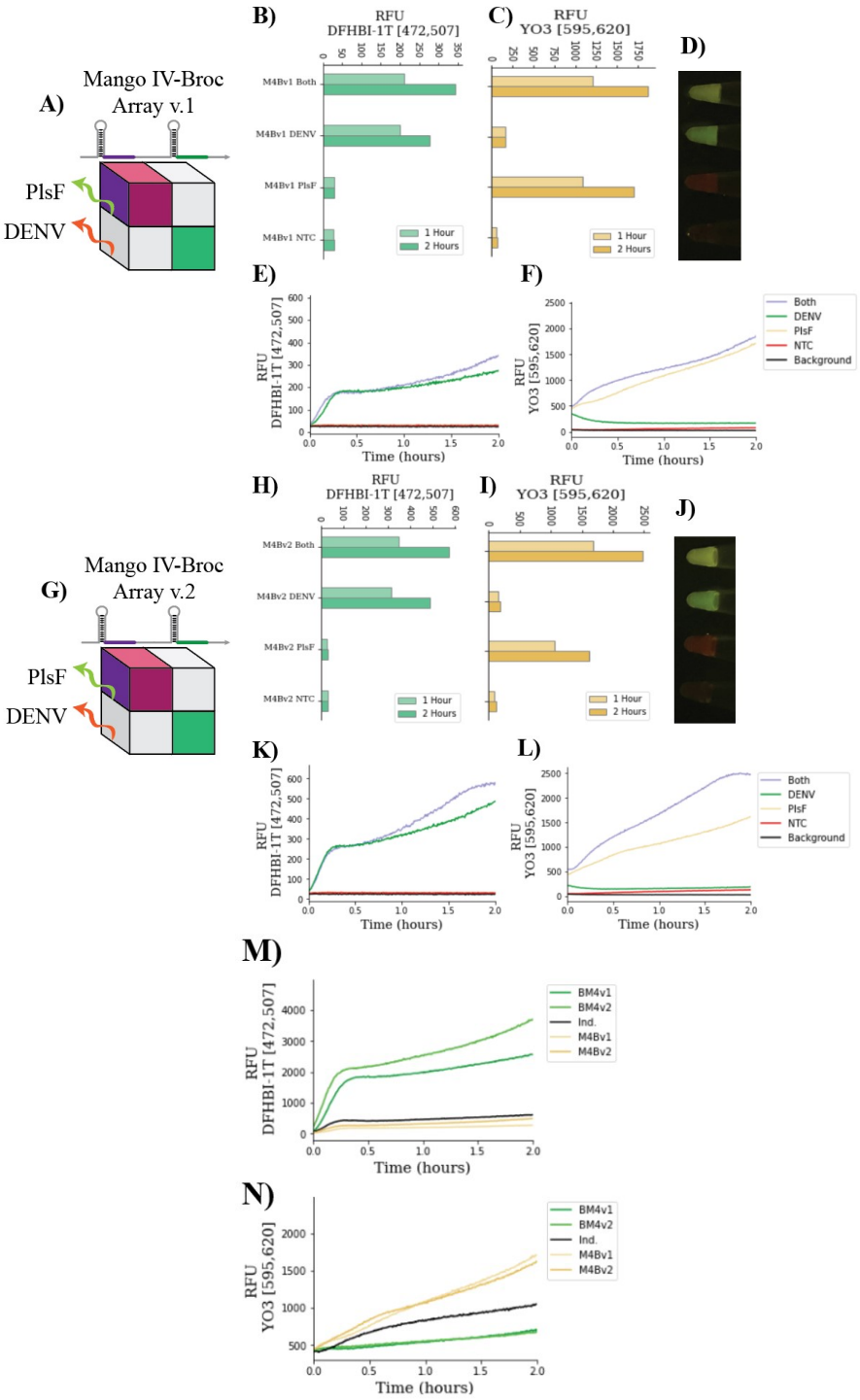

Figure C.12 | Broccoli–Mango-IV multiplexing arrays continued. A-F) Mango-IV–Broccoli multiplexing array design one. **G-L)** Mango-IV–Broccoli multiplexing array design two. **M)** DFHBI-1T channel time course curve of all Broccoli–Mango-IV arrays and individual aptaswitch platforms with DENV target only. **N)** YO3 channel time course curve of all Broccoli–Mango-IV arrays and individual aptaswitch platforms with PlsF target only.

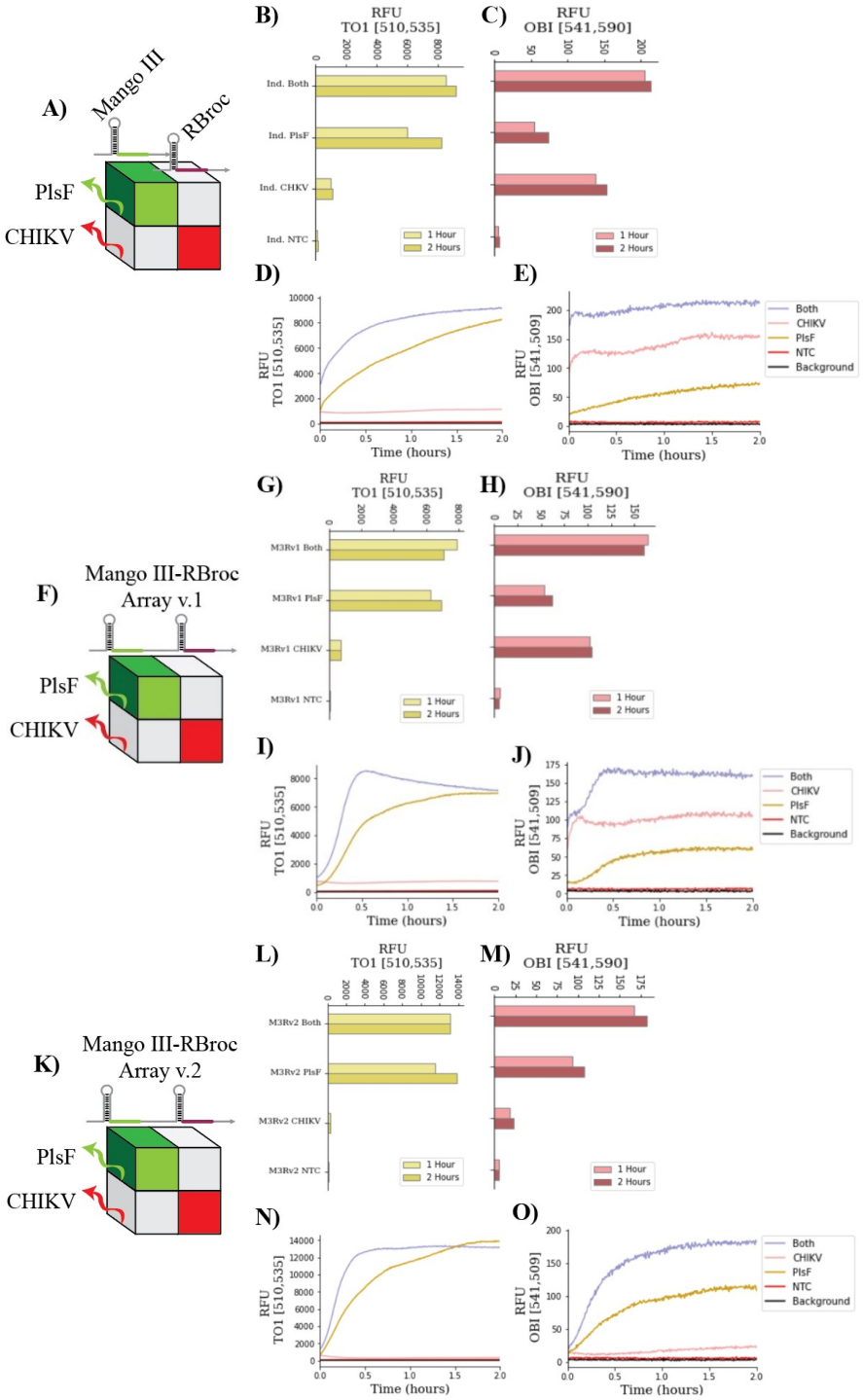

Figure C.13 | Mango-III–Red Broccoli multiplexing arrays. A-E) Mango-III–Red Broccoli individual aptaswitch control. **F-J)** Mango-III–Red Broccoli multiplexing array design one. **K-O)** Mango-III–Red Broccoli multiplexing array design two.

BIBLIOGRAPHY

[1] World Health Organization. WHO Coronavirus (COVID-19) Dashboard. (2023). URL: https://covid19.who.int/

[2] Thompson, D. & Lei, Y. Mini review: Recent progress in RT-LAMP enabled COVID-19 detection. *Sensors and Actuators Reports* **2**, 100017 (2020).

[3] Larremore, D. B. *et al.* Test sensitivity is secondary to frequency and turnaround time for COVID-19 screening. *Science Advances* **7**, eabd5393 (2021).

[4] Schuffenecker, I. *et al.* Genome Microevolution of Chikungunya Viruses Causing the Indian Ocean Outbreak. *PLoS Medicine* **3**, e263 (2006).

[5] Mavalankar, D., Shastri, P. & Raman, P. Chikungunya epidemic in India: a major public-health disaster. *The Lancet. Infectious Diseases* **7**, 306–307 (2007).

[6] Lanciotti, R. S. *et al.* Genetic and Serologic Properties of Zika Virus Associated with an Epidemic, Yap State, Micronesia, 2007. *Emerging Infectious Diseases* **14**, 1232–1239 (2008).

[7] Silva, M. M. O. *et al.* Concomitant Transmission of Dengue, Chikungunya, and Zika Viruses in Brazil: Clinical and Epidemiological Findings from Surveillance for Acute Febrile Illness. *Clinical Infectious Diseases* **69**, 1353–1359 (2019).

[8] Sukla, S., Mondal, P., Biswas, S. & Ghosh, S. A Rapid and Easy-to-Perform Method of Nucleic-Acid Based Dengue Virus Diagnosis Using Fluorescence-Based Molecular Beacons. *Biosensors* **11**, 479 (2021). https://doi.org/10.3390/bios11120479

[9] Hunsperger, E. A. *et al.* Evaluation of Commercially Available Diagnostic Tests for the Detection of Dengue Virus NS1 Antigen and Anti-Dengue Virus IgM Antibody. *PLoS Neglected Tropical Diseases* **8**, e3171 (2014).

[10] World Health Organization. Dengue guidelines for diagnosis, treatment, prevention and control: new edition. (2009). https://apps.who.int/iris/rest/bitstreams/52567/retrieve

[11] Moloney, R. M., Kmush, B., Rudolph, K. E., Cummings, D. A. T. & Lessler, J. Incubation Periods of Mosquito-Borne Viral Infections: A Systematic Review. *The American Journal of Tropical Medicine and Hygiene* **90**, 882–891 (2014).

[12] Sea, V. R. F. *et al.* Underreporting of Dengue-4 in Brazil Due to Low Sensitivity of the NS1 Ag Test in Routine Control Programs. *PLoS One* **8**, e64056 (2013).

[13] Siqueira, J. B., Martelli, C. M. T., Coelho, G. E., Simplício, A. C. da R. & Hatch, D. L. Dengue and Dengue Hemorrhagic Fever, Brazil, 1981–2002. *Emerging Infectious Diseases* **11**, 48–53 (2005).

[14] Saswat, T. *et al.* High rates of co-infection of Dengue and Chikungunya virus in Odisha and Maharashtra, India during 2013. *Infection, Genetics and Evolution* **35**, 134–141 (2015).

[15] Bhatt, S. *et al.* The global distribution and burden of dengue. *Nature* **496**, 504–507 (2013).

[16] Muller, D. A., Depelsenaire, A. C. I. & Young, P. R. Clinical and Laboratory Diagnosis of Dengue Virus Infection. *The Journal of Infectious Diseases* **215**, S89–S95 (2017).

[17] Lima, E. C. B. de, Montarroyos, U. R., Magalhães, J. J. F. de, Dimech, G. S. & Lacerda, H. R. Survival analysis in non-congenital neurological disorders related to dengue, chikungunya and Zika virus infections in Northeast Brazil. *Revista do Instituto de Medicina Tropical de São Paulo* **62**, e69 (2020).

[18] Karlikow, M. *et al.* Field validation of the performance of paper-based tests for the detection of the Zika and chikungunya viruses in serum samples. *Nature Biomedical Engineering* **6**, 246–256 (2022).

[19] Hall, R. A. & Macdonald, J. Synthetic Biology Provides a Toehold in the Fight against Zika. *Cell Host & Microbe* **19**, 752–754 (2016).

[20] World malaria report 2021. Geneva: World Health Organization. (2021). License: CC BY-NC-SA 3.0 IGO. https://apps.who.int/iris/rest/bitstreams/1398397/retrieve

[21] Schulte, S. J., Huang, J. & Pierce, N. A. Hybridization Chain Reaction Lateral Flow Assays for Amplified Instrument-Free At-Home SARS-CoV-2 Testing. *ACS Infectious Diseases* acsinfecdis.2c00472 (2023) doi:10.1021/acsinfecdis.2c00472.

[22] Gubala, V., Harris, L. F., Ricco, A. J., Tan, M. X. & Williams, D. E. Point of Care Diagnostics: Status and Future. *Analytical Chemistry* **84**, 487–515 (2012).

[23] Khormi, H. M. & Kumar, L. Climate change and the potential global distribution of Aedes aegypti: spatial modelling using geographical information system and CLIMEX. *Geospatial Health* **8**, 405 (2014).

[24] Lin, K. *et al.* Fast and visual detection of nucleic acids using a one-step RPA-CRISPR detection (ORCD) system unrestricted by the PAM. *Analytica*

Chimica Acta **1248**, 340938 (2023).

[25] Ma, D. *et al.* Multi-arm RNA junctions encoding molecular logic unconstrained by input sequence for versatile cell-free diagnostics. *Nature Biomedical Engineering* **6**, 298–309 (2022).

[26] Wu, K. & Green, A. A. Sensitive detection of SARS-CoV-2 on paper. *Nature Biomedical Engineering* **6**, 928–929 (2022).

[27] Pardee, K. *et al.* Rapid, Low-Cost Detection of Zika Virus Using Programmable Biomolecular Components. *Cell* **165**, 1255–1266 (2016).

[28] Stojanovic, M. N., de Prada, P. & Landry, D. W. Aptamer-Based Folding Fluorescent Sensor for Cocaine. *Journal of the American Chemical Society* **123**, 4928–4931 (2001).

[29] Pfeiffer, F. & Mayer, G. Selection and Biosensor Application of Aptamers for Small Molecules. *Frontiers in Chemistry* **4**, (2016).

[30] Nutiu, R. & Li, Y. Structure-Switching Signaling Aptamers. *Journal of the American Chemical Society* **125**, 4771–4778 (2003).

[31] Mairal, T. *et al.* Aptamers: molecular tools for analytical applications. *Analytical and Bioanalytical Chemistry* **390**, 989–1007 (2008).

[32] Lee, I., Kwon, S.-J., Sorci, M., Heeger, P. S. & Dordick, J. S. Highly Sensitive Immuno-CRISPR Assay for CXCL9 Detection. *Analytical Chemistry* **93**, 16528–16534 (2021).

[33] Rusk, N. De novo–designed riboregulators. *Nature Methods* **11**, 1192–1192 (2014).

[34] Durand, G. *et al.* A combinatorial approach to the repertoire of RNA kissing motifs; towards multiplex detection by switching hairpin aptamers. *Nucleic Acids Research* **44**, 4450–4459 (2016).

[35] Nutiu, R. & Li, Y. Aptamers with fluorescence-signaling properties. *Methods* **37**, 16–25 (2005).

[36] Pardee, K. *et al.* Paper-Based Synthetic Gene Networks. *Cell* **159**, 940–954 (2014).

[37] Green, A. A., Silver, P. A., Collins, J. J. & Yin, P. Toehold Switches: De-Novo-Designed Regulators of Gene Expression. *Cell* **159**, 925–939 (2014).

[38] Bushhouse, D. Z., Choi, E. K., Hertz, L. M. & Lucks, J. B. How does RNA fold dynamically? *Journal of Molecular Biology* **434**, 167665 (2022).

[39] Sukla, S., Ghosh, A., Saha, R., De, A., Adhya, S., Biswas, S. In-depth molecular analysis of a small cohort of human and Aedes mosquito (adults and larvae) samples from Kolkata revealed absence of Zika but high prevalence of dengue virus. *Journal of Medical Microbiology* **67**, 1109–1119 (2018).

[40] Daher, R. K., Stewart, G., Boissinot, M. & Bergeron, M. G. Recombinase Polymerase Amplification for Diagnostic Applications. *Clinical Chemistry* **62**, 947–958 (2016).

[41] Guatelli, J. C. *et al.* Isothermal, in vitro amplification of nucleic acids by a multienzyme reaction modeled after retroviral replication. *Proceedings of the National Academy of Science of the United States of America* **85**(5), 1874–1878 (1990). https://doi.org/10.1073/pnas.87.5.1874

[42] Mascini, M., Palchetti, I. & Tombelli, S. Nucleic Acid and Peptide Aptamers: Fundamentals and Bioanalytical Aspects. *Angewandte Chemie International Edition* **51**, 1316–1332 (2012).

[43] Mandal, M. & Breaker, R. R. Gene regulation by riboswitches. *Nature Reviews. Molecular Cell Biology* **5**, 451–463 (2004).

[44] Azéma, L. *et al.* Triggering nucleic acid nanostructure assembly by conditional kissing interactions. *Nucleic Acids Research* **46**, 1052–1058 (2018).

[45] Jeng, S. C. Y., Chan, H. H. Y., Booy, E. P., McKenna, S. A. & Unrau, P. J. Fluorophore ligand binding and complex stabilization of the RNA Mango and RNA Spinach aptamers. *RNA* **22**, 1884–1892 (2016).

[46] Serganov, A. & Nudler, E. A Decade of Riboswitches. *Cell* **152**, 17–24 (2013).

[47] Harish, B. *et al.* Hidden intermediates in Mango III RNA aptamer folding revealed by pressure perturbation. *Biophysical Journal* **121**, 421–429 (2022).

[48] Sett, A., Zara, L., Dausse, E. & Toulmé, J.-J. A malachite green light-up aptasensor for the detection of theophylline. *Talanta* **232**, 122417 (2021).

[49] Nazarenko, I. Effect of primary and secondary structure of oligodeoxyribonucleotides on the fluorescent properties of conjugated dyes. *Nucleic Acids Research* **30**, 2089–2195 (2002).

[50] Sett, A., Zara, L., Dausse, E. & Toulmé, J.-J. Engineering Light-Up Aptamers for the Detection of RNA Hairpins through Kissing Interaction. *Analytical Chemistry* **92**, 9113–9117 (2020).

[51] Paige, J. S., Nguyen-Duc, T., Song, W. & Jaffrey, S. R. Fluorescence Imaging of Cellular Metabolites with RNA. *Science* **335**, 1194–1194 (2012).

[52] Jenison, R. D., Gill, S. C., Pardi, A. & Polisky, B. High-Resolution Molecular Discrimination by RNA. *Science* **263**, 1425–1429 (1994).

[53] Filonov, G. S., Moon, J. D., Svensen, N. & Jaffrey, S. R. Broccoli: Rapid Selection of an RNA Mimic of Green Fluorescent Protein by Fluorescence-Based Selection and Directed Evolution. *Journal of the American Chemical Society* **136**, 16299–16308 (2014).

[54] Tuerk, C. & Gold, L. Systematic Evolution of Ligands by Exponential Enrichment: RNA Ligands to Bacteriophage T4 DNA Polymerase. *Science* **249**, 505–510 (1990).

[55] Ma, H. *et al.* Nucleic acid aptamers in cancer research, diagnosis and therapy. *Chemical Society Reviews* **44**, 1240–1256 (2015).

[56] Paige, J. S., Wu, K. Y. & Jaffrey, S. R. RNA Mimics of Green Fluorescent Protein. *Science* **333**, (2011).

[57] Ouellet, J. RNA Fluorescence with Light-Up Aptamers. *Frontiers in Chemistry* **4**, (2016).

[58] Jung, J. K., Archuleta, C. M., Alam, K. K. & Lucks, J. B. Programming cell-free biosensors with DNA strand displacement circuits. *Nature Chemical Biology* **18**, 385–393 (2022).

[59] Dolgosheina, E. V. *et al.* RNA Mango Aptamer-Fluorophore: A Bright, High-Affinity Complex for RNA Labeling and Tracking. *ACS Chemical Biology* **9**, 2412–2420 (2014).

[60] Umar, M. I., Ji, D., Chan, C.-Y. & Kwok, C. K. G-Quadruplex-Based Fluorescent Turn-On Ligands and Aptamers: From Development to Applications. *Molecules* **24**, 2416 (2019).

[61] Scalise, D. & Schulman, R. Controlling Matter at the Molecular Scale with DNA Circuits. *Annual Review of Biomedical Engineering* **21**, 469–493 (2019).

[62] Kim, J. *et al.* De novo-designed translation-repressing riboregulators for multi-input cellular logic. *Nature Chemical Biology* **15**, 1173–1182 (2019).

[63] Zhang, Q. *et al.* Predictable control of RNA lifetime using engineered degradation-tuning RNAs. *Nature Chemical Biology* **17**, 828–836 (2021).

[64] Varani, G. Exceptionally Stable Nucleic Acid Hairpins. *Annual Review of Biophysics and Biomolecular Structure* **24**, 379–404 (1995).

[65] Fornace, M. E. *et al. NUPACK: Analysis and Design of Nucleic Acid Structures, Devices, and Systems*. https://chemrxiv.org/engage/chemrxiv/article-details/636c7089b588507d0045f283 (2022) doi:10.26434/chemrxiv-2022-xv98l.

[66] Chang, S.-F. *et al.* Concurrent Isolation of Chikungunya Virus and Dengue Virus from a Patient with Coinfection Resulting from a Trip to Singapore. *Journal of Clinical Microbiology* **48**, 4586–4589 (2010).

[67] Sourisseau, M. *et al.* Characterization of Reemerging Chikungunya Virus. *PLoS Pathogens* **3**, e89 (2007).

[68] Bookstaver, P. B. *et al.* Management of Viral Central Nervous System Infections: A Primer for Clinicians. *Journal of Central Nervous System Disease* **9**, 117957351770334 (2017).

[69] Mallewa, M. *et al.* Viral CNS infections in children from a malaria-endemic area of Malawi: a prospective cohort study. *The Lancet. Global Health* **1**, e153–e160 (2013).

[70] World Health Organization. West Nile virus fact sheet. (2017). URL: https://www.who.int/news-room/fact-sheets/detail/west-nile-virus

[71] World Health Organization. Yellow fever fact sheet. (2019). URL: https://www.who.int/news-room/fact-sheets/detail/yellow-fever

[72] World Health Organization. Zika virus fact sheet. (2022). URL: https://www.who.int/news-room/fact-sheets/detail/zika-virus

[73] Dey, S. K. *et al.* Repurposing an adenine riboswitch into a fluorogenic imaging and sensing tag. *Nature Chemical Biology* **18**, 180–190 (2022).

[74] Bouhedda, F. *et al.* A dimerization-based fluorogenic dye-aptamer module for RNA imaging in live cells. *Nature Chemical Biology* **16**, 69–76 (2020).

CURRICULUM VITAE